UNIVERSITY OF CALIFORNIA
RIVERSIDE

Engineering Metal-Oxide Photoelectrode: Synthesis and Application for Renewable Energy Devices

A Dissertation submitted in partial satisfaction
of the requirements for the degree of

Doctor of Philosophy

in

Chemical and Environmental Engineering

by

Kichang Jung

September 2019

Dissertation Committee:
Dr. Alfredo A. Martinez-Morales, Chairperson
Dr. Ruoxue Yan
Dr. Boniface P. T. Fokwa

The Dissertation of Kichang Jung is approved:

_____

_____

_____

Committee Chairperson

University of California, Riverside

Acknowledgement

I would like to express my most sincere gratitude towards my advisor Dr. Alfredo A. Martinez-Morales for his continuous support and help towards my Ph.D study and research; especially for his patience, guidance, and motivation. With his support I was able to complete this dissertation.

In addition to my advisor, I would like to show my gratitude towards my dissertation committee members: Dr. Ruoxue Yan and Dr. Boniface P. T. Fokwa. Their well thought out comments and guided questions were immensely appreciated.

I would like to show my gratitude for Dr. Ashok Mulchandani for allowing me the use of their lab equipment and Dr. Ha of Chonnam National University who introduced me to optoelectronics. Without access to these instruments, conducting research would be near impossible. I want to thank my lab mates Dr. Lim, Fei Gu, Seungjin Lee, Jiyong Kim, Minerva Uribe-Robles, Yaqiong Li, Shiva Sharma, and Megan Woods for their support and providing me with memories that I can cherish forever.

The SEM and TEM characterization were conducted at the Central Facility for Advanced Microscopy and Microanalysis (CFAMM). This research was funded by the University of California Advanced Solar Technologies Institute (UC Solar).

To my parents,

This dissertation is wholeheartedly dedicated to my beloved parents for inspiration who have been our source and gave me courage when I thought of giving up.

To my wife,

I would like to dedicate my work to loving wife Hyunji Kim.

ABSTRACT OF THE DISSERTATION

Engineering Metal-Oxide Photoelectrode: Synthesis and Application for Renewable Energy Devices

by

Kichang Jung

Doctor of Philosophy, Graduate Program in Chemical and Environmental Engineering
University of California, Riverside, September 2019
Dr. Alfredo A. Martinez-Morales, Chairperson

The synthesis and characterization of metal-oxide photoelectrodes used for various devices that produce a renewable energy source is studied and discussed in this dissertation. Due to the various applications of nanoscale metal-oxide materials there is a variety of characterization and synthesis methods. This work controls the morphology, layer stack, and composition of metal-oxide by adjusting synthesis parameters and methods. Chapter 2 discusses the synthesis of a ZnO-CuO structure which incorporates a ZnO nanorod core within a CuO thin film shell to use as a photocathode. A desirable diameter and length of the ZnO core is achieved by adjusting the synthesis parameters such as the ratio of oxygen to nitrogen gas, temperature, and the flow rate of gas. Continuing onto Chapter 3, the fabrication process of dye-sensitized solar cells which utilize the synthesized ZnO-CuO core-shell as a photoelectrode is discussed. The effects on the stability and performance of the CuO shell on the ZnO core implemented in the dye-sensitized solar cells is then investigated. The CuO shell on the ZnO core

successfully prevents the dissolution of Zn atoms during the dye absorption reaction on the surface of the photoelectrode. In Chapter 4, the effects of a Cu interlayer between Cu_2O photocathode and a transparent conductive film is studied for the use in the photoelectrochemical water splitting reaction. The physical deposition process and chemical reaction are used to study the formation of a desirable structure within the thin film stack. This method successfully fabricates a Cu_2O layer that intentionally removes the Cu interlayer or prevents the formation of a Cu interlayer with varying thickness. The intercalated Cu layer between Cu_2O and transparent conductive film prevents charge separation and accelerates its recombination during the photoelectrochemical reaction. Chapter 5 discusses the introduction of a doping method into the CuO crystal lattice structure. CuO is synthesized onto a transparent conductive film through electrodeposition. Zn doped-CuO is synthesized by adding a Zn dopant precursor into the electrodeposition solution. The electrodeposition process is optimized by controlling the applied potential, dopant concentration, temperature, and reaction time.

Table of Contents

List of Figures

Chapter 1

Chapter 2

List of Tables

Chapter 1

Introduction

1.1 Renewable Energy

Total energy consumption in the world is continuously increasing due to the growth in global population and the development and utilization of electronic devices. Figure 1.1 shows an expectation of higher energy production in the future due to a significant increase in electricity usage.[1] The typical sources of energy production are oil, gas, coal, nuclear, biomass, geothermal, solar, wind, and hydropower.[2] The automotive industry consumes a significant amount of energy, 96% of new registered vehicle in the world use gasoline as their energy source. Over time the electricity consumption has increased while the utilization of gasoline has decreased. This is due to an increase in use of renewable energy source powered vehicles.[3] A government policy has been implemented to reduce the use of gasoline gradually and eventually stop selling gasoline vehicles.[4] Due to the anticipated increase in energy consumption, it is important to develop efficient and sustainable renewable energy technologies.

Renewable energy has advantages such as the increase of the energy production , reduction of the environmental destruction and cost effectiveness for operating and maintenance.[5] Figure 1.1 shows usage for energy production from coal has decreased abruptly since the mid 2000's. Energy production from nuclear and gasoline have also

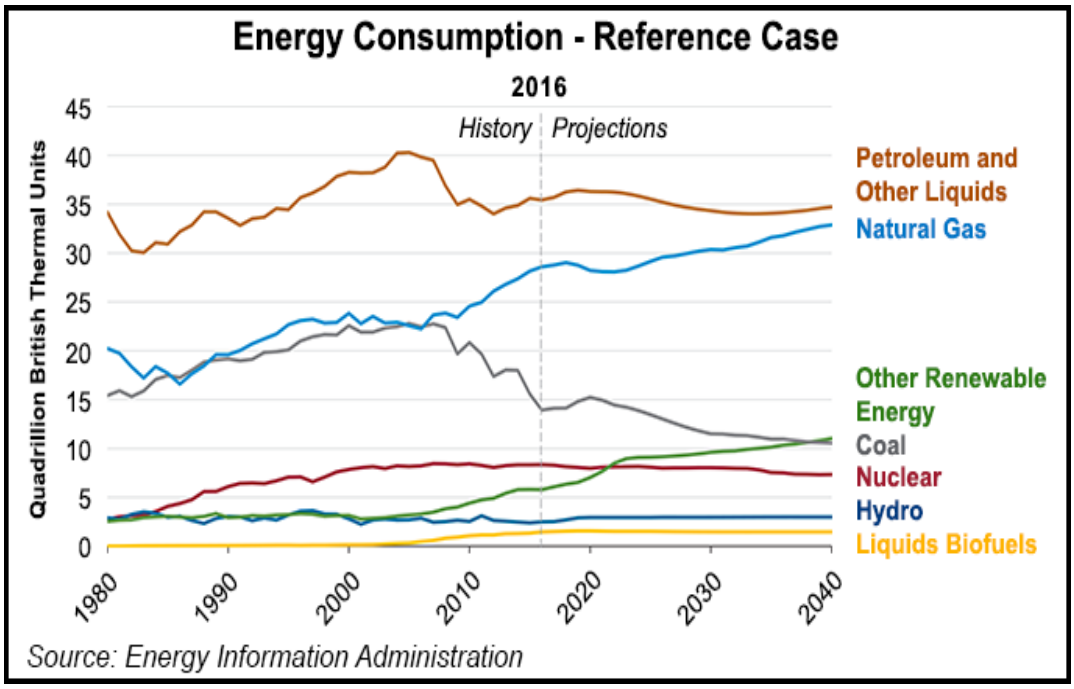

Figure 1.1 Past trends and future prospect for global energy consumption.[1]

decreased since 2007. On the contrary, it is clearly shown that energy generated from renewable source has increased continuously. Therefore, renewable energy production has been obtained more attention. There are many kinds of renewable sources such as sunlight, wind, geothermal heat, hydro power, and biomass.[6] These sources of energy have common advantages, such as non-exhaustible and rechargeable.[7] Renewable energy has been used in various fields such as electricity generation, transportation, and energy service.

Wind and solar energy are the current commercial scale eco-friendly renewable energy sources being used. Wind energy generation facilities require large amount of wind and reduction of noise pollution in the surrounding area, so there is limitation of installation space resulting in a low density of power production.[8] On the other hand, solar panels used for harvesting electricity is the fastest growing energy source int he renewable energy field. Solar panels are responsible for added 130 GW of electricity production in the world at 2017. This is due to their flexibility for installation, because sunlight accessible regardless of location.[9] Therefore, the development of technologies converting sunlight to electricity is necessary to increase usage of renewable energy. Widely used silicon solar cell is energy generator by converting photons to electricity, the photon is absorbed by the p-n junction and produces an exciton, the exciton dissociates and generates an electron and hole pair. The electron-hole pair is then transported to the external energy storage devices as shown in Figure 1.2.[10] The absorption efficiency of

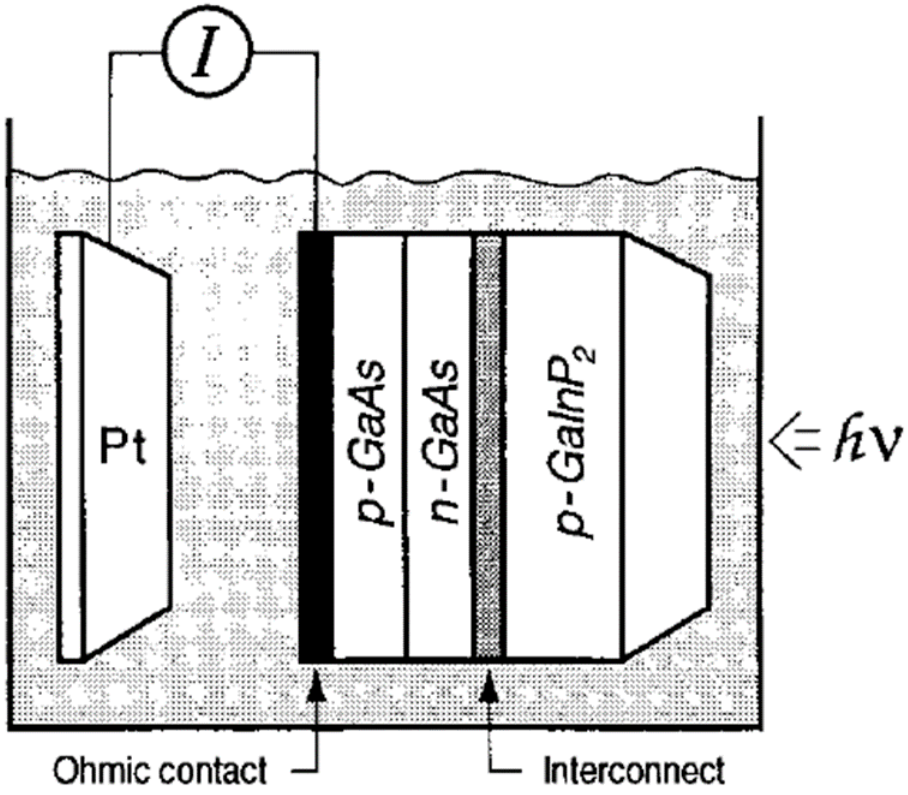

Figure 1.2 Schematic of the photoelectrochemical/photovoltaic device.[13]

absorption layer and extraction efficiency of electron determine the energy-conversion efficiency of solar cells. Silicon based solar cells are one of the most widely used solar panels due to their high-energy conversion efficiency (25%) and stability.[11] However, these solar panels have disadvantages for applications in other devices. This is because they are heavy, hard, high fabrication cost, and limited in location installation (ex: roof, mountain, desert, and sea).[12] Another type of technology that utilizes sunlight to produce a renewable energy source is hydrogen generation from water splitting. [13] Hydrogen has previously been obtained from water splitting using electricity and steam reforming of natural gas, oil reforming, and partial oxidation of coal and other hydrocarbons.[14] Water splitting driven by electricity requires a large sum of energy and causes air pollution during the extraction from fossil fuel process.[15]

Therefore, hydrogen generation from sunlight driven water splitting has gained more attention to help reduce air pollution.[13] Figure 1.3 shows the hydrogen evolution mechanism. This mechanism utilizes water and sunlight, the photocatalysts absorbs the photon from the sun and generates the electron and hole, hydrogen and oxygen gas are produced through oxidation/reduction reaction of water.[13] The generated hydrogen energy can be stored and transported and used as an energy source. The efficiency of sunlight driven water splitting is determined by the light absorption rate of photocatalysts, the separation rate of electrons and holes, and the reaction yield of electrons and proton as shown in Figure 1.3.[13] This water splitting reaction can operate using only sunlight as

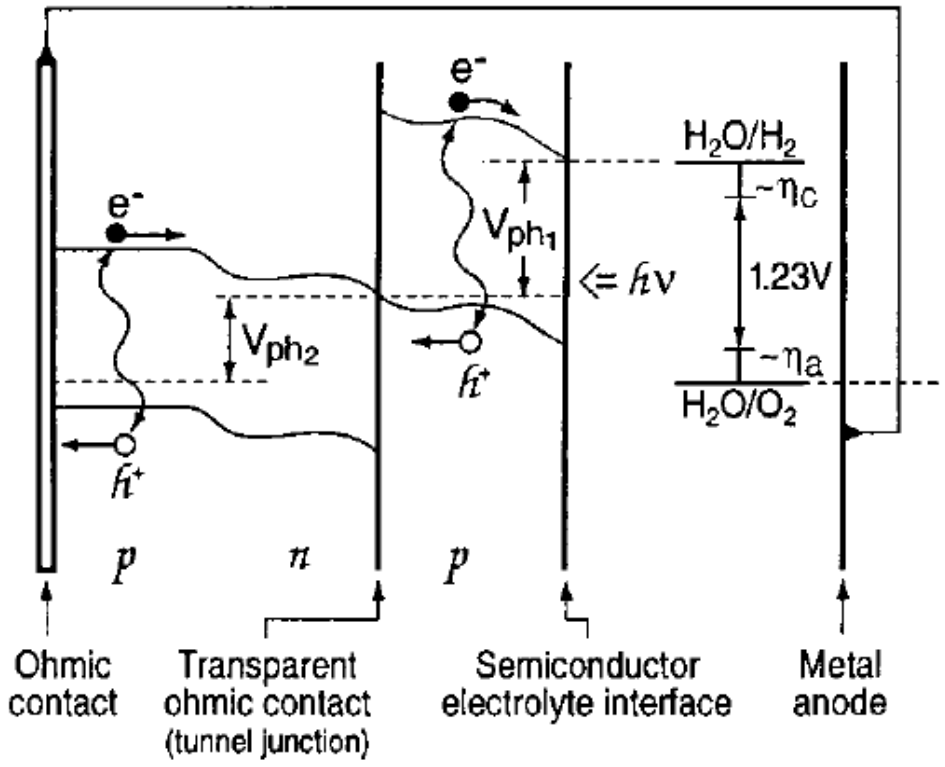

Figure 1.3 Energy diagram for photoelectrochemical cell/photovoltaic.[13]

an energy source, and does not require additional electrical energy or generate air pollutants, it also has a low disappearance rate is low when delivered to the devices. Moreover, the advantages of hydrogen fuel itself are that it generate water during combustion, there is no pollution, the amount of energy produced is very high, and the amount of energy stored per unit weight is large (e.g. hydrogen is 143 MJ/kg, gasoline is 46.4 MJ/g).[16]

1.2 Characteristics of Semiconductor

Semiconductors have gained attention due to the diversity of their structure and composition. This diversity allows for the modification of their properties and morphologies.[17] Their applications encompass semiconductor devices,[18] sensors,[19] magnetics,[20] and photonic devices.[21] Depending on the applications, the properties of semiconductors are modified by changing the structure and composition.[22] In solid state physics, the electronic band structure is an important parameter which determines the optical and electrical properties of the materials.[23] Materials are classified as conductors, semiconductors, or insulators based on their bandgap and band positions as shown in Figure 1.4[24] To understand the electronic behavior of semiconductors, there is schematic that depicts the band diagram of a semiconductor materials showing the valence band, conduction band, bandgap, and fermi level. The bandgap is the difference between levels of valence band and conduction band. The valence band is the highest range of electron

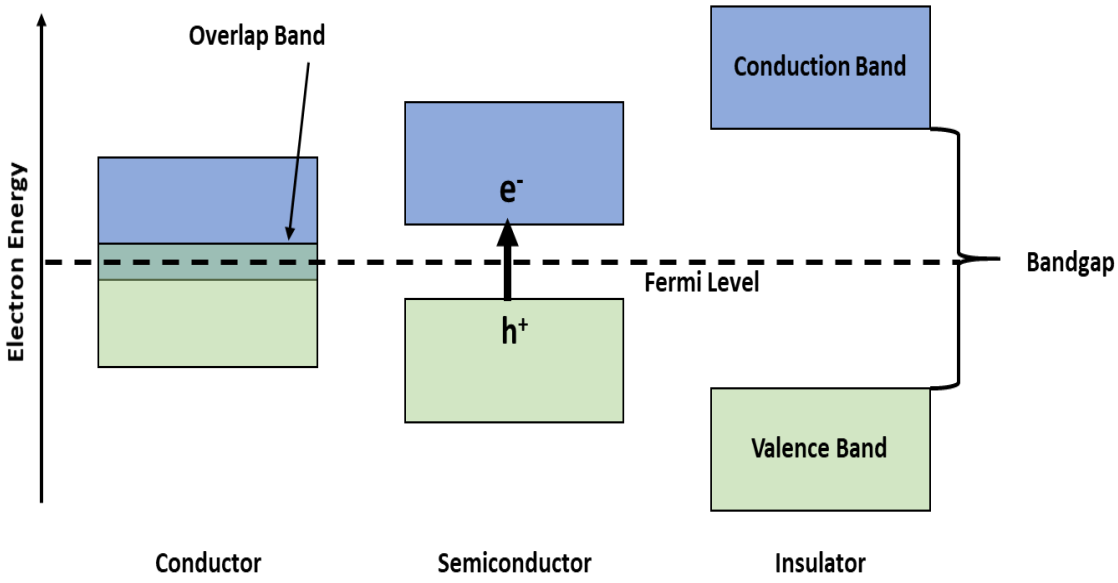

Figure 1.4 Band diagram of conductor including overlap band, semiconductor, and insulator including bandgap and fermi level.[24]

energy being occupied in the molecular orbitals and are generally full in semiconductors. The electron can jump out of the band by the external energy and move into the conduction band. The conduction band is the lowest range of electronic states that are delocalized band of energy partly filled with excited electrons from the valence band. The bandgap is the minimum energy required to excite electrons from the maximum valence band to minimum conduction band. [25] The fermi level is considered the hypothetical energy level of an electron which would have 50 % of probability of occupation.[26] Therefore, the fermi level determines the electrical properties and the type of majority carrier of the semiconductors as shown in Figure 1.5.[27] When the fermi level is located closely to the conductor band, the majority carrier is the electrons in the semiconductor whereas, when it is close to the valence band, the hole is the majority carrier.[28-30] The composition of semiconductors can be modified using doping method which is a favorable technique that controls the carrier concentration and band gap in the semiconductors. If the dopant has more valence electrons than the host atom, the amount of electrons in the lattice increases depending on the dopant concentration.[31] This additionally changes the energy distribution of the allowed states. The bandgap is changed after the instruction of dopants which produces additional states in the bandgap.[32]

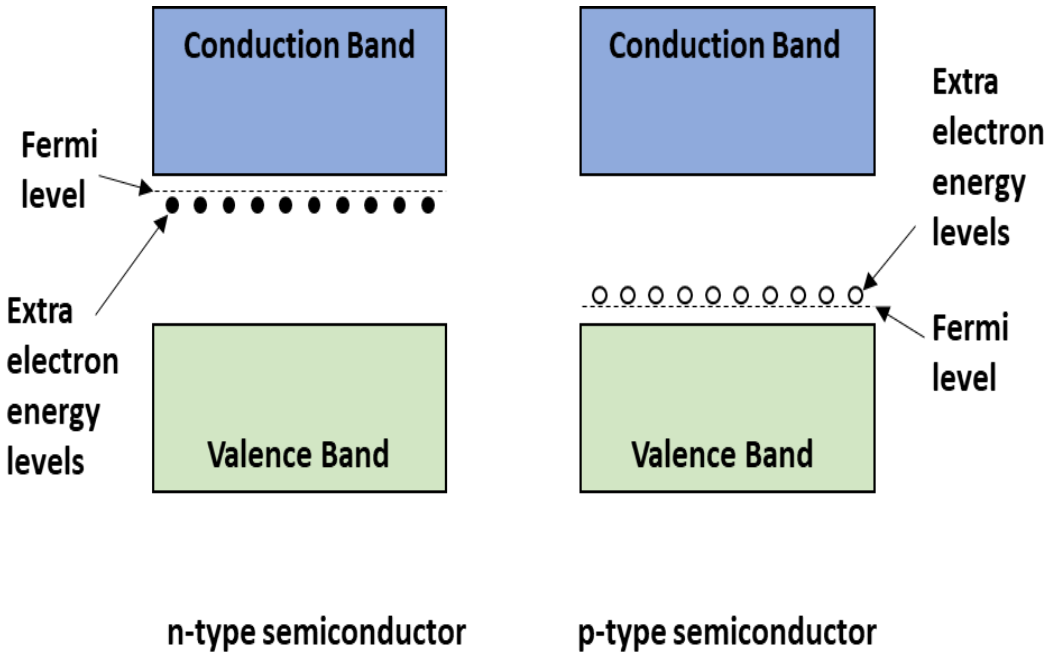

Figure 1.5 Difference between p-type and n-type semiconductor.[28-30]

1.3 Metal Oxide Semiconductor

The diverse structure and composition in metal oxides play an important role in increasing the range of device applications in comparison to silicon semiconductors, which are typically used in microelectronics[33] and solar cells.[34] Metal oxide semiconductors are used in the fabrication of transistors,[35] solar cells,[36] sensors,[37] piezoelectric devices,[38] fuel cells,[39] coating for the passivation of corrosion,[40] and as catalysts.[41] The electronic structure related to the composition of metal oxide semiconductors is tunable to satisfy application. In solid state physics, the *d*-band occupancy of the oxide combines with the metal and controls the electronic structure of the metal-oxide semiconductors as shown in Figure 1.6(a).[42] The band structures are described by using crystal field theory and ionic models of bonding. The oxides with empty d-orbitals and fermi levels close to the conduction band tend to be n-type semiconductors due to the oxygen vacancy defects. Their conduction band minimum consists of an empty metal *d*-orbital and the valence band maximum consists of O 2*p* orbitals. The oxygen deficiency generates defect states between O 2*p* orbitals and the fermi level which produces a n-type electronic structure as shown in Figure 1.6(b). Filling of empty metal *d*-orbitals produces defect states in the valence band. Figure 1.6(c) shows the electrons partially occupying the *d*-bands of oxides which have a strong electron correlation. When the *d*-band orbitals of the oxide are fully filled, it is a semiconductor that has bandgap between the *d*-orbitals of the oxide and *s*-orbitals of the bonded metal (it is not presented) as shown in Figure 1.6(d).[42] Figure 1.7 presents a band diagram of the various metal-oxide semiconductors which are p- or n-type semiconductors,

it is possible for certain metal-oxides to be used for optoelectronics such as photoelectrodes and photocatalysts.[42]

Depending on the electrical and optical properties of the metal-oxide, they are able to be applied for optoelectronic devices.[43] For example, organic-inorganic solar cells such as dye-sensitized solar cells are composed of five layers: the transparent conductive layer, the photoanode layer, an absorption layer such as an organic dye or metal-halide perovskites, the hole transport layer, and the contact layer as shown in Figure 1.8.[44] For an increased perfomrance in solar cells, the absoprtion layer has to have high absorption efficiency from the sun.[45] One of the most used metal-oxides for electron transport layers is TiO_2[46] and ZnO.[47] Visible and infrared light can pass through TiO_2 and ZnO that has a 3.2 – 3.4 eV bandgap. The electron is the majority carrier in these n-type semiconductor materials.[48] Additionally, metal-oxide semiconductors have been widely reported for their use as photocatalysts for photoelectrochemical reactions as shown in Figure 1.9.[49] Photons with a higher energy than the bandgap of metal-oxides excites the exciton. Excited electrons are available at the p-type semiconductor/liquid electrolyte interface for hydrogen evolution whereas generated holes at the n-type semiconductor are used for oxygen evoultion. The reduction potential occurs at the more positive level which produces band bending at the interface. On the other hand, the oxidation potential

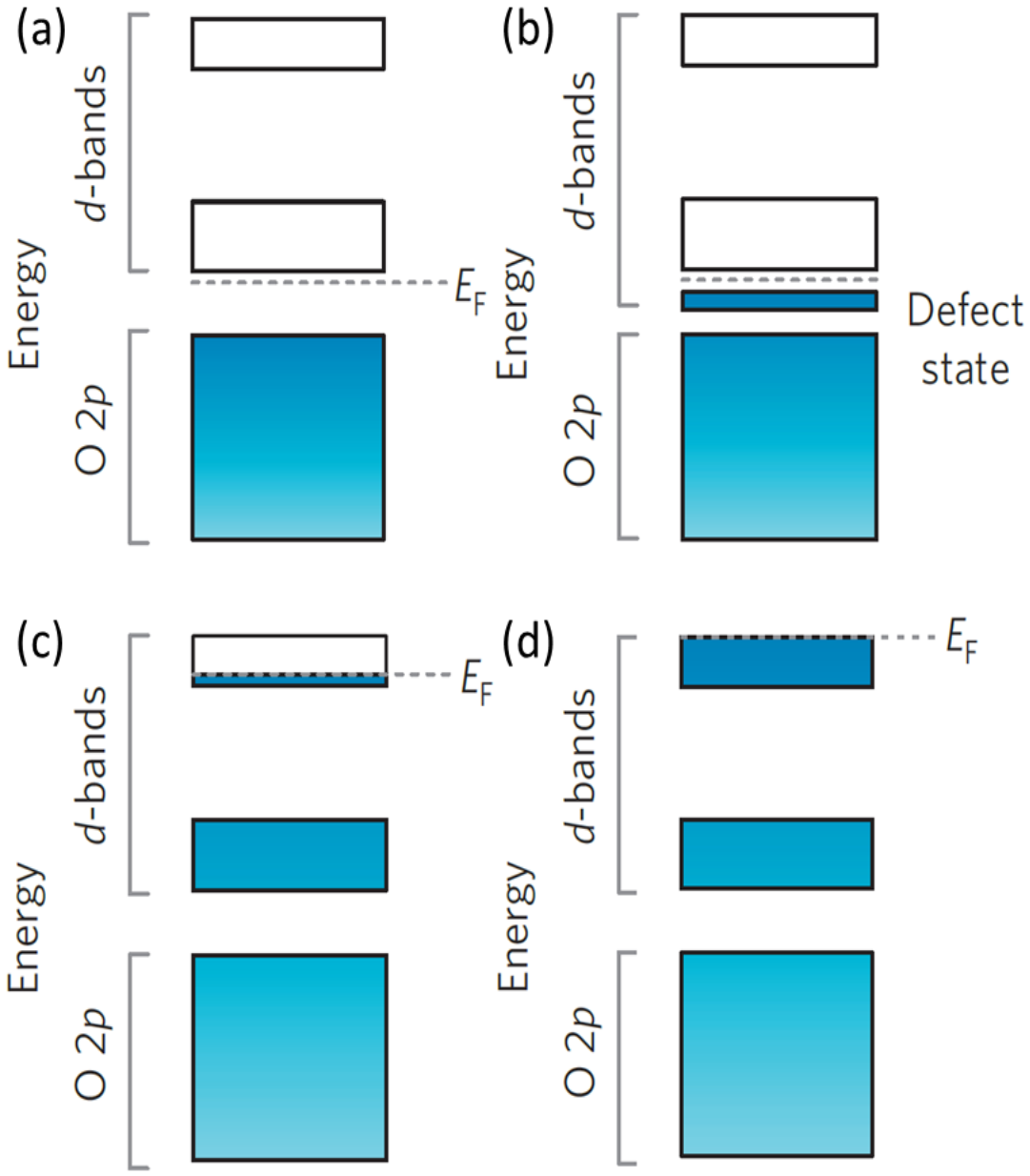

Figure 1.6 Schematic electron band diagram of valence bands arising from transition-metal oxides.[42]

Figure 1.7 Schematic representation of conduction band, valence band potentials, and bandgap energies of various semiconductor phothocatalysts and relative redox potentials of the compounds.[42]

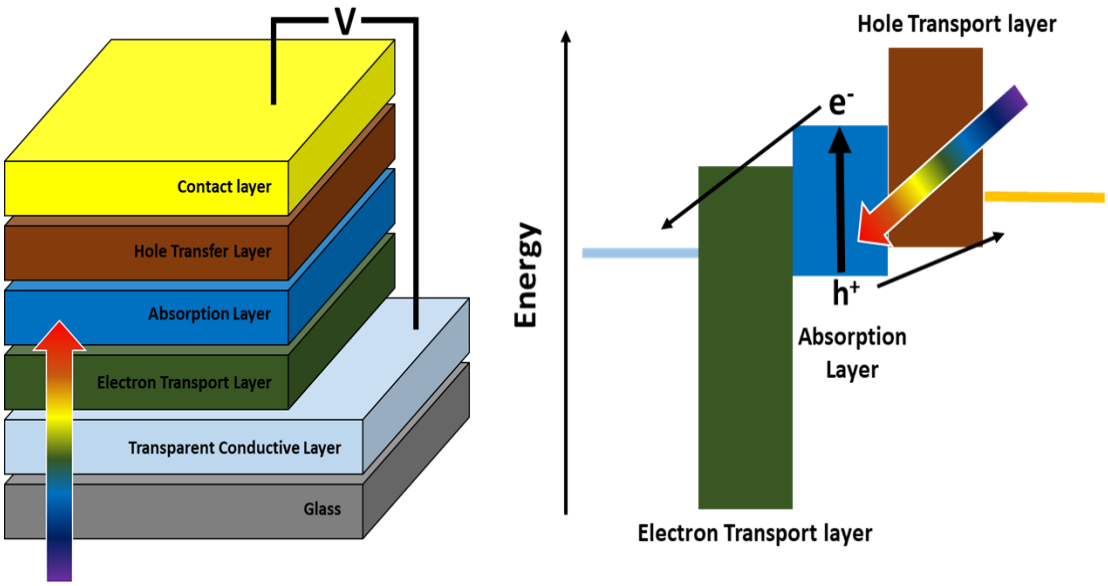

Figure 1.8 Organic-inorganic solar cells device structure and band diagram presenting an excited carrier transfer under illumination.

happens at the more negative level which generates band bending at the interface.[49] Figure 1.10 shows the band structure before and after contact between p-type semiconductor and the liquid electrolyte.[50] Figure 1.10(a) dipicts the conduction band (ECB) of the p-type semiconductor which has a more negative potential than the redox in the electrolyte before making contact. After the formation of contact between the p-type semiconductor/electrolyte, the bend edge of ECB bends towards the less negative potential as shown in Figure 1.10(b). Majority carriers (free holes) in the p-type semiconductor diffuse to the interface. As a result, there is a depleted region of majority carrier around the interface. This creates a charge depletion region, causing the band bending which has been forced away by an internal electric field at the end of the bend edge. When the internal electric field is sufficiently strong enough to suspend diffusion of the carrier, the depletion region attains equilibrium. Excitons generated by the photon are seperated into an electron-hole pair by the internal electric field in the depletion region. Excited electrons transfer to the electrolyte and hole transports into the bulk p-type semiconducton, simultaneously.[51] Therefore, when light comes in contact with the p-type semiconductor connected to the electrolyte, the excited electron transfers to the electrolyte and is available for CO_2 reduction[52] and hydrogen evoultion from water.[53] For the hydrogen evolution, the electron excited by the photon in the p-type semiconductor reacts with the proton to produce hydrogen gas in the electrolyte. This type of semiconductor materials used for photoelectrochemical reaction which donate electrons at the interface is called a photocathode. The focus of this work introduces a

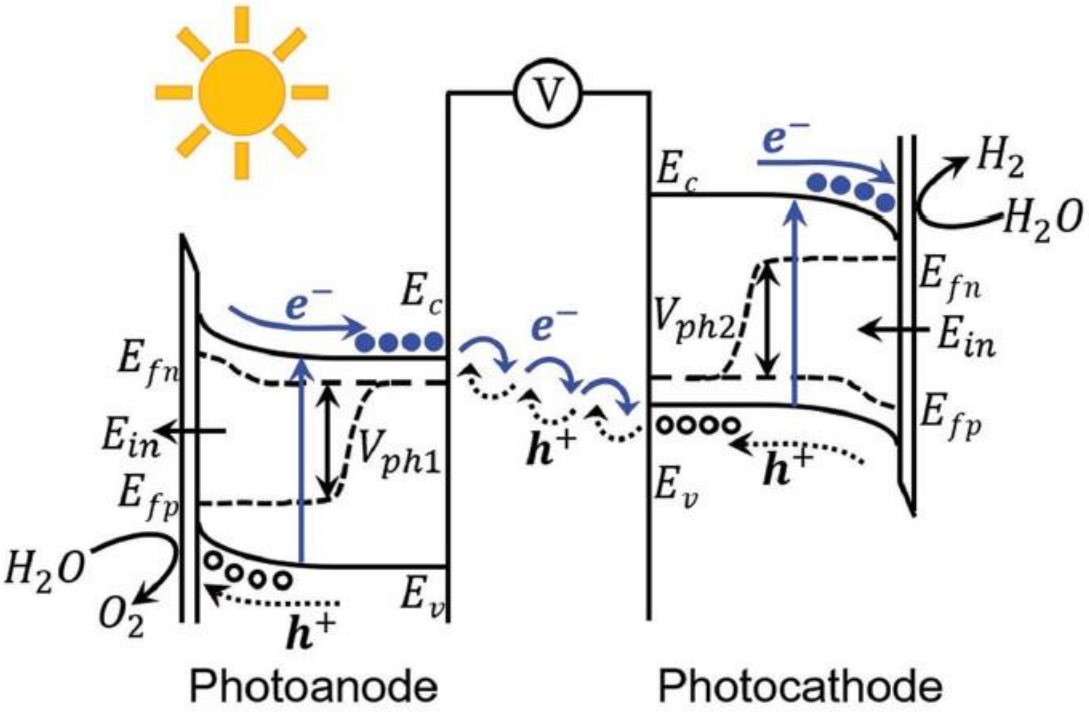

Figure 1.9 Photoelectrochemical water splitting utilizing photocathode and photoanode.[49]

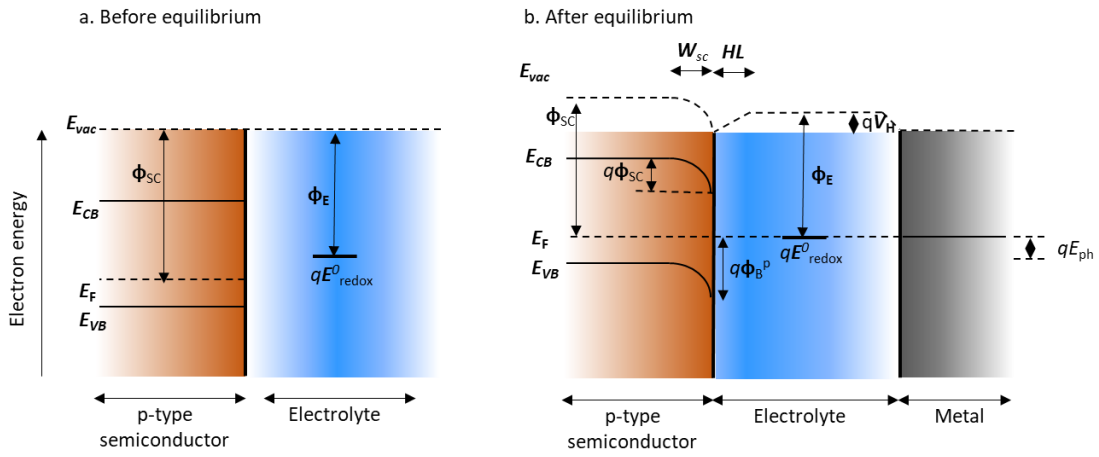

Figure 1.10 Schematic of band diagram of semiconductor/electrolyte interface (a) before and (b) after equilibrium.[50]

photocathode composed of metal-oxide for photoelctrochemical water splitting to generate hydrogen gas and photoelectrode for dye-sensitized solar cells.

Reference

[1] Annual Energy Outlook 2017 with projections to 2050, U.S. Energy Information Administration (2017)

[2] Eric W. Stein, *Renew. Sustain. Energy Rev.*, **22**, 640-654 (2013)

[3] K. Kieckhäfer, K. Wachter, and T. S. Spengler, *J. Clean. Prod.*, **162**, S11-S25 (2017)

[4] I. Burch, J. Gilchrist, Center of Climate Protection: Santa Rosa, CA, USA (2018)

[5] G. Heal, National Bureau of Economic Research (2009)

[6] M. Z. Jacobson, M. A. Cameron, E. M. Hennessy, I. Petkov, C. B. Meyer, T. K. Gambhir, A. T. Maki, K. Pfleeger, H. Clonts, A. L. McEvoy, M. L. Miccioli, A.-K. V. Krauland, R. W. Fang, M. A. Delucchi, *Sustain. Cities Soc.*, **42**, 22-37 (2018)

[7] M. M. Biswas, K. K. Das, I. A. Baqee, M. A. H. Sadi, H. M. S. Farhad, *Global Journal of researches in engineering*, 11 (2011)

[8] P. Nema, R. K. Nema, S. Rangnekar, *Renew. Sustain. Energy Rev.*, **13**, 2096-2103 (2009)

[9] P. K. Steimer, *IEEE Power Electron*., 11–5 (2010)

[10] D. M. Chapin, C. S. Fuller, and G. L. Pearson, *J. Appl. Phys.*, **25**, 676-677 (1954)

[11] S. Sharma, B. Siwach, S. K. Ghoshal, D. Mohan, *Renew. Sustain. Energy Rev.*, **70**, 529-537 (2017)

[12] A. A. F. Husain, W. Z. W. Hasan, S. Shafie, M. N. Hamidon, S. S. Pandey, *Renew. Sustain. Energy Rev.*, **94**, 779-791 (2018)

[13] O. Khaselev, J. A. Turner, *Science*, **280**, 425-427 (1998)

[14] A. Ersoz, H. Olgun, S. Ozdogan, *J. Power Sources*, **154**, 67-73 (2006)

[15] H. Ahmad, S. K. Kamarudin, L. J. Minggu, M. Kassim, *Renew. Sustain. Energy Rev.*, **43**, 599-610 (2015)

[16] K, Mazloomi, C. Gomes, *Renew. Sustain. Energy Rev.*, **16**, 3024-3033 (2012)

[17] S. T. Lee, N. Wang, C. S. Lee, *Mat. Sci. Eng.*, **286**, 16-23 (2000)

[18] A. D. Johnson, *J. Micromech. Microeng.*, **1**, 34-41 (1991)

[19] J. Xu, Q. Pan, Y. Shun, Z. Tian, *Sensor. Actuat. B-Chem.*, **66**, 277-279 (2000)

[20] S.-Y. Sung, A. Sharma, A. Block, K. Keuhn, *J. Appl. Phys.*, **109**, 07B738 (2011)

[21] K. F. Mak, J. Shan, *Nat. Photonics*, **31**, 216-226 (2016)

[22] X. Chen, S. S. Mao, *Chem. Rev.*, **107**, 2891-2959 (2007)

[23] I. Vurgaftman, J. R. Meyer, L. R. Ram-Mohan, *J. Appl. Phys.*, **89**, 5815-5875 (2001)

[24] P. Zrazhevskiy, M. Sena, X. Gao, *Chem. Soc. Rev.*, **39**, 4326-4354 (2010)

[25] A. Muñoz-Páez, *J. Chem. Educ.*, **71**, 381-388 (1994)

[26] A. Kahn, *Mater. Horiz.*, **3**, 7-10 (2016)

[27] G. Sashikesh, M. S. Ford, T. P. Softley, *J. Chem. Phys.*, **138**, 114308 (2013)

[28] West, A.R., *Basic Solid State Chemistry, 2nd edition*. 1996: John Wiley & Sons

[29] G.L. Miessler, D.A. Tarr, *Inorganic Chemistry, 3rd Edition.* 1991: Pearson Education International

[30] Nave, C.R., *Band Theory of Solids.* HyperPhysics, Department of Physics and Astronomy Georgia State University,2010

[31] P. K. Chow, R. B. Jacobs-Gedrim, J. Gao, T.-M. Lu, B. Yu, H. Terrones, N. Koratkar, *ACS Nano*, **9**, 1520-1527 (2015)

[32] Y. Gong, Z. Liu, A. R. Lupini, G. Shi, J. Lin, S. Najmaei, Z. Lin, A. L. Elías, A. Berkdemir, G. You, H. Terrones, M. Terrones, R. Vajtai, S. T. Pantelides, S. J. Pennycook, J. Lou, W. Zhou, P. M. Ajayan, *Nano Lett.*, **14**, 442-449 (2014)

[33] M. L. Green, E. P. Gusev, R. Degraeve, E. L. Garfunkel, *J. Appl. Phys.*, **90**, 2057-2121 (2001)

[34] D. E. Carlson, C. R. Wronski, *Appl. Phys. Lett.*, **28**, 671-673 (1976)

[35] I. Ferain, C. A. Colinge, J.-P. Colinge, *Nature*, **479**, 310-316 (2011)

[36] R. Jose, V. Thavasi, S. Ramakrishna, *J. Am. Ceram. Soc.*, **92**, 289-301 (2009)

[37] N. Barsan, D. Koziej, U. Weimar, *Sensor. Actuat. B-Chem.*, **121**, 18-35 (2007)

[38] T. Lim, a G. Ico,b K. Jung, ac K. N. Bozhilov, J. Nam, A. A. Martinez-Morales, *CrystEngComm*, **20**, 5688-5694 (2018)

[39] R. M. Ormerod, *Chem. Soc. Rev.*, **32**, 17-28 (2003)

[40] D. Wang, G. P. Bierwagen, *Prog. Org. Coat.*, **64**, 327-338 (2009)

[41] M. A. Vuurman, I. E. Wachs, *J. Phys. Chem.*, **96**, 5008-5016 (1992)

[42] M. T. Greiner, M. G. Helander, W.-M.Tang, Z.-B. Wang, J. Qiu, Z.-H. Lu, *Nat. Mater.*, **11**, 76-81 (2012)

[43] X. Yu, T. J. Marks, A. Facchetti, *Nat. Mater.*, **15**, 383-396 (2016)

[44] M. Z. Iqbal, A.-U. Rehman, *Sol. Energy*, **169**, 634-647 (2018)

[45] M.-S. Kim, B.-G. Kim, J. Kim, *ACS Appl. Mater. Inter.*, **1**, 1264-1269 (2009)

[46] A. L. Capodilupo, E. Fabiano, L. D. Marco, G. Ciccarella, G. Gigli, C. Martinelli, A. Cardone, *J. Org. Chem.*, **81**, 3235-3245 (2016)

[47] K. Sarmah, U. K. Roy, T. K. Maji, S. Pratihar, *ACS Appl. Nano Mater.*, **1**, 2049-2056 (2018)

[48] A. K. Chandiran, M. Abdi-Jalebi, M. K. Nazeeruddin, M. Grätzel, *ACS Nano*, **8**, 2261-2268 (2014)

[49] T. Yao, X. An, H. Han, J. Q. Chen, C. Li, *Adv. Energy Mater.*, **8**, 1800210 (2018)

[50] N. Guijarro, M. S. Prévot, K. Sivula, *Phys. Chem. Chem. Phys.*, **17**, 15655-15674 (2015)

[51] T. Hisatomi, J. Kubota, K. Domen, *Chem. Soc. Rev.*, **43**, 7520-7535 (2014)

[52] X. Chang, T. Wang, P. Zhang, Y. Wei, J. Zhao, J. Gong, *Angew. Chem. Int. Ed.*, **55**, 8840-8845 (2016)

[53] K. Sun, K. Madsen, P. Andersen, W. Bao, Z. Sun, D. Wang, *Nanotechnology*, **23**, 194013 (2012)

Chapter 2

ZnO-CuO core-shell heterostructure for improving the efficiency of ZnO-based dye-sensitized solar cells

2.1 Introduction

Photovoltaic (PV) devices are a viable technology for helping meet future energy demands, by generating electricity from the sun—a clean, renewable, and endless source of energy.[1,2] Among the various type of the photovoltaic devices, organic-inorganic solar cells are one of the most promising technologies. Si-based solar cell panels are presently widely used due to their high efficiency, cost effectiveness, and durability. Nevertheless, new technologies such as organic-inorganic solar cells are necessary to achieve wider applications of PV devices such as in cellphones, automobiles, and wearable devices.[3]

Traditionally, DSSC devices have used ruthenium-based dyes as a light absorption material. This dye can absorb ultraviolet and visible light (< 800 nm) and produce excited electrons from photon energy.[4] However, the main limitation arising from utilizing a ruthenium-based dye as an absorber is that it does not absorb infrared (IR) light (> 800nm), which accounts for 46% of sunlight.[2] This limitation of DSSCs restricts their conversion efficiency. Therefore, being able to utilize IR light has been identified as a major opportunity for improving the conversion efficiency of DSSCs.[5] Moreover, metal-oxide semiconductor materials are used as a photoelectrode in organic-inorganic solar cells. Especially for DSSCs, a semiconductor material is necessary for the transport of excited electrons from the dye to a transparent conductive substrate such as fluorine-doped tin

oxide (FTO). Among metal-oxide semiconductor materials, ZnO is one of the most commonly used photoelectrode materials, due to its high electron mobility and low recombination rate. However, ZnO shows low absorption in the IR wavelength range due to its wide bandgap energy (3.37 eV).[6,7] Alternatively, CuO is a well-known metal-oxide semiconductor material with a narrow band gap energy (1.2 eV).[8] Therefore, CuO can be adapted as a secondary material to utilize NIR light in DSSCs. Additionally, CuO can also help mitigate another major issue that impacts the conversion efficiency in DSSCs-the electron-hole recombination that takes place when the electrons at conduction band (CB) of the photoelectrode are recombined either within the dye, or in the electrolyte. Therefore, reducing the recombination rate is one important aspect to improve conversion efficiency in devices [9]

In this research, we show an improvement in the conversion efficiency of DSSCs using CuO as a secondary absorption layer for utilizing NIR light and a blocking layer for decreasing the charge recombination. The DSSCs are fabricated by using N719 commercial dye, and an iodide-based electrolyte. The photovoltaic characteristics of DSSCs using ZnO nanorods and ZnO-CuO core-shell nanostructures are compared by performing I-V measurements.

2.2 Experimental procedure

ZnO nanorods used for the core backbone structure are synthesized by CVD on commercially available FTO glass. Zn powder located upstream the FTO glass in the CVD reactor is used as a precursor material for ZnO. The CVD reactor is ramped to the reaction

temperature of 500 oC over 30 min. ramping time. Once the reaction temperature is reached, it is maintained for 30 min. The gas mixture flown into the CVD reactor is 4 sccm (oxygen), and 100 sccm (nitrogen), as the reaction and carrier gas, respectively. The CVD reactor is cooled down by natural convection after the synthesis reaction is complete. Post CVD synthesis, a 100 nm Cu seed layer is deposited on the ZnO nanorods by e-beam evaporation. The deposited seed layer is thermally oxidized in a tube furnace at 600 oC, under open environment conditions for 1 hr. For comparison and as a baseline, a Cu seed layer is also thermally oxidized on bare FTO glass for the purpose of identifying CuO peaks by XRD analysis.

During device fabrication, the synthesized ZnO-CuO core-shell nanostructure and ZnO nanorods are soaked into 0.5 mM di-tetrabutylammonium *cis*-bis(isothiocyanato) bis(2,2'-bipyridyl-4,4'-dicarboxylato)ruthenium(II) (N719) dye in ethanol solution for 70 hr. A platinum nanoparticle thin film is formed on another FTO glass by spin coating (to act as a catalyst). The two substrates (photoelectrode and counter electrode) are sandwiched and sealed with a surlyn film, with a 25 μm thickness. The gap between the two substrates is filled with an iodine-based electrolyte. The electrolyte solution is made of 0.05 M of LiI, 0.03 M of I_2, 0.5 M of 4-*tert*-Buthylpyridine and 0.1 M of guanidine thiocyanate mixed in the solvent with valeronitrile and acetonitrile solution in 1:1 volume ratio.

The surface morphology of the synthesized ZnO-CuO core-shell nanostructure and ZnO nanorods is analyzed using SEM (FEI Nova NanoSEM 450). The crystalline structure is investigated by XRD in a Panalytical X'Pert XRD instrument using Cu Kα radiation. The transmittance of the synthesized materials is measured by Varian Cary 500 double

beam scanning UV/Vis/NIR spectrophotometer (200 nm to 1500 nm). To analyze photovoltaic properties, a Xenon lamp and a semiconductor analyzer are used.

2.3 Results and discussion

As shown in Figure 2.1 (a), (b), and (c), the SEM images show different morphologies for ZnO nanorods, ZnO-Cu, and ZnO-CuO core-shell nanostructures. Figure 2.1 (a) shows that quasi-1D ZnO nanorods are synthesized by CVD on the FTO glass. The ZnO shape is hexagonal pillar and the surface of the tip is flat. The mean diameter of the ZnO nanorods is 47 nm. The morphology of the deposited Cu seed layer on ZnO nanorods is shown in Figure 2.1 (b). The surface morphology is significantly changed by the deposition of the Cu seed layer, and shows a rougher surface. This is because Cu is deposited as a cluster of particles rather than as a smooth film during e-beam deposition.

In comparison to the ZnO nanorods, the ZnO-Cu core-shell nanostructures show a wider diameter (69 nm), due to the Cu layer thickness. However, the thickness of Cu seed layer is not 100 nm due to it is calculated based on the assumption that the surface is flat. The Cu particle size is 29 nm. It can be seen that the surface area increases after Cu deposition. This is because each ZnO nanorod surface area enlarges without affecting the quantity of nanorods. Figure 2.1(c) shows ZnO-CuO core-shell nanostructures after a thermal oxidation process. The diameter of the core-shell is increased to 85 nm. The morphology of the shell is changed into a much rougher surface due to the Cu seed layer agglomerating during the oxidization.

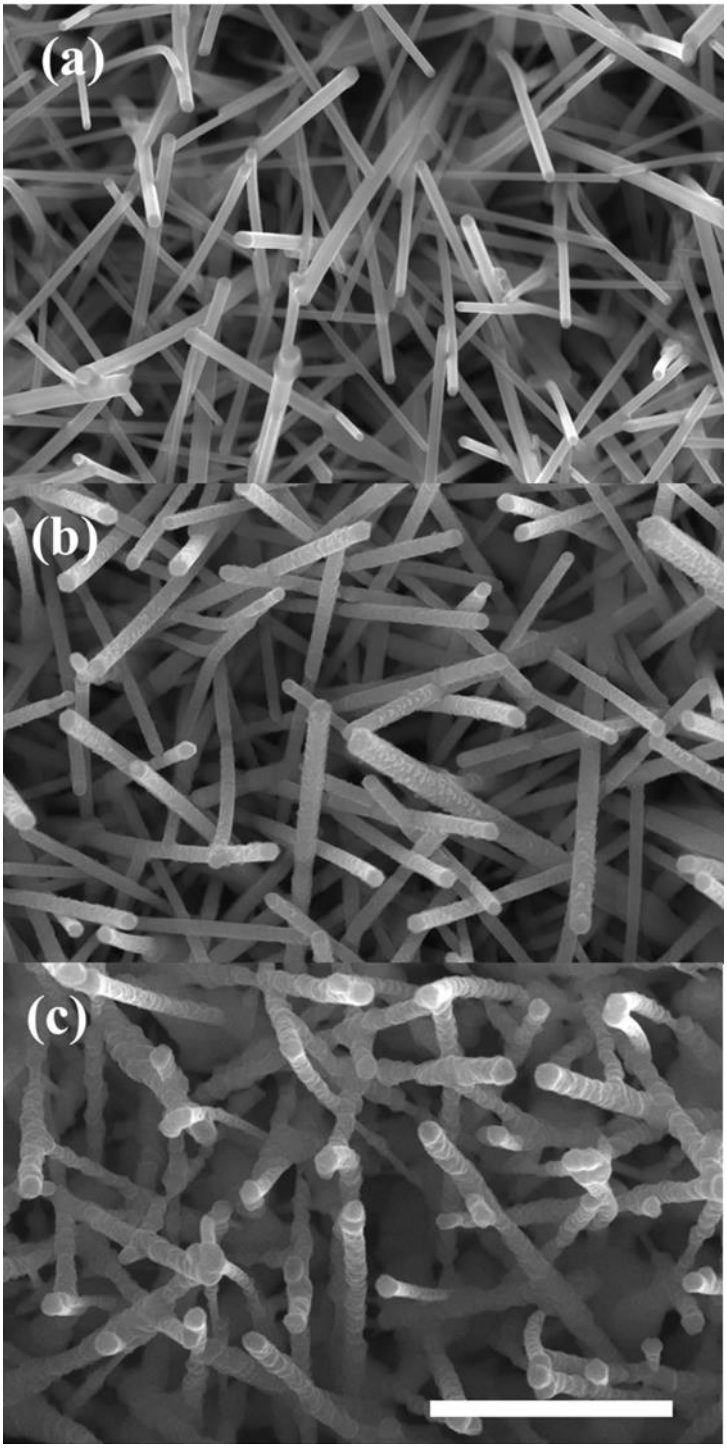

Figure 2.1 SEM images of the surface morphology of synthesized materials: (a) ZnO nanorods, (b) ZnO-Cu, and (c) ZnO-CuO core-shell nanostructures. The white bar indicates

Figure 2.2 shows the XRD patterns of ZnO-Cu core-shell nanostructure, CuO layer on FTO glass, and ZnO-CuO core-shell nanostructure from 33.0° to 45.0°. Both of the core-shell nanostructures have a typical wurtzite hexagonal ZnO crystal structure with peaks located at 34.4°, 36.2°, and 37.7°, as shown by the black and blue XRD patterns. After thermal oxidation of Cu seed layer on the FTO glass, two of CuO peaks are shown at 35.5° and 38.7°. They are correlated with [-111] and [111] directional preference. The ZnO-CuO core-shell nanostructure has ZnO and CuO peak each and there is no peak shift.

Figure 2.3 shows the optical transmittance for all samples measured from 200 nm to 1500 nm by UV-Vis-NIR photospectroscopy. The result shows light above 400 nm passes through ZnO nanorods due to its wide band gap (3.37 eV). Especially, high transmittance is observed in range of NIR (> 800 nm). On the other hand, the CuO layer on FTO glass shows low transmittance above 800 nm. This is due to the narrow band gap of CuO (1.2 eV). The ZnO-CuO core-shell nanostructure has lower transmittance than ZnO nanorods due to CuO shell assisting as an absorption layer on the ZnO nanorods. The performance comparison of DSSCs using ZnO nanorods and ZnO-CuO core-shell nanostructures is shown in Figure 2.4. Higher conversion efficiency (0.108%) is obtained by using ZnO-CuO core-shell nanostructure as a photoelectrode in DSSC compared to ZnO nanorods (0.032%). Especially, the ZnO-CuO-based device has a photocurrent density 4.2 times higher than ZnO nanorods, as shown in Table 1.

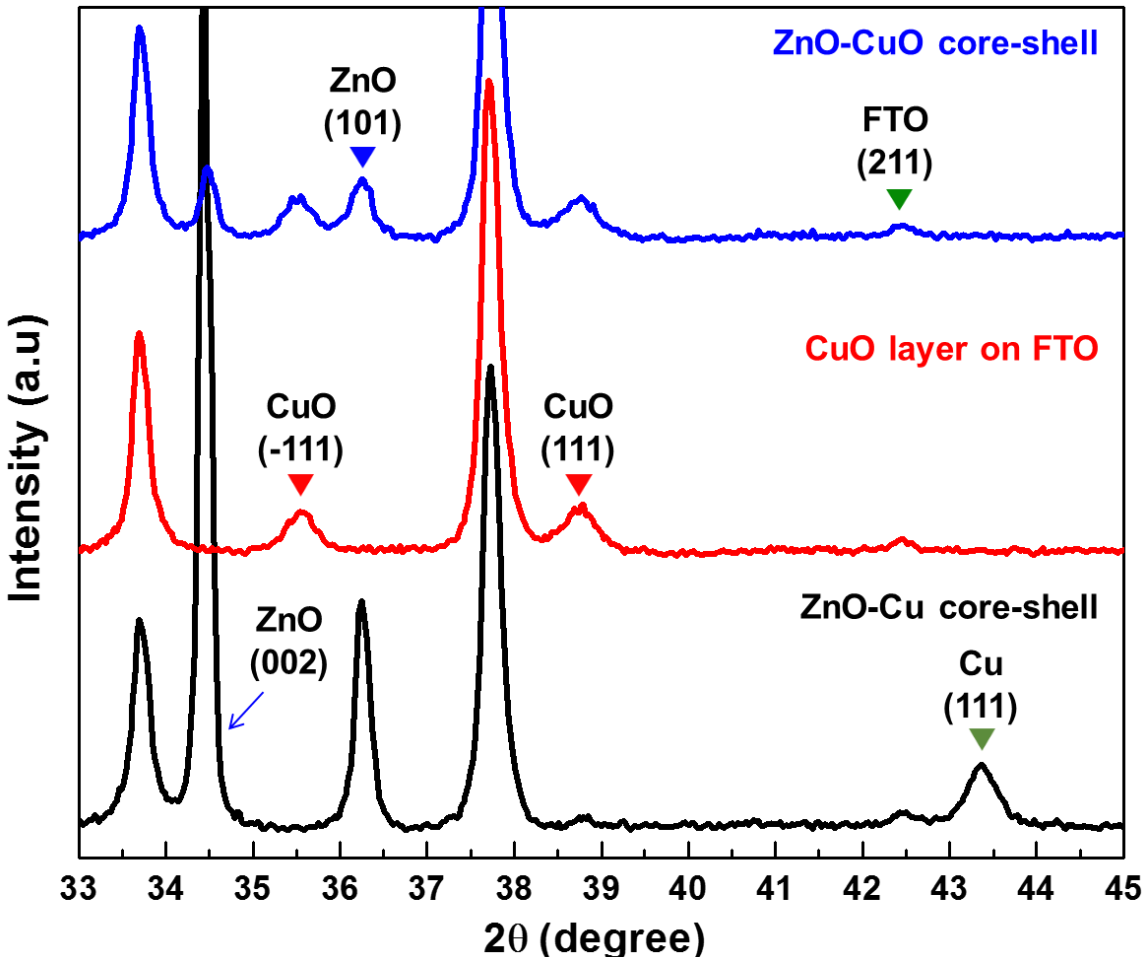

Figure 2.2 XRD pattern of the Cu-ZnO core-shell nanostructure (bottom), CuO layer on FTO glass (middle), and ZnO-CuO core-shell nanostructure (top).

The observed increased performance can be attributed to a higher photocurrent resulting from two separate mechanisms. First, the CuO shell on the ZnO core absorbs and utilizes more visible and NIR light, generating a larger number of excited electrons, as shown in Figure 2.3. Second, the CuO shell structure behaves as a blocking layer that reduces interfacial recombination by inhibiting electrons from moving back to the highest occupied molecular orbital (HOMO) of the dye, or electrolyte. Thus, minimizing current leakage paths and improving the photocurrent density in the device. This is because the CB of CuO shell (-0.84 eV vs. NHE)[10] is situated above the CB of ZnO (-0.25 eV, NHE).[11] The inclusion of the CuO shell promotes charge transfer from the dye to the ZnO photoelectrode, as shown Figure 2.5.[12] In particular, CuO prevents electron transfer from ZnO to the HOMO level of the dye and electrolyte, while thermodynamically allowing electron injection to the ZnO. As a result, the ZnO-CuO core-shell nanostructure increases the current density by reducing recombination of electrons and holes at the interface.

Furthermore, the inverse of the slope at the Voc (shown in Figure 2.4) is proportional to the series resistance of the cell. The series resistance in solar cells is affected by the movement of current from the dye, to the photoelectrode, to the FTO glass, to the metal contact. The cell using ZnO-CuO core-shell nanostructure shows an increased slope compared to the one fabricated with ZnO nanorods at the Voc, indicative of a reduction in

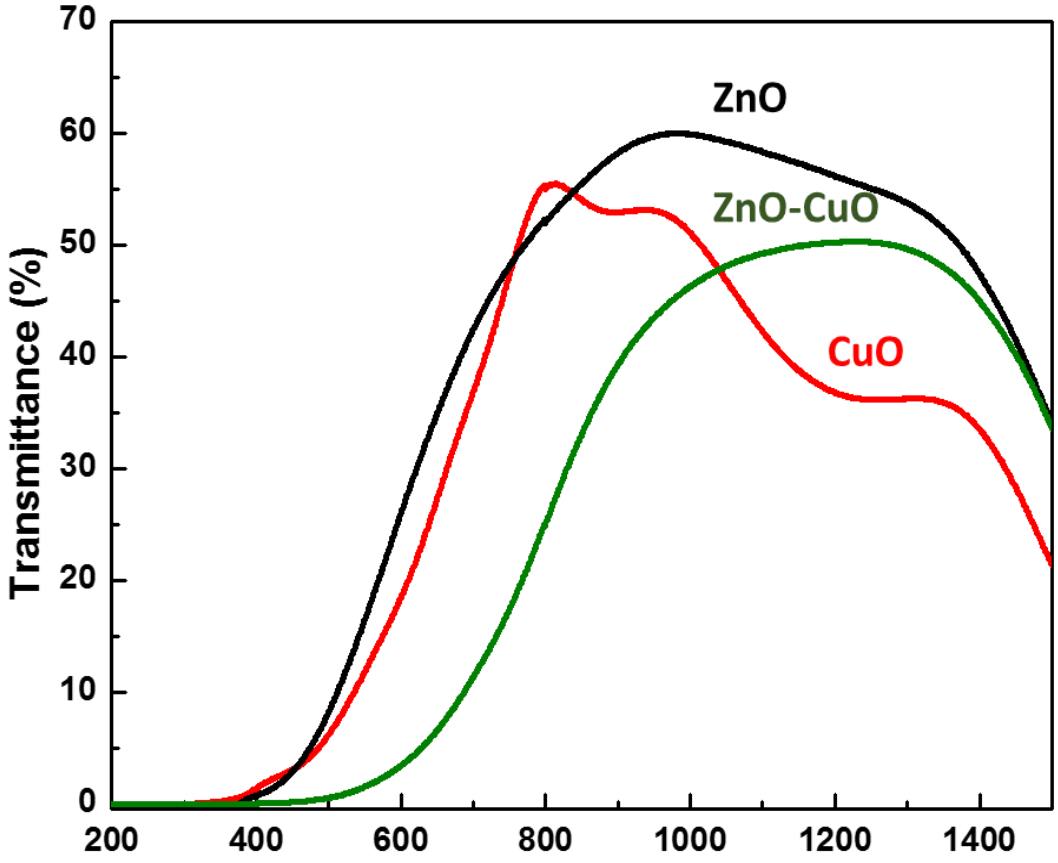

Figure 2.3 Optical transmittance spectrum of ZnO nanorods, CuO and CuO-ZnO core-shell.

Table 2.1 Solar cells parameters of ZnO nanorods and ZnO-CuO core-shell nanostructures.

Photoelectrode	J_{sc} (mA/cm^2)	V_{oc} (V)	Fill Factor	Efficiency (%)
ZnO nanorods	0.17	0.545	0.347	0.032
ZnO-CuO core-shell structure	0.72	0.456	0.328	0.108

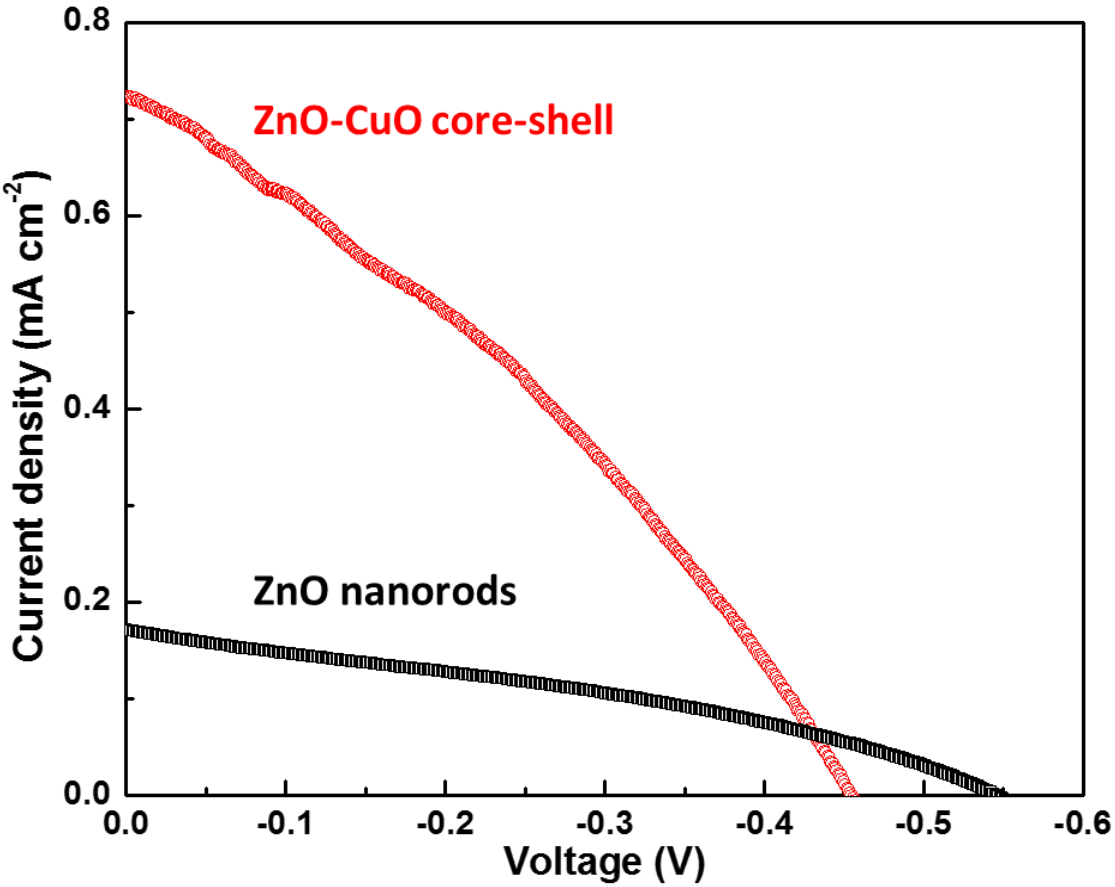

Figure 2.4 Photocurrent as a function of photovoltaic characteristics for DSSCs abricated ZnO nanorods (bottom) and ZnO-CuO core-shell nanostructure (top).

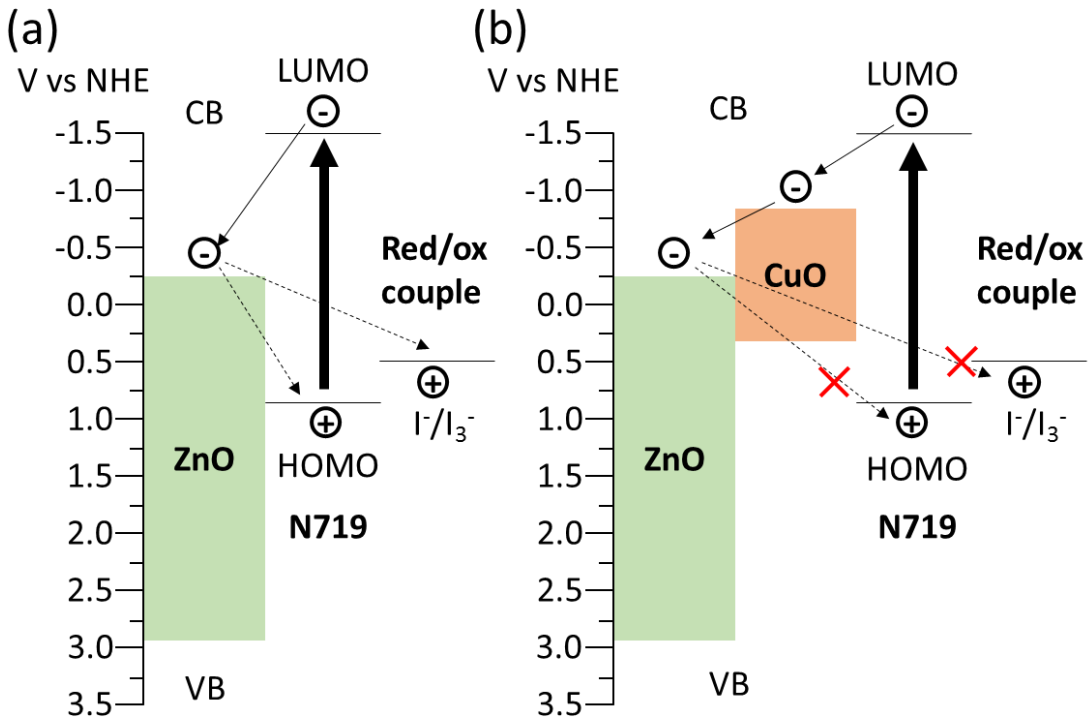

Figure 2.5 Energy diagram of (a) ZnO nanorods and (b) ZnO-CuO core-shell nanostructure as a photoelectrode in DSSCs.

series resistance. The CuO shell on the ZnO core acts as a blocking layer that leads to a lower series resistance, reducing the recombination of electron-hole pairs, and enhancing photocurrent generation.[12,13] In this work, we explore the effect of CuO layer on ZnO nanorods for 1) increasing the absorption range; and, 2) lowering electron-hole recombination.

2.4 Conclusions

In summary, we have successfully demonstrated improvement in the conversion efficiency in DSSCs using ZnO-CuO core-shell nanostructure in comparison to ZnO nanorods. The CuO shell is synthesized on ZnO by thermal oxidation. Further optimization is necessary to reduce the amount of defects during the CuO shell formation, and increase conversion efficiency. To further validate our results presented here, we will fabricate and characterize more devices to confirm repeatability and obtain average performance in terms of open circuit voltage, short circuit current, fill factor, and conversion efficiency. Future work will focus on decreasing recombination at the interface.

References

[1] M. I. Hoffert, K. Caldeira, A. K. Jain, E. F. Haites, L. D. Danny Harvey, S. D. Potter, M. E. Schlesinger, S. H. Schneider, R. G. Watts, T. M. L. Wigley, D. J. Wuebbles, *Nature*, **395**, 881-884 (1998)

[2] J. Blanco, S. Malato, P. Fernández-Ibañez, D. Alarcón, W. Gernjak, M. I. Maldonado, *Renew. Sust. Energ. Rev.*, **13**, 1437-1445 (2009)

[3] M. Wrigh, A. Uddin, *Sol. Energ. Mat. Sol. C.*, **107**, 87-111 (2012)

[4] S. Zhang, X. Yang, Y. Numata, L. Han, *Energ. Environ. Sci.*, **6**, 1443-1464 (2013)

[5] L. Han, A. Islam, H. Chen, C. Malapaka, B. Chiranjeevi, S. Zhang, X. Yang, M. Yanagida, *Energ. Environ, Sci.*, **5**, 6057-6060 (2012)

[6] O. Carp, A. Tirsoaga, B. Jurca, R. Ene, S. Somacescu, A. Ianculescu, *Carbohyd. Polym.*, **115**, 285-293 (2015)

[7] H. Cao, J. Y. Xu, D. Z. Zhang, S.-H. Chang, S. T. Ho, E. W. Seelig, X. Liu, R. P. H. Chang, *Phys. Rev. Lett.*, **84**, 5584-5587 (2000)

[8] D. Wu, Q. Zhang, M. Tao, *Phys. Rev. B*, **73**, 235206 (2006)

[9] M. Grätzel, *Inorg. Chem.*, **44**, 6841-6851 (2005)

[10] M. Woodhouse, B. A. Parkinson, *Chem. Soc. Rev.*, **38**, 197-210 (2009)

[11] S. S. Wilson, J. P. Bosco, Y. Tolstova, D. O. Scanlon, G. W. Watson, H. A. Atwater, *Energ. Environ. Sci.*, **7**, 3606-3610 (2014)

[12] P. Raksa, S. Nilphai, A. Gardchareon, S. Choopun, *Thin Solid Films*, **517**, 4741-4744 (2009)

[13] R. Sahay, J. Sundaramurthy, P. S. Kumar, V. Thavasi, S. G. Mhaisalkar, S. Ramakrishna, *J. Solid. State. Chem.*, **186**, 261-267 (2012)

Chapter 3

CuO as a multi-functional layer to improve the power conversion efficiency in DSSCs

3.1 Introduction

Society today is confronted by the an ever growing demand for energy that is driven by population growth and the increase in the quality of life of people around the world. In order to overcome this challenge, further developments and improvements in renewable energy are needed, so that more abundant, sustainable, and environmentally friendly sources of energy play a greater part in meeting our current and future energy needs.[1-5] The sun is the best source of renewable energy, because it is not only abundant but also essentially inexhaustible. Solar photovoltaic (PV) devices are one of the most efficient methods of utilizing solar energy. Solar cells utilize the sun's radiant energy as the energy source resulting in a renewable and clean supply of energy for powering human activity with lessened impacts on the environment.[6] Currently, silicon-based solar cells with energy conversion efficiencies ranging from 17-21%, and long life (> 25 years) have been widely used throughout the world and are the dominant technology in terms of deployed solar PV capacity.[7-9] However, some of the characteristics of silicon-based solar cells such as their intrinsic heavy weight and stiffness result in limitations in terms of their applications, particularly where flexibility and portability are essential. To satisfy the requirements of more versatile applications, there is a need to develop new types of photovoltaic devices, providing alternatives beyond traditional silicon solar cells[10].

Organic-inorganic photovoltaic cells such as dye-sensitized solar cells (DSSCs) and perovskite solar cells (PSCs) have attracted attention as promising technologies due to their low manufacturing cost and their applicability into a wide range of surfaces such as windows, building walls, and wearable devices. DSSCs and PSCs have the potential to become viable alternatives for silicon solar cells and merit further research and development.[10-14]

The device architecture of DSSCs consisting of a photoelectrode, counter electrode, electrolyte, and a light-absorbing material (i.e. dye) is amenable to a variety of surfaces and applications. ZnO has been applied in optoelectronic devices, including solar cells, because of its advantageous properties such as: 1) transparency in the visible light range due to its large energy band gap (3.4 eV); 2) high electron mobility of 115-155 $cm^2\ V^{-1}\ s^{-1}$; and 3) cost effectiveness.[15] Another advantage for optoelectronic applications is the ultrafast stepwise electron injection from the photoexcited Ru-complex into nanocrystalline ZnO via intermediates at the surface.[16, 17] However, a significant limiting factor for using ZnO as a photoelectrode in DSSCs is the formation of Zn^{2+}/dye complexes during soaking of the ZnO photoelectrode into the acidic dye (N-719 or N-3) solution.[18] The adsorption of formic acid (HCOOH) on the ZnO $(10\bar{1}0)$ surface weakens the Zn-O bond, which increases the bond length between Zn and O atoms, and ultimately results in the dissolution of surface Zn atoms.[19] The aggregated Zn^{2+}/dye complexes lead to an inactive layer for the electron injection from the lowest unoccupied molecular orbital (LUMO) of the dye to the conduction band (CB) of ZnO. The formation of this aggregation

increases the charge transfer resistance through the dye, negatively impacting the current density and overall power conversion efficiency (PCE) of DSSCs.[18]

In the contemporary literature, researchers have focused on a variety of methods to reduce the aggregation of Zn^{2+}/dye complexes at the surface of ZnO.[19] Engineering the surface of ZnO has been attempted as a way to improve PCE in DSSCs using ZnO as a photoelectrode. To avoid the formation of the Zn^{2+}/dye complexes, the insertion of a metal oxide layer such as TiO_2, SiO_2, MgO, and amorphous Al_2O_3 on the surface of ZnO has been demonstrated.[11-14] Particularly, an effective approach using CuO layer is preventing the interfacial recombination between an excited electron and hole on the CB energy level of ZnO and the redox potential of electrolyte.[20] The utilization of a CuO with ZnO has been reported on CuO-ZnO nanocomposites, CuO nanofibers on ZnO, and core-shell ZnO-CuO nanocomposites.[21-23] However, the stacked nanocomposite and nanoparticle structures create large number of interfacial resistance for electrons to overcome. Therefore, 1-D structures which provides direct electron pathway are desired to minimize the efficiency losses from the interfacial resistances.

In this work, we report the enhancement in the overall power conversion efficiency of DSSCs using a CuO shell on a ZnO core as the photoelectrode. The ZnO core consisting of nanorods (NRs) structures are synthesized by chemical vapor deposition (CVD). After CVD synthesis, a Cu seed layer is deposited onto the surface of the ZnO NRs, and thermally oxidized. To analyze and compare the materials at each step of the process (i.e. CVD synthesis, metal deposition, and thermal oxidation), the surface morphology, the crystallinity, and the optical properties are characterized. Two types of DSSCs devices

were fabricated, one set of devices using ZnO nanorods (NRs) only as the photoelectrode, and another using ZnO-CuO core-shell (CS) nanostructures. Since it was expected that the amount of Zn^{2+}/dye complexes formed on the surface of ZnO NRs was likely to increase with increased soaking time in the dye solution, various soaking times are used to compare the performance of fabricated DSSCs.

3.2 Experimental procedure

One dimensional ZnO NRs were grown on a F-doped SnO_2 (FTO, surface resistivity ~13 Ω/sq, Sigma Aldrich) substrate by CVD method as previously reported.[24] The FTO substrate is placed at two-thirds along the quartz tube (1400 x 72 x 4 mm; length, inner diameter, wall thickness, respectively). A small quartz tube (8.2 x 7 x 1 mm; length, inner diameter, wall thickness, respectively) with 0.2 g zinc powder (Sigma-Aldrich, <150 μm 99.995%) is placed 2 cm away from the substrate as the precursor material. A continuous flow of 97 and 3 SCCM of N_2 and O_2 are respectively used as the carrier and reaction gases. A 30 min stabilization step without heating was used to achieve a constant flowing atmosphere before the temperature was ramped up. The quartz tube was heated up to a reaction temperature of 600 °C for 30 min. The reaction temperature was kept for 30 min. The quartz tube was cooled down by the open atmosphere, without an additional cooling system. The synthesized ZnO NRs were patterned to restrict the surface area (0.16 cm^2) by photolithography. In order to remove any unnecessary area composed of ZnO NRs, 0.1 M HCl aqueous solution was used as an etchant for 20 sec. After etching the substrate was rinsed with DI water for 3 min and dried by a N_2 gun. The photoresist was completely removed by acetone and rinsed with isopropyl alcohol for 5 min. Cu seed layer was

deposited on the synthesized ZnO NRs by e-beam evaporation process to form a Cu seed layer of 100 nm. The thermal oxidation process was carried out in the quartz tube at 600 °C for 1 hour under open-air environment conditions.

Synthesized ZnO NRs and ZnO-CuO CS were soaked into a prepared dye solution consisting of 0.5 mM di-tetrabutylammonium cis-bis(isothiocyanato) bis(2,2'-bipyridyl-4,4'-dicarboxylato)ruthenium(II) (N-719 , Sigma Aldrich) dye in ethanol for 0.5, 2, and 72 hours. 50 mM chloroplatinic acid hexahydrate (Sigma Aldrich) in ethanol was spin-coated onto another FTO substrate to be used as a counter electrode in the fabrication of the DSSC devices. The deposited layer was sintered in a tube furnace at 400 °C for 30 min under open-air environment conditions. The photoelectrode and a counter electrode were sandwiched together and sealed with a surlyn film (Solaronix, 25 μm thickness). Two holes were perforated on the counter electrode through which an I^-/I^{3-} electrolyte solution was injected into the device. The electrolyte solution consisted of 0.05 M of LiI, 0.03 M of I_2, 0.5 M of 4-tert-Butylpyridine, and 0.1 M of guanidine thiocyanate in a mixture of valeronitrile and acetonitrile solvent (1:1 v/v).

Surface morphology was characterized by scanning electron microscopy (SEM, FEI NovaNanoSEM 450). Diameter of synthesized materials was measured by ImageJ program. The crystallinity of synthesized materials (ZnO NRs, ZnO-Cu CS, ZnO-CuO CS) was analyzed by PANalytical X'Pert X-ray diffraction (XRD) instrument using Cu Kα radiation. Crystal structure and elemental analysis were conducted by high-resolution transmission electron microscope (HRTEM) and electron dispersive X-ray spectroscopy (EDS) (Titan Themis 300). Ultraviolet-visible-near infrared (UV/Vis/NIR) absorption

spectra of the synthesized materials was observed by Varian Cary 500 double beam scanning UV/Vis/NIR spectrophotometer in the 300 to 1500 nm wavelength range at room temperature. Photovoltaic properties of fabricated DSSCs devices were measured using a Xenon lamp and a semiconductor analyzer. The step voltage was fixed at 1 mV. The photovoltaic properties of all devices were measured on a 0.16 cm^2 patterned active area.

3.3 Results and discussion

The morphology of synthesized materials was analyzed by SEM. Throughout SEM characterization, irrespective of the Cu deposition and/or thermal oxidation step process, no significant changes are observed in terms of the density and orientation of the NRs. The SEM images in Figure 3.1 confirm that the ZnO NRs nanostructures are stable during the high temperature thermal oxidation process. In Figure 3.1(a), the morphology of the ZnO NRs is observed to be randomly oriented on the FTO substrate with an average diameter of 39 nm. The average diameter is increased to 54 nm after the deposition of the Cu seed layer on the ZnO nanorods (Figure 3.1(b)). The observed thickness is different from the target thickness of 100 nm in the e-beam evaporation because the deposition was conducted on a non-flat surface. SEM results show that the surface morphology is changed with respect to each synthesis step. The as-synthesized ZnO NRs show a smooth surface, whereas rough surfaces are observed after both, Cu seed layer deposition and the thermal oxidized CuO. The increase in roughness resulting from the deposition of the metal seed layer is due to the Cu grains covering the surface of ZnO NRs. Figure 3.1(c) shows that the CuO layer has a rougher surface compared to the Cu seed layer on the ZnO NRs. It is expected that agglomeration of Cu takes place during the thermal oxidation process, as the

Cu seed grains have the tendency to agglomerate at high temperatures processes during thermal oxidation.[25] SEM confirms that the average diameter of ZnO-CuO CS structures is the highest among the three samples (68 nm). The diameter increment in the ZnO-CuO CS is 14 nm compared to ZnO-Cu CS.

Figure 3.2 shows the diameter distribution of ZnO NRs, ZnO-Cu CS, and ZnO-CuO CS. The average diameter of the ZnO NRs, ZnO-Cu CS, and ZnO-CuO CS are calculated from a sample number of 60 nanostructures. Compared to ZnO NRs, the histogram shows an increase in diameter at the end of the thermal oxidization process used to obtain the CuO shell.

The crystal structure and growth direction of the synthesized ZnO NRs, ZnO-Cu CS, and ZnO-CuO CS nanostructures on FTO glass are examined by XRD pattern analysis, as shown in Figure 3.3(a). Distinct diffraction peaks corresponding to the phase of FTO are found in all the samples (denoted by *). The peaks of the ZnO NRs with hexagonal wurtzite phase as the backbone material are present in all samples irrespective of whether the ZnO NRs are encapsulated by a Cu seed layer or CuO. It is worth noting that ZnO nanorods are suitable as a supporting material for the synthesis of the CuO layer by thermal oxidation at a high temperature, without inflicting any morphology change to the NRs. Figure 3.3(b) represents the detailed XRD peaks in the 2θ range of 30° to 46°. The peaks located at 34.0° and 38.1° are indexed to the (101) and (200) lattice plane of FTO, while the peaks located at 34.7° and 36.5° correspond to the (002) and (101) lattice plane of

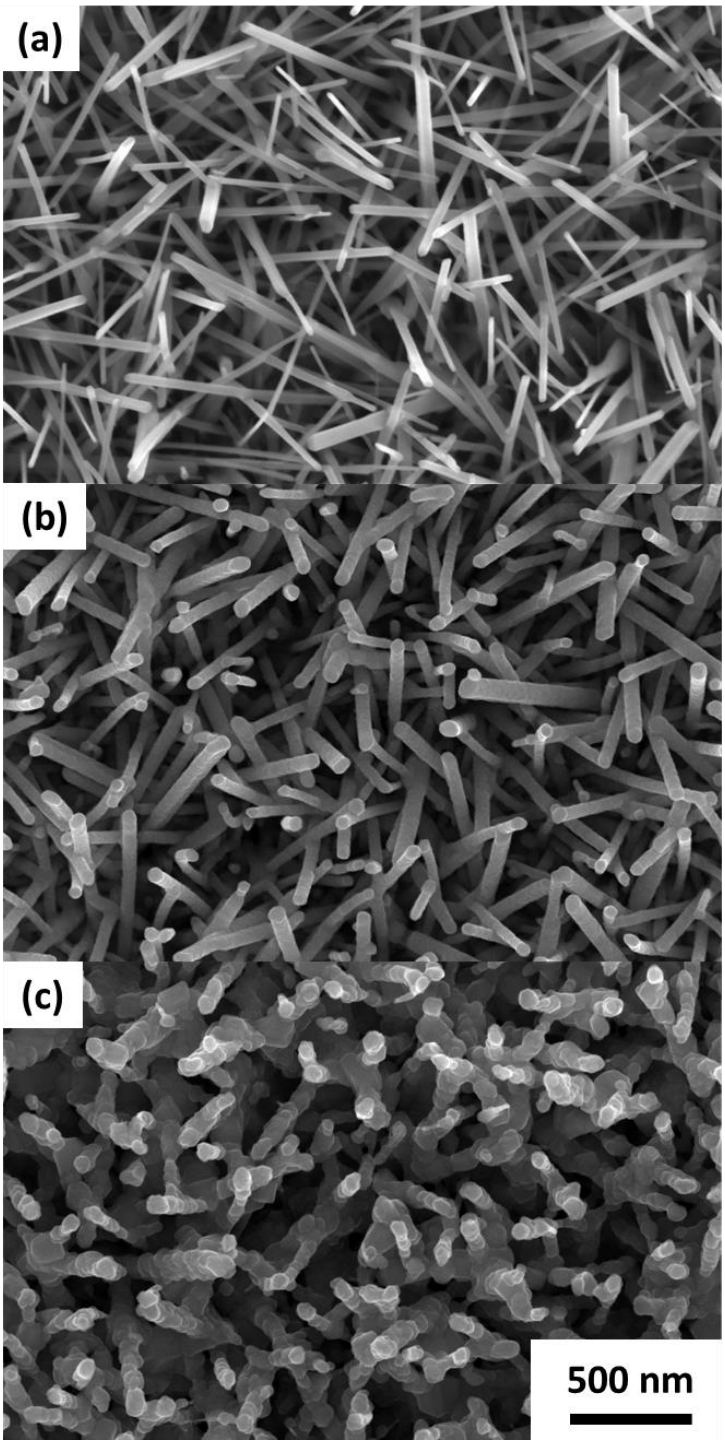

Figure 3.1 SEM images of (a) as synthesized ZnO NRs, (b) ZnO-Cu CS after e-beam evaporation of Cu seed layer, (c) ZnO-CuO CS after thermal oxidation.

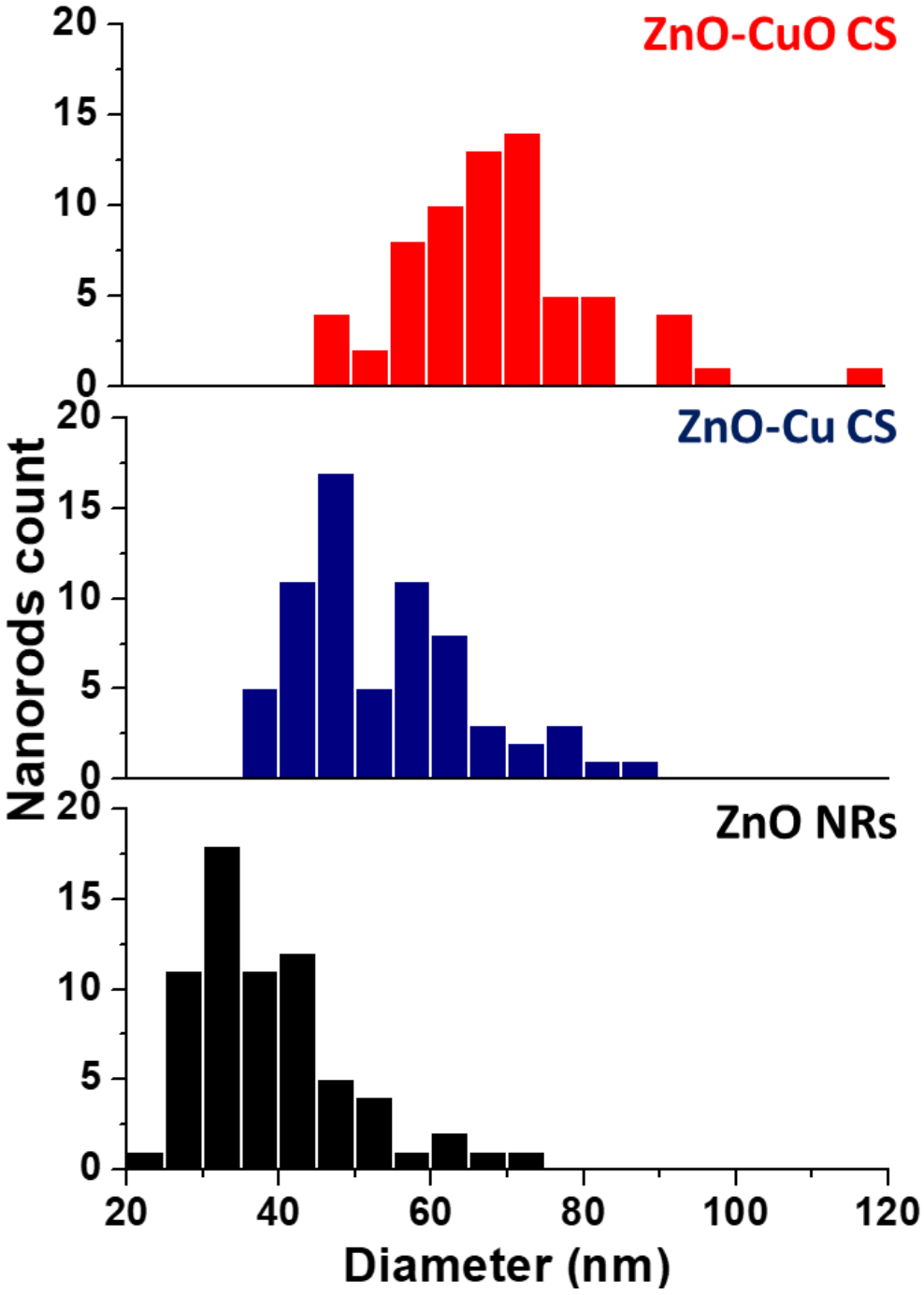

Figure 3.2 Histogram showing diameter distribution of ZnO NRs, ZnO-Cu CS, and ZnO-CuO CS.

hexagonal-phase ZnO (JCPDS card no. 36-1451; lattice parameters: a = 3.2495 Å and c = 5.2069 Å). The peak for ZnO-Cu CS is located at 43.6° corresponding to the (111) cubic Cu (JCPDS card no. 04-0836; lattice parameters: a = 3.6150 Å). The diffraction peaks of monoclinic CuO (JCPDS card no. 48-1548; lattice parameters: a = 4.68 Å, b = 3.42 Å, and 5.13 Å) are located at 35.7° and 39.0° corresponding to the $(1\bar{1}1)$ and (111) planes obtained after the thermal oxidation process. The disappearance of the Cu peak is evidence that the whole Cu seed layer is consumed during the thermal oxidation process used to synthesize the CuO layer on the surface of ZnO NRs. The XRD and SEM results provide evidence that the CuO shell is successfully synthesized on the smooth surface of ZnO core by our two-step process. For the detailed investigation of the ZnO-CuO CS nanostructure morphology, crystal orientation, and elemental composition, HRTEM image, EDS, and selected area diffraction pattern (SAED) were collected as shown in Figure 3.4. The high magnification image, in Figure 3.4(a), shows the lattice fringes of ZnO (0001) and CuO $(\bar{1}11)$ and (111). The hexagonal wurtzite zinc oxide is confirmed to have the single crystal structure ordered along [0001] direction and the monoclinic copper oxide is verified on the ZnO nanorod surface. The lattice spacing of ZnO (0001), CuO $(\bar{1}11)$ and (111) crystal planes are 0.520, 0.251, and 0.228 nm, respectively. The element mapping obtained from ZnO-CuO CS confirms that the core consists of Zn and O, while the shell is made of Cu and O element (Figures 3.4 (c) – (e)). Zn element clearly makes up the core area of the nanorod structure. Cu element is present throughout the core-shell area, with a strong Cu element signal at the shell area and a weak Cu element in the core area, indicative that the Cu element is not present in the core area. O element is observed both on the core and shell areas.

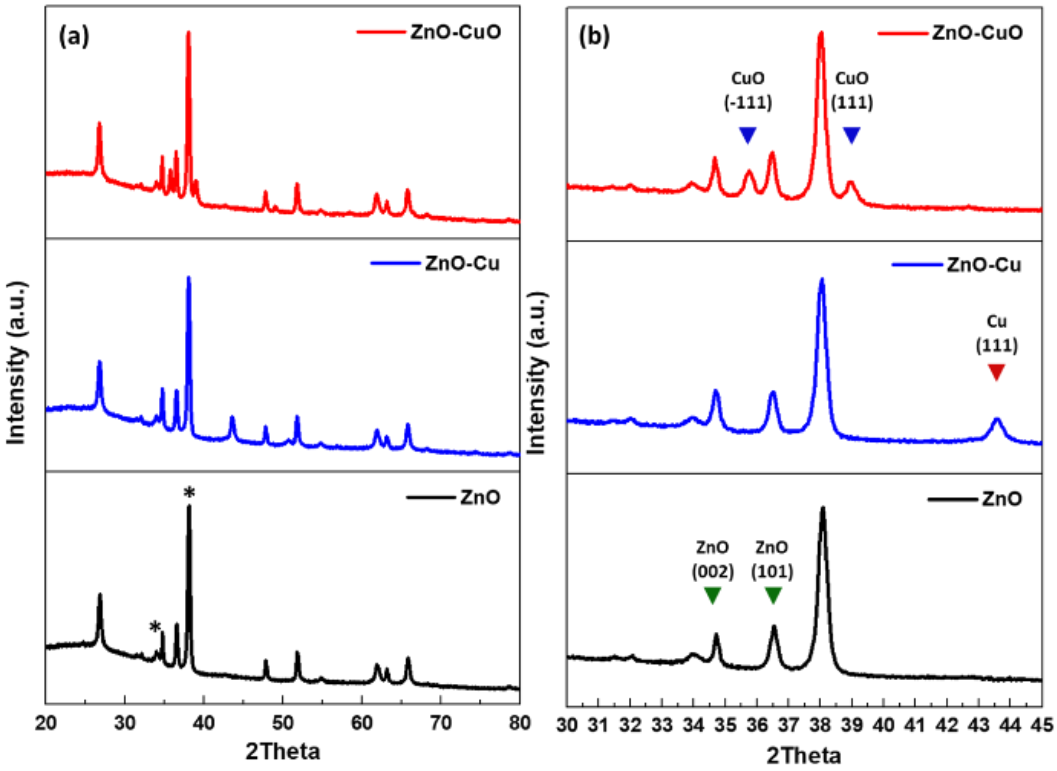

Figure 3.3 X-ray diffraction pattern (Cu Kα) of ZnO NRs, ZnO-Cu CS, and ZnO-CuO CS from 20 to 80 degree (a) and from 30 to 45 degree (b). FTO peaks are denoted by the asterisk (*).

Therefore, it is determining that the core and shell are composed of ZnO and CuO. Single crystallinity of ZnO is further supported by SAED with a well outlined spots shown in Figure 3.4(f). Figure 3.4(g) shows CuO diffraction pattern showing circular rings corresponding to a polycrystalline nature. The results from HRTEM measurement confirm that the synthesized material has a core-shell nanostructure composed of ZnO core and CuO shell.

Optical transmittance is observed by UV-Vis-NIR photospectroscopy in the range of 300 nm to 1500 nm to support the improved performance of DSSCs using CuO as a shell layer on ZnO NRs, as shown in Figure 3.5. The three samples are shown to have a low transmittance spectrum shape at the UV region due to the properties of ZnO material which absorbs UV light shorter than 400 nm. The black line representing the transmittance of the ZnO NRs shows an abrupt decrease below 400 nm while a high transmittance is observed in range of visible and NIR light (> 400 nm). This result is attributed to the band gap energy of ZnO (3.4 eV). The transmittance spectrum of the Cu seed layer deposited on the ZnO NRs reveals that no light with wavelength in the range of 300 to 1500 nm can travel (pass) through the layer. The UV-Vis-NIR results, indicate that ZnO-CuO CS nanostructures absorb light with wavelength below 1300 nm. Compared to the pure ZnO NRs, ZnO NRs with a CuO shell show a lower transmittance at the range below 1300 nm. Specifically, the transmittance of ZnO-CuO CS nanostructures show a pronounced decreased in transmittance below 1000 nm. These results confirm that CuO absorbs visible and NIR light and open the possibility for CuO to be used as a supplementary material for extending the absorption range into the NIR light range in DSSCs devices.

The current-voltage (J-V) characteristics including the J_{sc}, V_{oc}, fill factor, and PCE are measured under standard AM1.5G illumination, as shown in Figure 3.6 and Table 3.1.

The results show that the PCE and J_{sc} of DSSCs using both ZnO NRs and ZnO-CuO CS nanostructures as a photoelectrode are affected by soaking times beyond 2 hr, with the ZnO-only devices being more susceptible to the dissolution of Zn atoms in the dye. Alternatively, the V_{oc} and fill factor are both affected by the soaking time in a similar manner with a small difference between the two types of electrodes. The results show that the CuO layer on the ZnO NRs does not have a significant influence on V_{oc}. The thin CuO shell layer does not change the CB and Fermi level significantly compared to the ZnO nanorods.[26] The PCE of the DSSCs utilizing the ZnO NRs decreases dramatically with the longer soaking time. This observation was reported by M. Tachiya's and Anders Hagfeldt's groups which determined that the best PCE of DSSCs using ZnO NRs and N-3 (or N-719) as a photoelectrode and dye, respectively, was obtained from 0.5 to 2 hr soaking time. Soaking time longer than 2 hr led to the decrease of the PCE of devices.[18, 27] Since the soaking time does not affect the V_{oc} and fill factor significantly, the reduced PCE of the DSSCs using ZnO NRs is mostly arising from the reduction in the J_{sc}. This reduction in J_{sc} is attributed to the Zn^{2+}/dye complexes formed by the dissolution of Zn^{2+} ion at the surface of ZnO nanorods into the dye solution.

Figure 3.7(a) shows that the aggregation of these complexes hinders the transport of excited electrons from the dye to ZnO photoelectrode.[27] The high amount of Zn^{2+}/dye complexes increase the resistance, therefore, decreasing the charge transfer from the dye to the ZnO photoelectrode. The results confirm that the PCE and J_{sc} in devices using ZnO

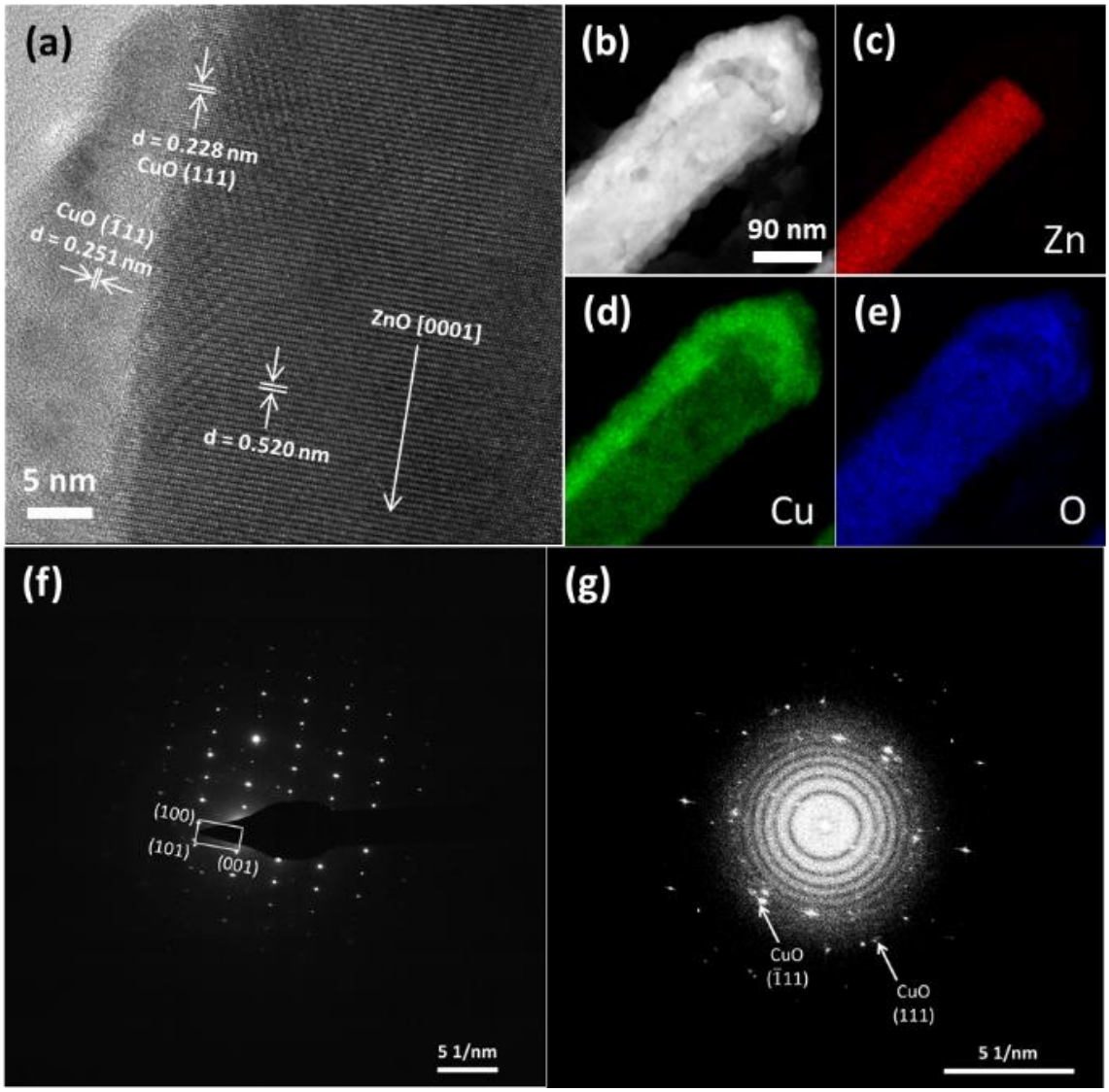

Figure 3.4 HRTEM image of (a) ZnO-CuO core-shell structure, (b) high magnification TEM image of ZnO-CuO core-shell structure; (c)-(e) element mapping; (f)-(g) SAED pattern of ZnO and CuO.

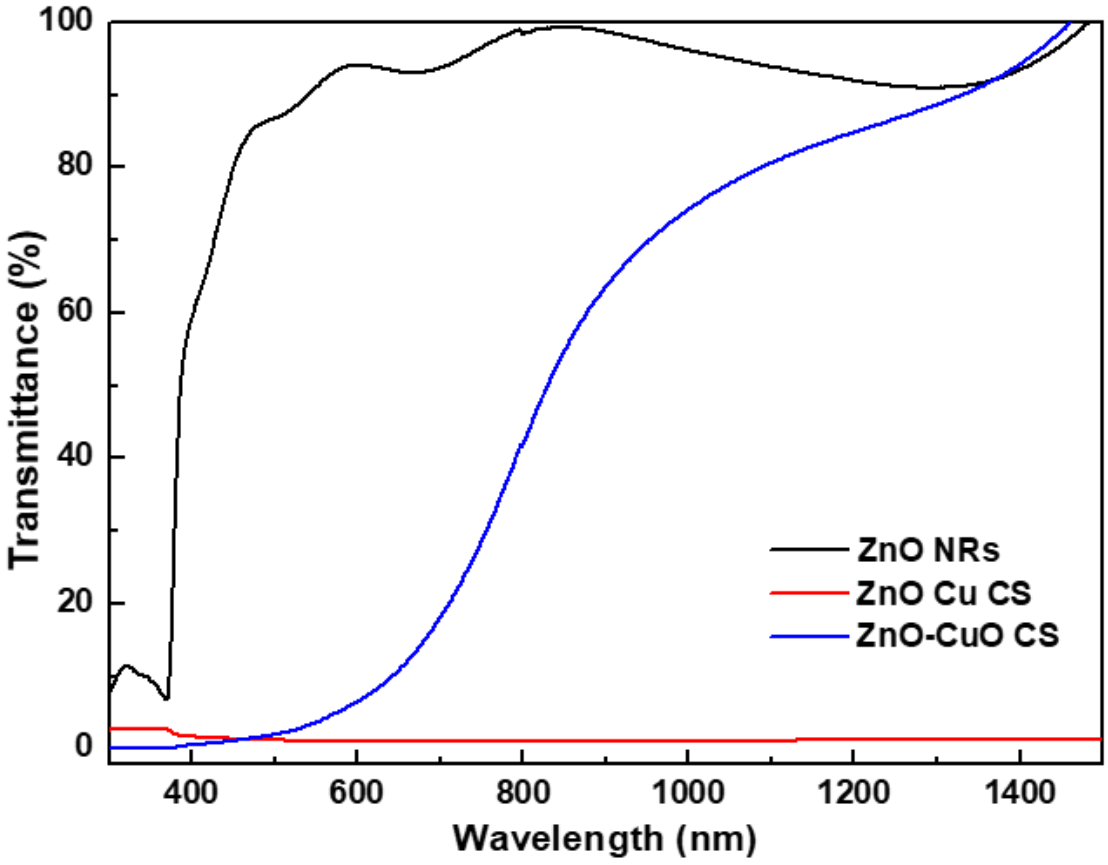

Figure 3.5 Transmittance spectra of ZnO nanorods, ZnO-Cu CS, and ZnO-CuO CS in the range of 300 nm to 1500 nm.

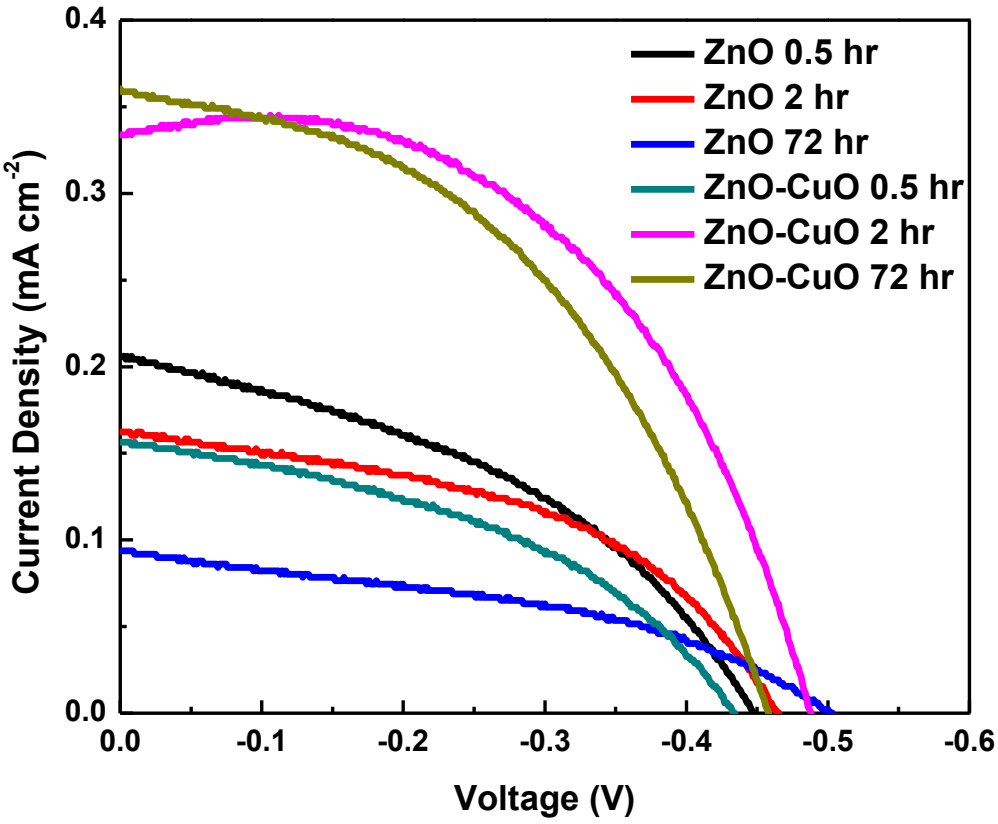

Figure 3.6 Current-voltage characteristics of as a function of soaking time into acidic N-719 dye solution under simulated AM 1.5 G, 100 mW cm^{-2} solar irradiation. The performance of DSSCs using ZnO NRs and ZnO-CuO CS is compared.

NRs decrease more significantly with longer soaking time. On the other hand, CuO layer increases carrier lifetime due to improved electron transport from N-719 dye to FTO layer and the reduced carrier recombination at the interface between ZnO and N-719 dye. Figure3.7(b) shows excited electron transfer process. The CuO layer without Zn^{2+}/dye complex prevents the recombination with holes in the N-719 dye, while it also increases the charge transfer rate and electron lifetime.[20] Therefore, the PCE and J_{sc} of the devices with the ZnO-CuO CS nanostructure increase when the DSSCs are soaked in the dye solution beyond 2 hr, all the way into a 72 hr soaking time. DSSCs using ZnO-CuO CS nanostructures have more than two times (2.3) higher J_{sc} at 2 hr soaking time versus 30 min. This is because more dye molecules are absorbed on the CuO surface within the 2 hr soaking time, while also acting as a protective layer preventing the formation of Zn^{2+}/dye complexes. Meanwhile, DSSCs using ZnO-CuO CS soaked into the dye solution for 30 min have a lower PCE and J_{sc} due to the small amount of dyes absorbed on ZnO-CuO CS. The PCE of ZnO-CuO CS devices under 72 hr soaking time decrease, while J_{sc} is higher than that of 2 hr sample. This is because V_{oc} and fill factor are shown to decrease by a small amount. Significantly longer soaking time affects the fill factor for both devices. The ZnO-CuO CS shows a lower decreasing rate in overall efficiency compared to the ZnO NRs. DSSCs using

Table 3.1 Summary of device parameters in DSSCs using ZnO nanorods and ZnO-CuO CS with various soaking time.

	Efficiency (%)	J_{sc} (mA cm^{-2})	V_{oc} (V)	Fill Factor
ZnO 0.5 hr	0.037	0.21	0.45	0.41
ZnO 2 hr	0.036	0.16	0.47	0.47
ZnO 72 hr	0.02	0.09	0.50	0.41
ZnO-CuO 0.5 hr	0.029	0.16	0.43	0.42
ZnO-CuO 2 hr	0.086	0.33	0.49	0.53
ZnO-CuO 72 hr	0.075	0.36	0.46	0.46

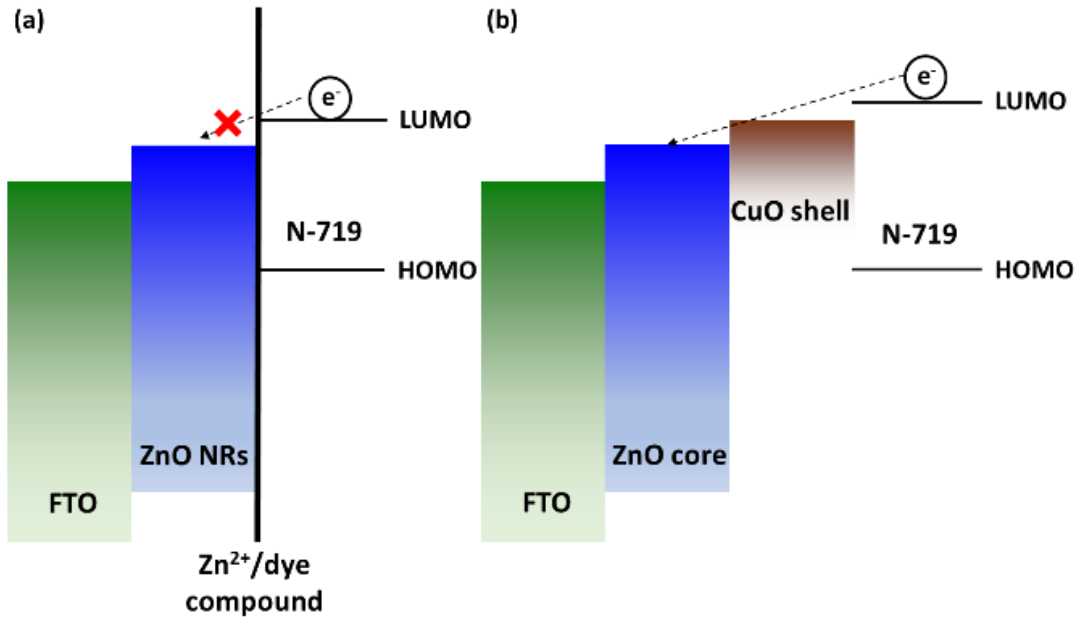

Figure 3.7 Energy level diagram of excited electron transfer from N-719 dye to ZnO photoelectrode with (a) Zn^{2+}/dye complex and (b) CuO shell.

ZnO-CuO CS after 72 hr show an efficiency drop of 11.5% compared to 2 hr soaking time. On the other hand, the efficiency in DSSCs using ZnO NRs drops by 47.2 % during the same period. The specific amount of attached dye on the CuO layer at 2 hr soaking time leads to a higher conversion efficiency in devices. While longer soaking time allows for the further absorption of more dye, it decreases overall efficiency due to the deterioration of the fill factor and saturation of the current density. These results support the conclusion that in DSSCs utilizing ZnO-CuO CS, the total amount of attached dye molecules on the CuO surface do not change much after soaking into the dye solution for a long time (i.e. 72 hr). Although there is some drop in the efficiency of devices using ZnO-CuO CS at 72 hr soaking time, fully covered CuO layer on ZnO NRs still prevents the rapid degradation in efficiency compared to ZnO NRs. This surface layer reduces Zn^{2+} ion dissolution in the solution and formation of the Zn^{2+}/dye complexes on the surface of the ZnO photoelectrode. Although a slight reduction in V_{oc} and fill factor after 2 hr soaking time is observed from DSSC using ZnO-CuO CS, this reduction arises from the change of the CuO surface over time due to minor dissolution of Cu atom in the dye. The changed CuO surface modifies the Fermi level at the (111) and ($1\bar{1}1$) planes surfaces.[28] Since the V_{oc} and the fill factor are related to the states at the band gap and surface, their values are impacted. For the V_{oc}, the modified Fermi level of the CuO surface shifts the difference from the redox potential of the electrolyte. Meanwhile, the excited electron from the CB of the CuO is released to the state in the bandgap and recombined with a hole. Despite the fact that the current density increases due to the higher amount of absorbed dye on the CuO layer after 72 hr, the changed CuO surface after longer soaking time reduces the V_{oc}, fill factor, and

conversion efficiency slightly. Similarly, increasing V_{oc} in DSSC using ZnO NRs with longer soaking time is due to the modified surface of the ZnO. The $(10\bar{1}0)$ plane of ZnO is predominant in the NRs structure. This plane is suitable to change the energy band structure depending on the surface states.[29] Therefore, the Zn atom dissolution from the surface of ZnO NRs leads to the modification of the surface states. As a result, the DSSC using ZnO NRs as a photoelectrode increase V_{oc} after longer soaking time. On the other hand, the fill factor is attributed to the surface states which inhibit the electron migration.

3.4 Conclusions

Enhanced power conversion efficiency by a factor of 2.3 times is demonstrated in DSSCs using ZnO-CuO core-shell nanostructure compared to standard ZnO nanorods used for photoelectrodes, at 2 hr soaking time. An improvement in the current density directly arises from the utilization of a CuO shell layer. This CuO layer prevents the formation of the Zn^{2+}/dye complexes formation at the photoelectrode surface which maintains effective electron injection. Although both samples show a drop in the conversion efficiency at 72 hr soaking time, the DSSC using ZnO-CuO core-shell shows a slower decrease rate compared to ZnO NRs. Using 72 hr soaking time, the DSSC using ZnO shows the enhanced V_{oc} and the decreased fill factor. The modified surface state from Zn atom dissolution at the surface of ZnO NRs affects the V_{oc} and the fill factor. Furthermore, the reduced V_{oc} in DSSC using ZnO-CuO CS is from the Cu atom dissolution while higher amount of absorbed dye on the CuO shows higher current density due to longer soaking time.

References

[1] S. Chu, A. Majumdar, *Nature*, **488**, 294 (2012).

[2] M. Grätzel, *Nature*, **414**, 338 (2001).

[3] T. Tsoutsos, N. Frantzeskaki, V. Gekas, *Energ. Policy*, **33**, 289-296 (2005).

[4] S.A. Kalogirou, *Energ. Convers. Manage.*, **45**, 3075-3092 (2004).

[5] F. Abulfotuh, *Desalination*, **209**, 275-282 (2007).

[6] N. Panwar, S. Kaushik, S. Kothari, *Renew. Sust. Energ. Rev.*, **15**, 1513-1524 (2011).

[7] Z.M. Beiley, M.D. McGehee, *Energ. Environ. Sci.*, **5**, 9173-9179 (2012).

[8] N.S. Lewis, *Science*, **351**, aad1920 (2016).

[9] J. Jean, P.R. Brown, R.L. Jaffe, T. Buonassisi, V. Bulović, *Energ. Environ. Sci.*, **8**, 1200-1219 (2015).

[10] T. Brown, F. De Rossi, F. Di Giacomo, G. Mincuzzi, V. Zardetto, A. Reale, A. Di Carlo, *J. Mater. Chem. A*, **2**, 10788-10817 (2014).

[11] M. Law, L.E. Greene, A. Radenovic, T. Kuykendall, J. Liphardt, P. Yang, *J. Phys. Chem. B*, **110**, 22652-22663 (2006).

[12] Y.-J. Shin, K.-S. Kim, N.-G. Park, K.-S. Ryu, S.-H. Chang, B. *Kor. Chem. Soc.*, **26**, 1929-1930 (2005).

[13] Y.-J. Shin, J.-H. Lee, J.-H. Park, N.-G. Park, *Chem. Lett.*, **36**, 1506-1507 (2007).

[14] N.O. Plank, H.J. Snaith, C. Ducati, J.S. Bendall, L. Schmidt-Mende, M.E. Welland, *Nanotechnology*, **19**, 465603 (2008).

[15] R. Vittal, K.-C. Ho, Renew. *Sust. Energ. Rev.*, **70**, 920-935 (2017).

[16] A. Furube, R. Katoh, K. Hara, S. Murata, H. Arakawa, M. Tachiya, *J. Phys. Chem. B*, **107**, 4162-4166 (2003).

[17] C. Bauer, G. Boschloo, E. Mukhtar, A. Hagfeldt, *J. Phys. Chem. B*, **105**, 5585-5588 (2001).

[18] R. Katoh, A. Furube, Y. Tamaki, T. Yoshihara, M. Murai, K. Hara, S. Murata, H. Arakawa, M. Tachiya, *J. Photoch. Photobio. A.*, **166**, 69-74 (2004).

[19] P. Persson, L. Ojamäe, *Chem. Phys. Lett.*, **321**, 302-308 (2000).

[20] P. Raksa, S. Nilphai, A. Gardchareon, S. Choopun, *Thin Solid Films*, **517**, 4741-4744 (2009).

[21] R. Sahay, J. Sundaramurthy, P.S. Kumar, V. Thavasi, S.G. Mhaisalkar, S. Ramakrishna, *J. Solid State Chem.*, **186**, 261-267 (2012).

[22] M.H. Habibi, B. Karimi, M. Zendehdel, M. Habibi, *Spectrochim. Acta. A.*, **116**, 374-380 (2013).

[23] A. Dhara, B. Show, A. Baral, S. Chabri, A. Sinha, N.R. Bandyopadhyay, N. Mukherjee, *Sol. Energy*, **136**, 327-332 (2016).

[24] K. Jung, T. Lim, Y. Li, A.A. Martinez-Morales, *MRS Advances*, **2**, 857-862 (2017).

[25] L. König, I. Rabin, W. Schulze, G. Ertl, *Science*, **274**, 1353-1354 (1996).

[26] Q. Xu, D. Ju, Z. Zhang, S. Yuan, J. Zhang, H. Xu, B. Cao, Sensor. *Actuat. B-Chem.*, **225**, 16-23 (2016).

[27] K. Keis, J. Lindgren, S.-E. Lindquist, A. Hagfeldt, *Langmuir*, **16**, 4688-4694 (2000).

[28] J. Hu, D. Li, J.G. Lu, R. Wu, *J. Phys. Chem. C*, **114**, 17120-17126 (2010).

[29] K. Ozawa, K. Mase, *Phys. Rev. B*, **81**, 205322 (2010).

Chapter 4

Cu_2O Photocathode with Faster Charge Transfer by Fully Reacted Cu Seed Layer to Enhance Performance of Hydrogen Evolution in Solar Water Splitting Applications

4.1 Introduction

Hydrogen is a promising renewable fuel with the potential to be used as an energy source to alleviate the higher demand for energy driven by population growth. Hydrogen has a high mass energy density and is an eco-friendly material. These two characteristics make it an attractive energy source for addressing current and future energy needs.[1] The efficient and cost-effective harvesting and storing of hydrogen gas are critical for its utilization across various fields and applications.[2,3] The use of photoelectrochemical (PEC) cells for water splitting applications as a method to efficiently harvest hydrogen gas using solar energy has been carried out extensively by various research groups.[4-6] PEC cells convert sunlight to chemical energy by splitting water molecules for generating hydrogen gas.[6-9] Therefore, research focused in improving the efficiency in PEC cells is imperative to make hydrogen a more competitive technology. Among materials used to produce hydrogen gas using PEC cells, Cu_2O is a good candidate because it is cost-competitive and an abundant material in the earth.[10-15] Cu_2O is a p-type semiconductor material with a band gap of 1.6 - 2.2 eV, absorbance in the visible light range (563 - 775 nm), and a suitable band edge alignment that is amenable for generating chemical energy.[16-18] In a PEC device, the absorbed sunlight at the Cu_2O surface generates excited

electrons by reducing protons to hydrogen gas at the interface between the photoelectrode and the electrolyte.[10-11,13-15]

Cu_2O has a theoretical hydrogen conversion efficiency of 18% in PEC cells and a power conversion efficiency of 20 % in a solar cell.[12,15] However, low hydrogen generation and instability are two challenges that prevent the usage of Cu_2O as a photocathode in PEC cells.[19] The low efficiency is attributed to the high charge recombination caused by the slow carrier transfer rate at the Cu_2O surface.[20] To increase the efficiency of Cu_2O, a thick film around 10 μm is necessary for the effective absorption of sunlight.[21,22] However, minority carrier (electrons) in the Cu_2O reacting with protons have less than a 200 nm diffusion length, resulting in an inefficient reaction.[23] The charge diffusion length and the carrier transfer rate are important factors to improve the efficiency of hydrogen gas generated from excited electrons.[24] In the literature, the properties of Cu_2O have been engineered for increasing the charge diffusion length and improving the carrier transfer rate as well. There are various research methods to improve Cu_2O performance such as doping,[25] high temperature processing for enhancing the crystal quality,[11] engineering an overlayer,[12,26-28] and modifying the morphology to reduce the electron pathway length.[29-30] Despite these efforts to improve the generation efficiency, the utilization of Cu_2O still requires more research to improve its low photocurrent density in PEC cells.

In this paper, we report the improved hydrogen generation properties of textured Cu_2O photocathode film, via the full reaction of the Cu seed layer between the Cu_2O and the

fluorine doped tin oxide (FTO) substrate. The textured Cu_2O has a higher PEC efficiency due to its larger surface area compared to thin-film structures. Via our solution base synthesis method, we successfully synthesized a textured Cu_2O film on FTO substrate from a Cu seed layer film. When Cu_2O is used as a photoelectrode, any unreacted Cu greatly impacts the hole transfer in the PEC cell. In this work, the relationship between electron/hole recombination and carrier transfer rate is investigated. Photoelectrochemical reaction measurements are analyzed to determine the reaction at the interface between Cu_2O and electrolyte. The material properties are characterized in terms of their morphology, crystallinity, and light absorbance.

4.2 Experimental procedure

All chemicals in this paper are purchased from Sigma Aldrich. FTO on glass substrate (surface resistivity ~13 Ω/sq, Sigma Aldrich) is used as a substrate. FTO is cleaned using a detergent solution in deionized (DI) water, acetone, and isopropyl alcohol (IPA) in an ultrasonication bath for 5 min for each step. A nitrogen gun is used to dry the FTO after the IPA rinse. A Cu seed layer is deposited by e-beam evaporation on the FTO substrate patterned with a 1 x 1 cm^2 window. The deposition rate is maintained at less than 1.2 Å/sec. Various Cu film thicknesses are deposited. These samples are denoted sample 1, 2, 3, and 4. The solution for making the textured Cu_2O is prepared as detailed by Chattopadhyay's group.[10] The initial solution is mixed with 0.038 M ammonium persulfate ($(NH_4)_2S_2O_8$) and 0.191 M sodium hydroxide (NaOH). The reaction solution is prepared by adding 4 ml in 160 ml DI water. The solution is stirred until fully mixed. The

prepared samples with Cu seed layer are dipped into the solution for 1 hr at room temperature without stirring. The residue on the surface of sample is rinsed by DI water for 5 min and dried by nitrogen gun. The samples are annealed by rapid thermal annealing at 550 °C for 1 min under nitrogen condition. In order to compare the surface morphology of a flat uniform film (as a control sample), a Cu film on FTO glass is thermally oxidized at 600 °C for 1 hr under air.

The morphology of the synthesized materials on the FTO glass are characterized by scanning electron microscopy (SEM, FEI NovaNanoSEM450) and atomic force microscopy (AFM, MFP-3D from Asylum Research). Crystallinity of the samples is analyzed by X-ray diffraction (XRD, PANanlytical X'Pert X-ray diffractometer) using Cu Kα radiation (1.540598 Å). Optical properties are measured by double beam scanning UV-Vis-NIR spectrophotometry (Varian Cary 500).

Photoelectrochemical performance of the synthesized samples, as photocathodes for PEC devices, is measured by a potentiostat with a 3-electrode setup using Ag/AgCl/KCl as the reference electrode, Pt wire as the counter electrode, and the synthesized film as the working electrode. 0.1 M Na_2SO_4 electrolyte solution is used for the testing of the PEC. A solar simulator (Newport, Oriel Sol3A Class AAA Solar Simulator, 450 W Xenon) is used as the light source (AM 1.5 G, 100 mW cm^{-2}). The solar simulator was calibrated by a monoclinic silicon solar cell (Newport, Oriel® Reference Solar Cell & Meter, 91150V). The scan rate for the linear sweep voltammetry is 0.05 V/s and the applied potential is -0.05 to 0.4 V vs. RHE. Electrochemical impedance spectroscopy (EIS) is conducted at

open circuit potential from 10^5 to 10^{-1} Hz frequency under illumination to study interfacial charge transfer between the photocathode and the electrolyte. Measuring the capacitance against potential at 10^3 Hz frequency is performed under dark from 0.2 to 0.6 V vs. RHE to characterize the V_{fb} potential.

4.3 Results and discussion

Four samples with different thickness are synthesized via a solution method. The synthesized samples show a textured Cu_2O film on the FTO substrate as observed by scanning electron microscopy (SEM) characterization shown in Figure 4.1 and Figure 4.2. The morphology of these samples is rougher than the CuO layer synthesized on FTO substrate by thermally oxidizing the Cu seed layer shown in Figure 4.3. In contrast to the CuO film which maintains the FTO surface topography, the Cu_2O forms a morphology that is independent of the FTO substrate. The samples show that the textured Cu_2O films have a peak to peak distance around 80 nm as shown in Figure 4.4 and Figure 4.5. Although the thickness of the Cu seed layer is different for each sample, the atomic force microscopy(AFM) topography results show a similar root mean square roughness value for all samples, ranging from 17 to 20 nm. This is evidence that the synthesized Cu_2O films on the FTO substrate have a similar morphology regardless of the starting Cu seed layer thickness. However, the cross-sectional SEM images show that the resulting thickness of the Cu_2O layer on the FTO substrate is limited by the reaction time of solution-based synthesis process shown in Table 4.1. The combined thickness of the unreacted Cu and

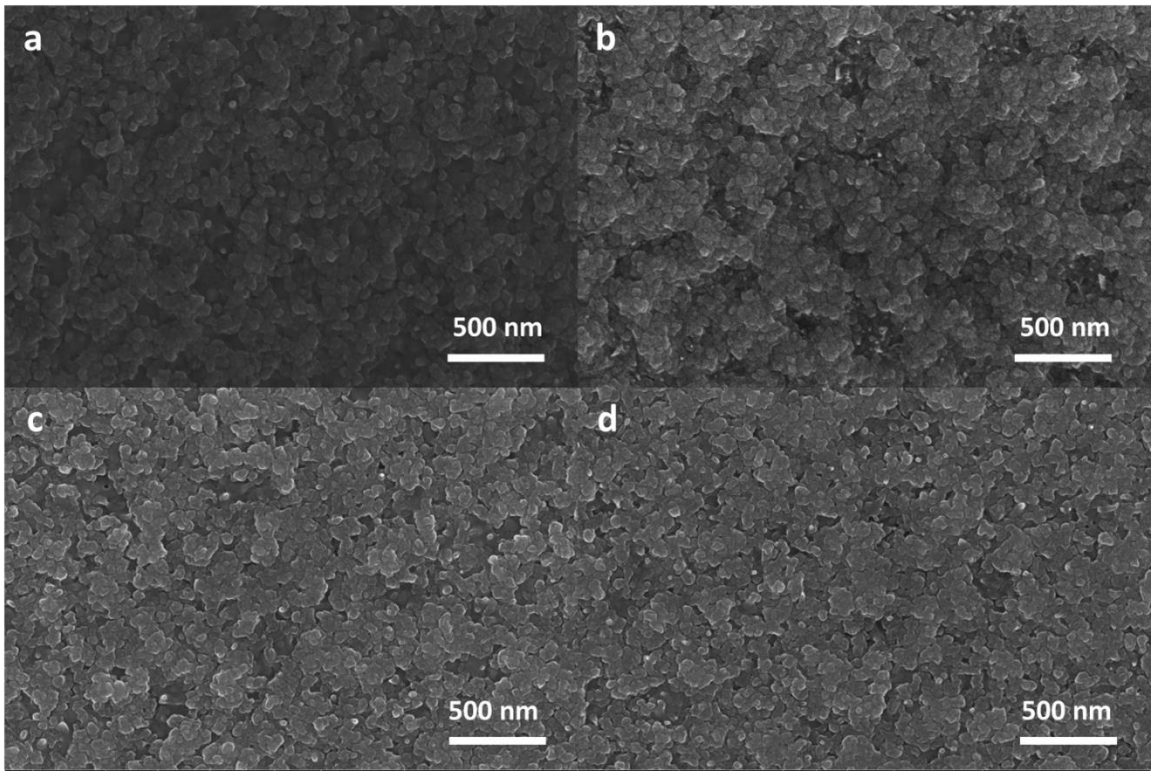

Figure 4.1 Comparison of Cu_2O samples with different thickness. Top-view scanning electron microscopy images of the (a) Cu_2O-100, (b) 200, (c) 300 and (d) 500 nm.

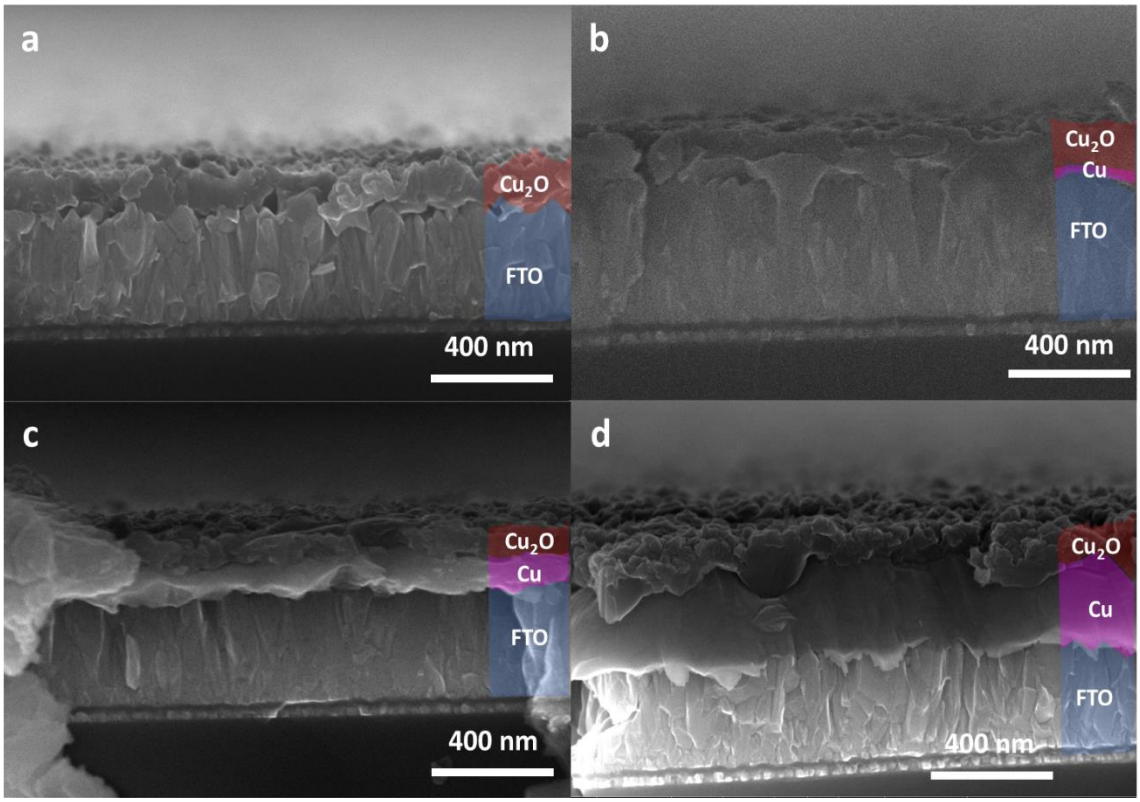

Figure 4.2 Comparison of Cu_2O samples with different thickness. Cross-sectional scanning electron microscopy images of the (a) Cu_2O-100, (b) 200, (c) 300 and (d) 500 nm.

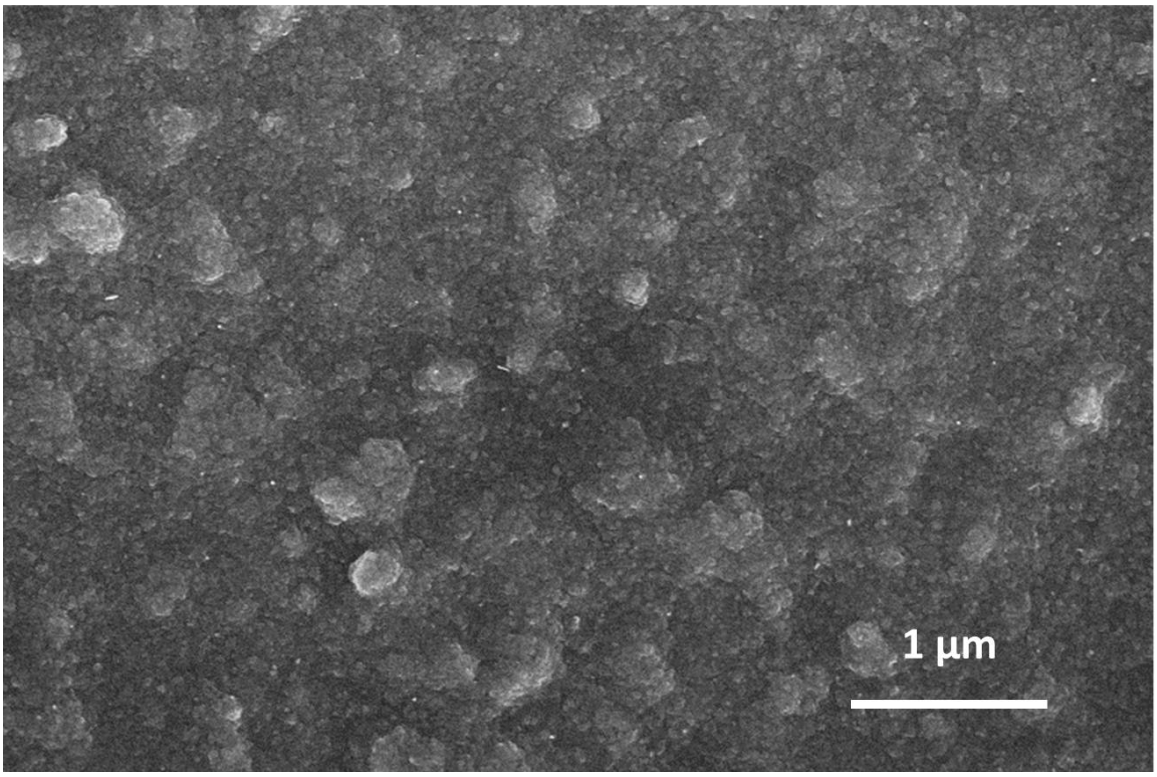

Figure 4.3 Top-view SEM image of thermally oxidized Cu seed layer thermally oxidized at 600 °C for 1 hr under air.

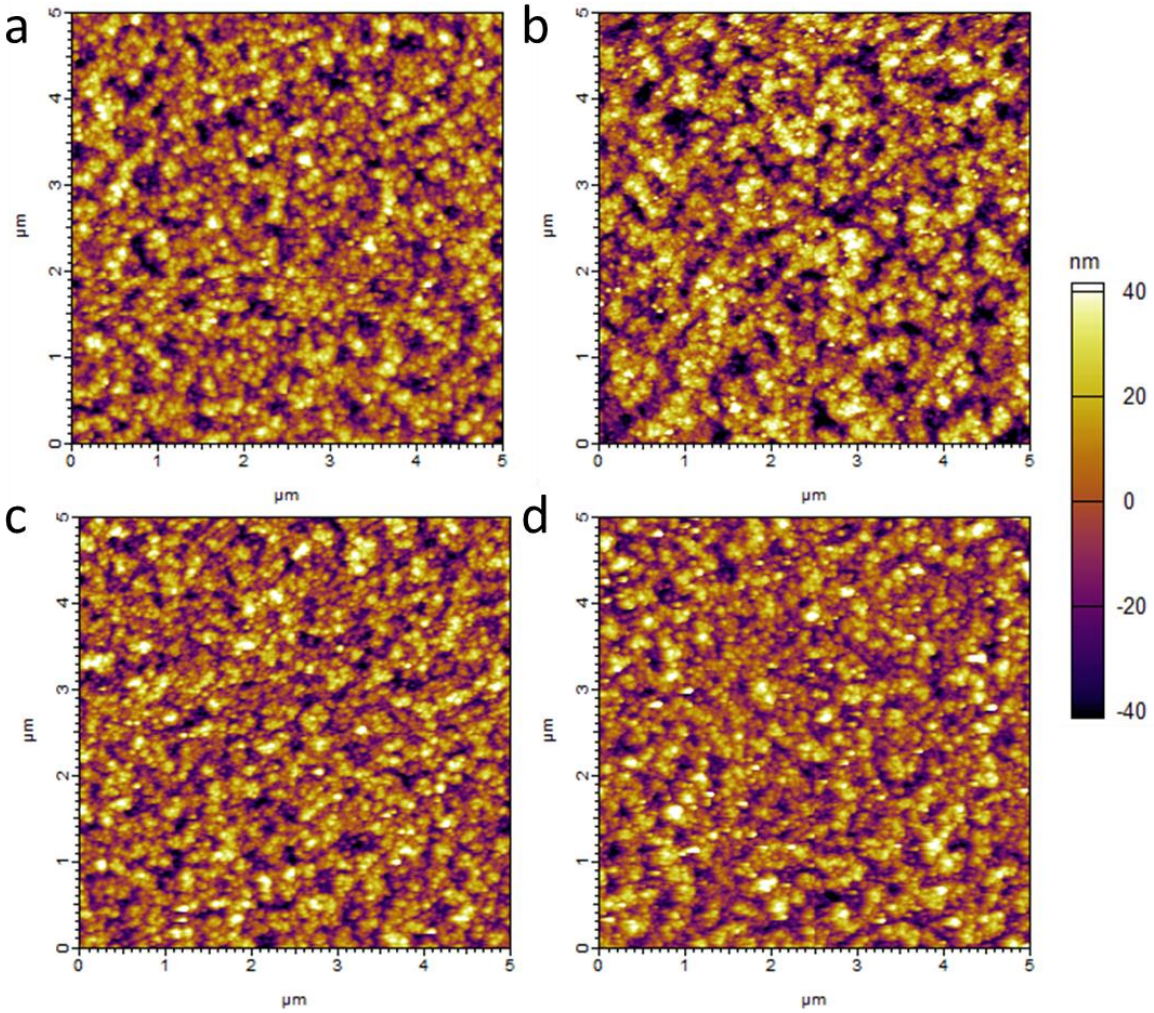

Figure 4.4 AFM 2D images of the samples of a Cu-100, b 200, c 300, and d 500 nm.

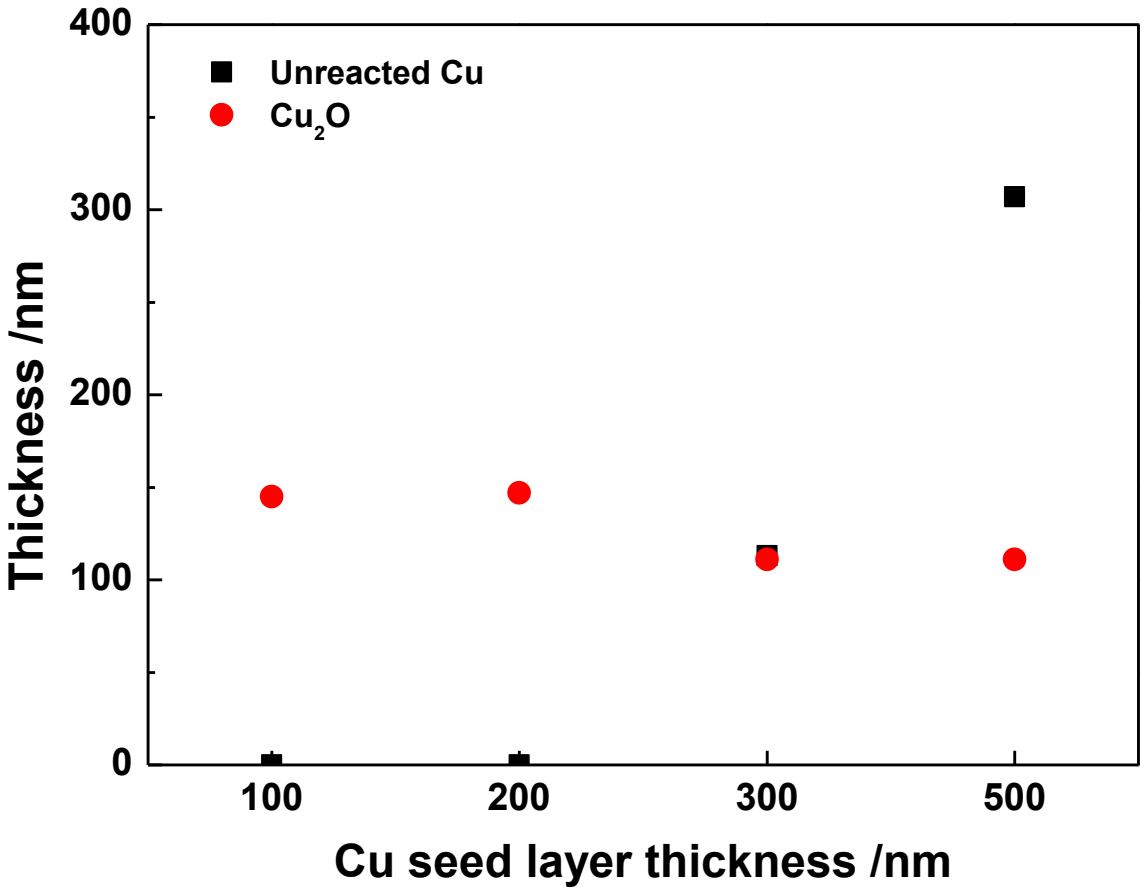

Figure 4.5 Thickness of unreacted Cu and Cu_2O layer for each sample measured by cross-sectional SEM images.

textured Cu_2O is dependent to the starting Cu seed layer thickness as shown in Figure 4.6. Particularly, double layers are observed for samples 2, 3 and 4, whereas a single layer is observable for sample 1. The unreacted layer thickness between the Cu_2O top layer and FTO is 115 and 300 nm in sample 3 and 4, respectively. Through SEM morphology analysis, we conclude that while the synthesized Cu_2O films have different thickness because of the unreacted layer, in all instances textured Cu_2O films possessing similar morphology are synthesized successfully.

The crystallinity of the synthesized samples is analyzed by X-ray diffraction (XRD) characterization from $2\theta = 35°$ to 60°, as shown in Figure 4.7. The peaks for Cu_2O, Cu, and FTO are labelled with their corresponding crystal planes. All samples show the peaks for Cu_2O (111) and (020) crystal planes. On the other hand, sample 2, 3, and 4 show two additional peaks at $2\theta = 43.5°$ and 51.6°, corresponding to the cubic Cu (111) and (200) crystal planes (JCPDS 04-0836). Intensity of the Cu peaks increase with increasing thickness of the unreacted Cu seed layer, while the intensity of the Cu_2O peaks remained unchanged. These results are in support of the observations from cross-sectional SEM analysis. The unreacted layer between Cu_2O and FTO is the Cu layer identified in the XRD results. All the synthesized samples show a textured Cu_2O film with similar crystallinity, irrespective of the unreacted Cu layer thickness between Cu_2O and FTO substrate.

Table 4.2 Measured, calculated and Fitting Parameters from Nyquist, Mott-Schottky, and bode plots from the Cu_2O-100, 200, 300, and 500

	Target Cu seed layer (nm)	Measured Cu_2O (nm)
Sample 1	100	114 ± 28
Sample 2	200	132 ± 33
Sample 3	300	114 ± 21
Sample 4	500	137 ± 41

* Deviation calculated by ImageJ.

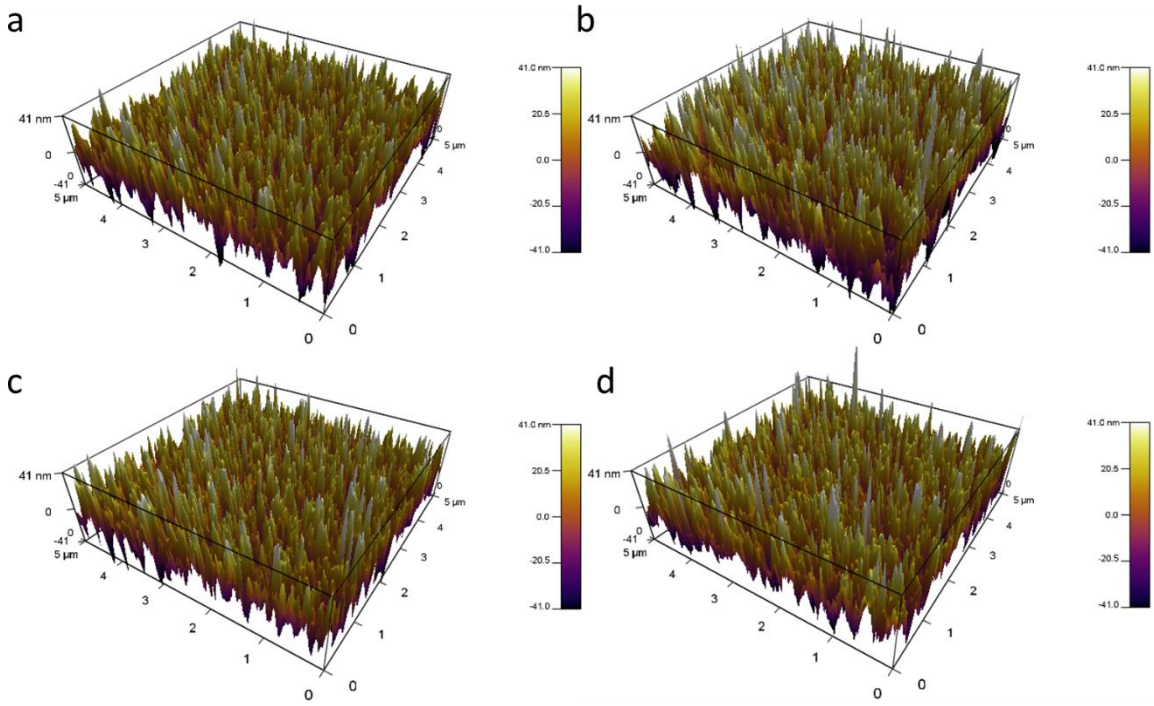

Figure 4.6 AFM 3D images of the samples of a Cu-100, b 200, c 300, and d 500 nm.

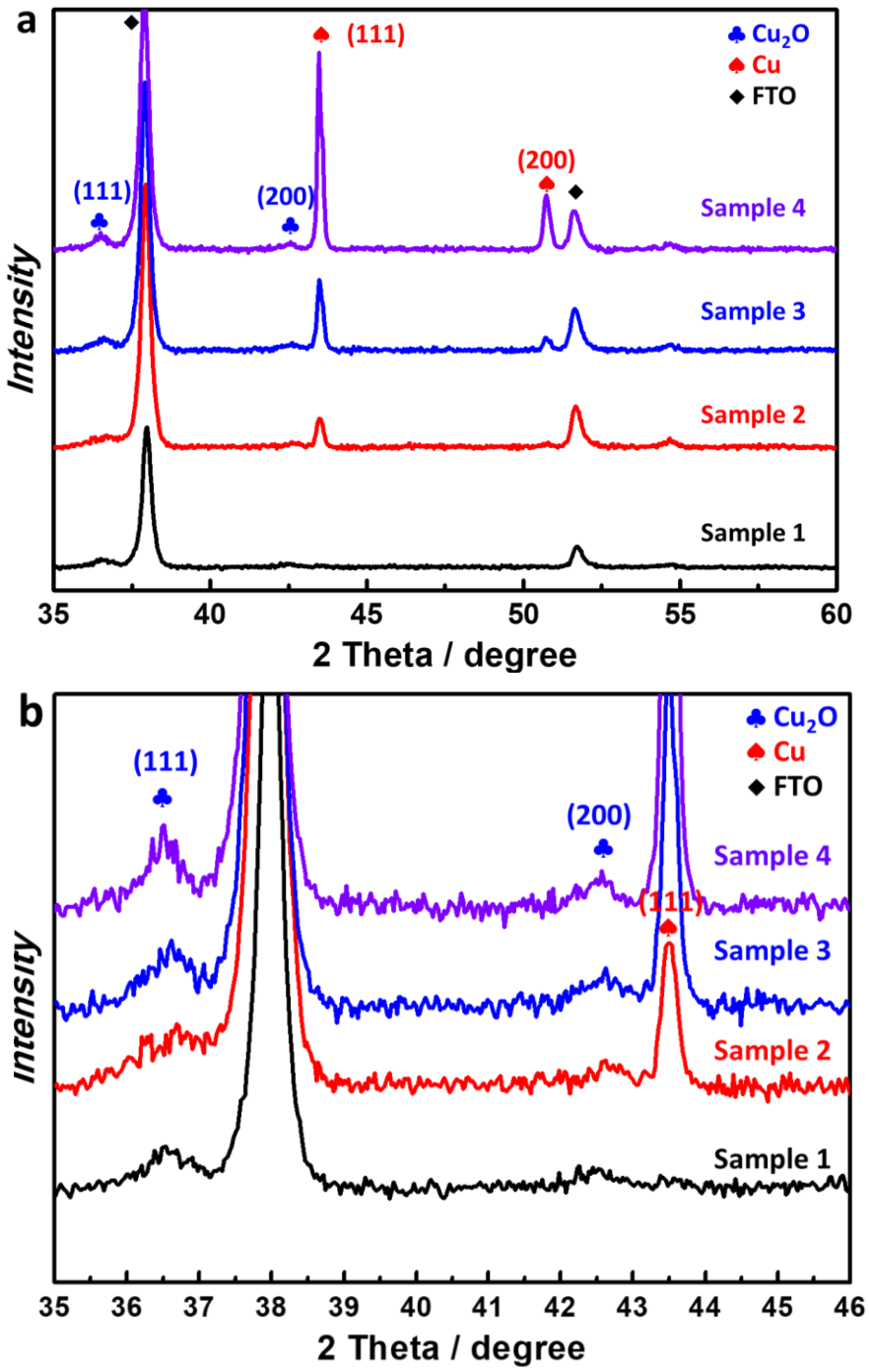

Figure 4.7 Characterization of samples of Cu_2O-100, 200, 300, and 500 nm with and without the unreacted Cu layer. a, X-ray diffraction patterns of Indexes taken from JCPDS: Cu_2O #05-0667, Cu #04-0836, FTO #41-1445. b, normalized absorption spectra in the range of UV/Vis/NIR.

Optical properties of the synthesized samples are analyzed by UV-Vis-NIR spectroscopy. The absorption spectra versus wavelength are shown in Figure 4.8. There are specific absorption peaks at 680 and 640 nm wavelength for sample 1 and 2, respectively. Both are absorption peaks by the Cu_2O layer, verified by the bandgap (1.6 to 2.2 eV) of Cu_2O with an absorption wavelength range from 563 to 775 nm. The obtained bandgap is in the range of reported values in the literature.[16-18] Even though sample 3 and 4 have a Cu_2O layer with similar thickness, the absorption peak by the Cu_2O layer in sample 4 is not noticeable. In sample 3, the absorption peak by Cu_2O can be weakly observed (Figure 4.8 inset). Moreover, sample 4 shows a plateau for the entire range, indicative that the unreacted thick Cu layer with 300 nm prohibits light penetration from the top layer to the FTO substrate. The absorption intensity from unreacted Cu layer increases with thicker unreacted Cu layer thickness as observed in samples 3 and 4. Additionally, sample 2 has a higher absorption peak intensity than sample 1. These results point out to the absorption properties of the Cu_2O/Cu/FTO structure being dominated by the Cu layer thickness, which blocks the incoming light when the seed layer is thicker than 100 nm.

The performance of the textured Cu_2O film as the photocathode in PEC cells is measured. The photocurrent density is measured under illumination to analyze the photocatalytic operation of the photocathode, as shown Figure 4.9. The highest photocurrent density 0.58 mA cm^{-2} at 0 V vs. RHE is achieved from sample 1 photocathode under illumination. On the other hand, both sample 3 and 4 show the lowest photocurrent

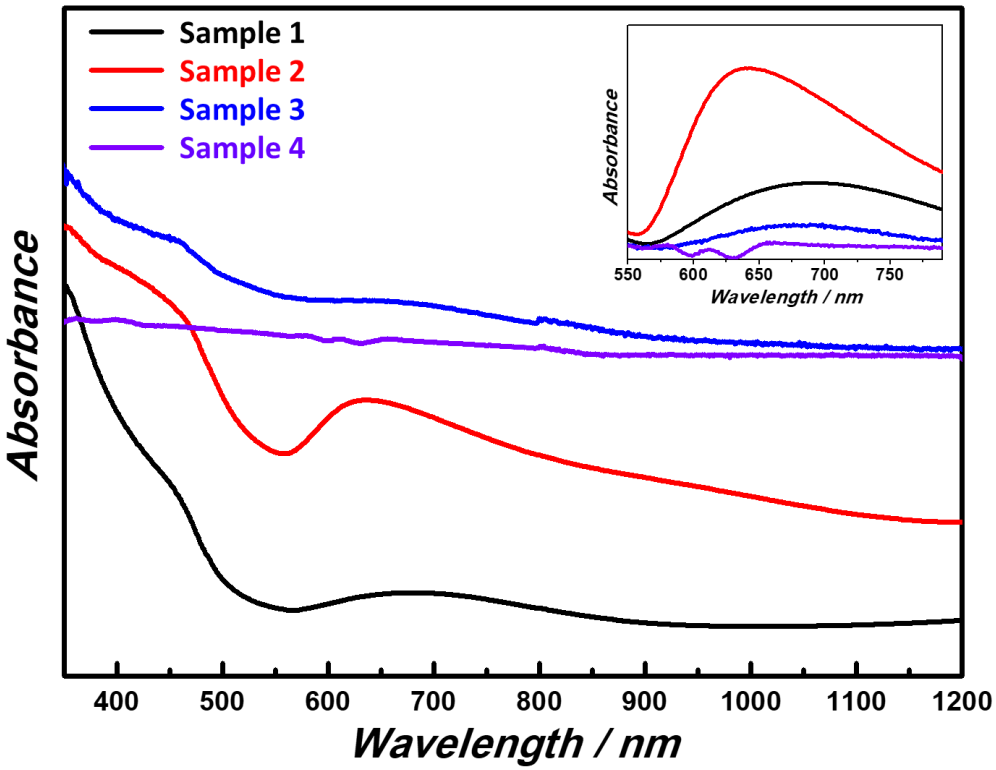

Figure 4.8 The absorption spectra in the range of UV/Vis/NIR of samples with and without the unreacted Cu layer. The inserted spectra shows the absorbance of the samples after subtracting the baseline.

density among the synthesized samples. This is attributed to the unreacted Cu layer (thicker than 100 nm) that reduces photocurrent density. The unreacted Cu layer generated from the Cu_2O layer. Sample 2 shows a reduced performance compared to sample 1 due to a very thin unreacted Cu layer characterized by XRD spectra at $2\theta = 42.7°$, that affects the photocurrent density irrespective of the amount of absorbed light at the Cu_2O layer. In order to enhance the photocurrent density, a textured Cu_2O film without the unreacted Cu layer must be synthesized, as demonstrated by the sample 1.

Electrochemical impedance spectroscopy (ElS) is used to study the interface reaction between the photoelectrode and the electrolyte in the fabricated PEC cells. The EIS measurements are conducted under illumination in a frequency range from 10^5 to 10^{-1} Hz, with an amplitude of 10 mV at an open circuit potential. Nyquist plots for the samples are presented in Figure 4.10. The charge transfer process is expressed as a semicircle in the Nyquist plot. The diameter of the semicircle in a Nyquist plot is equal to the charge transfer resistance (R_{ct}), shown in Table 4.2. The R_{ct} increases with the unreacted Cu layer

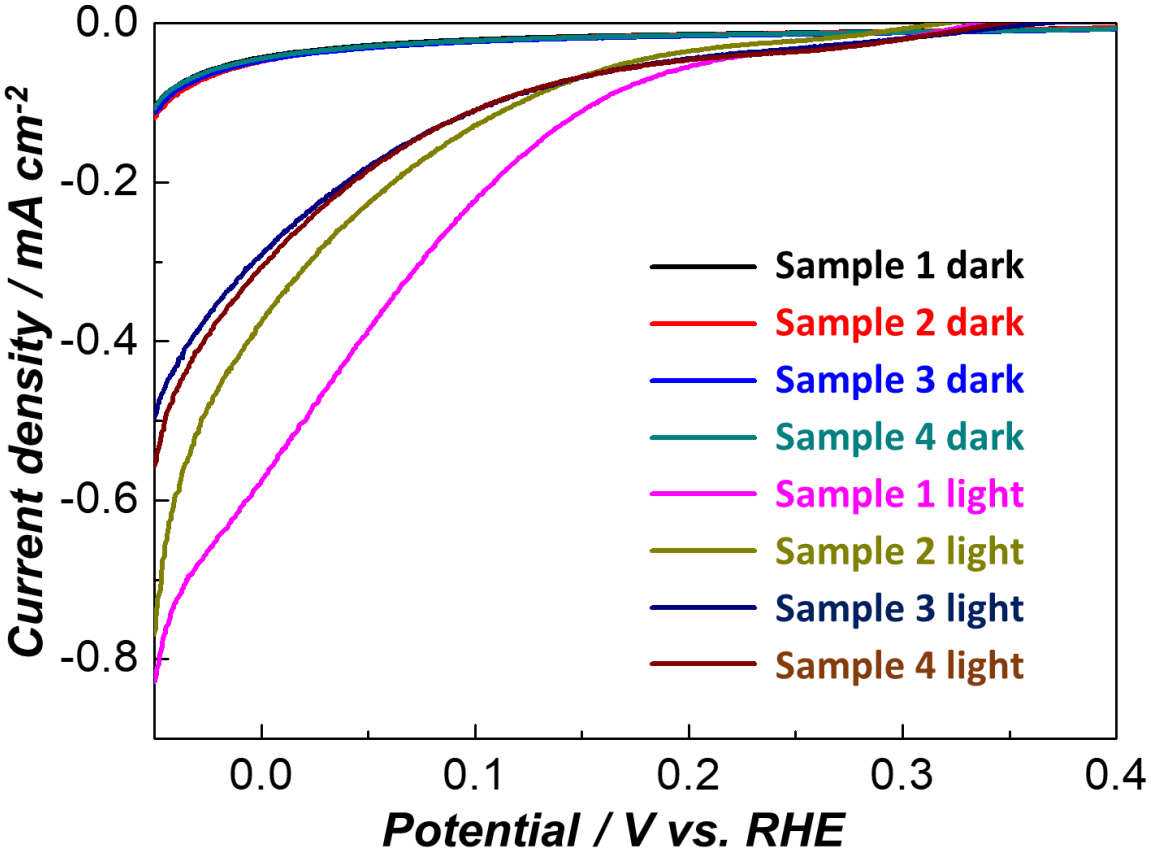

Figure 4.9 Photoelectrochemical performance measurement under dark and illuminated conditions (AM 1.5 G, 100 mW cm^{-2}).

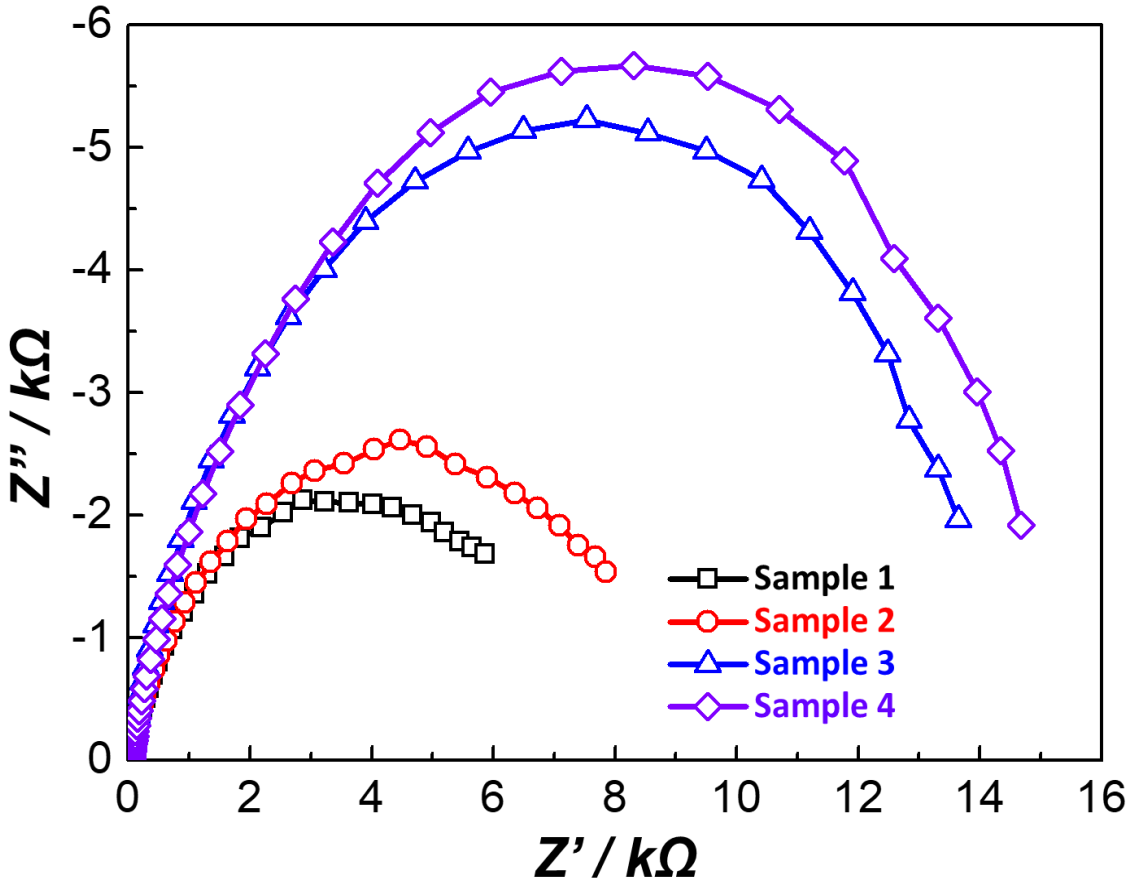

Figure 4.10 Nyquist plots of samples based on photocathodes under illumination (AM 1.5G, 100 mW cm^{-2}, 10 mV open circuit potential, 10^5 to 10^{-1}Hz frequency range, 0.1 M Na_2SO_4).

thickness under illumination. The decrease in electron conductivity is affected by the unreacted Cu layer at the photocathode/FTO interface. Even in the case when the thin acts as a carrier blocking layer between Cu_2O and FTO. Therefore, the unreacted Cu layer negatively impacts the separation and transportation of the electrons and holes

unreacted Cu layer is not distinguishable by cross-sectional SEM analysis it increases the R_{ct}. Sample 3 and 4 with an unreacted Cu layer thicker than 100 nm show two times higher R_{ct} than sample 1 and 2. The results show that the unreacted Cu layer between Cu_2O and FTO reduces the charge transfer process at the interface between Cu_2O surface and electrolyte. This is because the generated carriers cannot be effectively separated and recombine before can be collected.

The capacitance on the photoelectrode/electrolyte are measured in order to calculate the flatband potential (V_{fb}) and carrier density (N_A), shown in Figure 6. Parameters are calculated from $1/C^2$ vs. applied potential plot (Mott-Schottky plot) at a fixed frequency of 10^3 Hz. The measured $1/C^2$ is expressed in the equation (1) below:

$$\frac{1}{C^2} = \frac{2}{N_A e \varepsilon \varepsilon_0}\left[\left(V_S - V_{fb}\right)\right]\frac{kT}{e}$$

Table 4.3 The charge transfer resistance (R_{ct}), carrier density (N_A), flatband potential (V_{fb}), and carrier lifetime (τ) measured and calculated from the fitting parameters from Nyquist, Mott-Schottky, and Bode plots from the samples.

	Cu_2O-100	Cu_2O-200	Cu_2O-300	Cu_2O-500
R_{ct} (Ω)	7.7×10^3	8.9×10^3	14.5×10^3	15.9×10^3
N_A (cm^{-3})	2.74×10^{15}	3.04×10^{15}	2.17×10^{15}	2.97×10^{15}
V_{FB} (V)	0.492	0.486	0.496	0.486
τ (ms)	13.4	2.9	3.3	3.5

N_A, e, ε_0, ε, k, T and V_S are the hole density, the elementary charge, the permittivity of the vacuum, the relative permittivity of photocathode (Cu_2O is 10.26), the Boltzmann constant, temperature, and the applied potential, respectively.[1,15] Based on this equation, the hole density in the Cu_2O layer can be calculated from the slope of the curve. The carrier density of the samples ranges from 2.17 x 10^{15} to 3.04 x 10^{15} cm^{-3}, shown in Table 4.2. The tangential point from the extrapolated linear part of the curve is the V_{fb} of the photocathode. The negative slope of the linear part in the curve shows p-type semiconductor behavior. The V_{fb} is 0.486 to 0.496 V vs. RHE. These results indicate that the unreacted Cu layer does not affect the carrier density and the V_{fb}.

Moreover, the Bode plot displaying the phase as the response against the frequencies endow the information of the carrier transport/recombination process in the semiconductor (Figure 4.11). The Bode plot determines the information of carrier lifetime (τ) inside the PEC under illumination. Measured frequencies at the maximum phase were used to calculate the carrier lifetime $\boldsymbol{\tau = 1/2\pi f_{max}}$.[31-33] The hole lifetime decreases significantly with the existence of the unreacted Cu layer. Longer carrier lifetime (13.5 ms) is obtained in sample 1. The three samples with an unreacted Cu layer show shorter carrier lifetime ranging from 2.9 to 3.5 ms. The PEC cell using sample 1 achieved the best efficiency among the samples due to the longer carrier lifetime that leads to a slow recombination rate. The Cu_2O film without the unreacted Cu layer improve

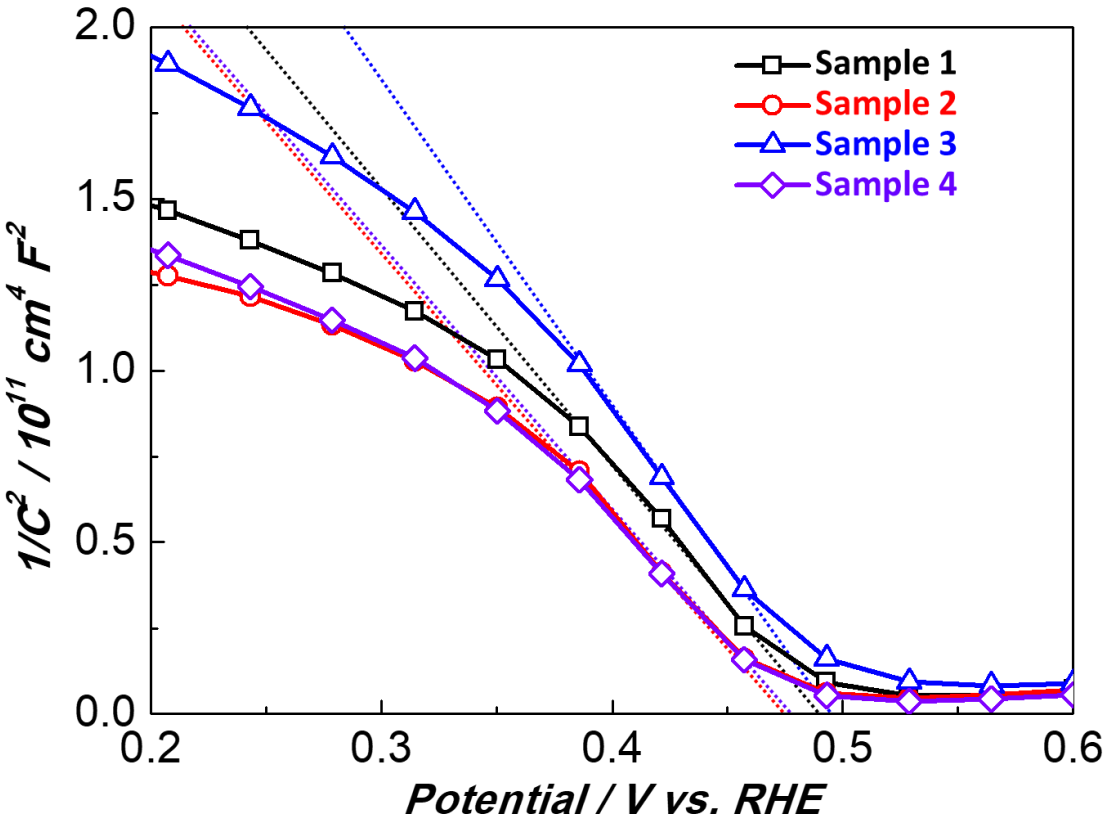

Figure 4.11 Mott-Schottky plots of samples (10^3 Hz frequency, 0.1 M Na_2SO_4).

the carrier lifetime while its carrier density and V_{fb} are not affected (Figure 4.12). From our analysis, we conclude that the enhanced photocurrent density using Cu_2O is attributed to the longer carrier lifetime.

4.4 Conclusions

Cu_2O photocathodes with fully reacted Cu layer have been developed via a solution based process. These samples show superior electrochemical properties in PEC cells compared to samples with an unreacted Cu layer. A 100% enhancement in photocurrent density under sunlight illumination for a water splitting application is measured. We confirmed that the enhancement is attributed to the improvement in the charge transfer rate and carrier lifetime. Therefore, the sample with fully reacted Cu layer presents low charge transfer resistance at the interface between the Cu_2O surface and electrolyte.

References

[1] Z. Zhang, P. Wang, *J. Mater. Chem.*, **22**, 2456-2464 (2012).

[2] A. Choudhury, H. Chandra, A. Arora, *Renew. Sust. Energ. Rev.*, **20**, 430-442 (2013).

[3] A. Qi, B. Peppley, K. Karan, *Fuel Process. Technol.*, **88**, 3-22 (2007).

[4] D. Kim, K. K. Sakimoto, D. Hong, P. Yang, *Angew. Chem. Int. Edit.*, **54**, 3259-3266 (2015).

[5] F. E. Osterloh, *Chem. Soc. Rev.*, **42**, 2294-2320 (2013).

[6] I. S. Cho, C. H. Lee, Y. Feng, M. Logar, P. M. Rao, L. Cai, D. R. Kim, R. Sinclair, X. Zheng, *Nat. Commun.*, **4**, 1723 (2013).

[7] X. Wang, R. Long, D. Liu, D. Yang, C. Wang, Y. Xiong, *Nano Energy*, **24**, 87-93 (2016).

[8] Q. Wang, T. Hisatomi, Q. Jia, H. Tokudome, M. Zhong, C. Wang, Z. Pan, T. Takata, M. Nakabayashi, N. Shibata, *Nat. Mater.*, **15**, 611-615 (2016).

[9] O. Khaselev, J. A. Turner, *Science*, **280**, 425-427 (1998).

[10] A. Paracchino, N. Mathews, T. Hisatomi, M. Stefik, S. D. Tilley, M. Grätzel, *Energ. Environ. Sci.*, **5**, 8673-8681 (2012).

[11] Y.-K. Hsu, C.-H. Yu, Y.-C. Chen, Y.-G. Lin, *Electrochim. Acta*, **105**, 62-68 (2013).

[12] T. Minami, T. Miyata, Y. Nishi, *Sol. Energy*, **105**, 206-217 (2014).

[13] D. Chen, Z. Liu, Z. Guo, W. Yan, Y. Xin, *J. Mater. Chem. A.*, **6**, 20393-20401 (2018).

[14] A. A. Dubale, C.-J. Pan, A. G. Tamirat, H.-M. Chen, W.-N. Su, C.-H. Chen, J. Rick, D. W. Ayele, B. A. Aragaw, J.-F. Lee, *J. Mater. Chem. A*, **3**, 12482-12499 (2015).

[15] J. Luo, L. Steier, M.-K. Son, M. Schreier, M. T. Mayer, M. Grätzel, *Nano Lett.*, **16**, 1848-1857 (2016).

[16] A. Kargar, S. S. Partokia, M. T. Niu, P. Allameh, M. Yang, S. May, J. S. Cheung, K. Sun, K. Xu, D. Wang, *Nanotechnology*, **25**, 205401 (2014).

[17] A. A. Dubale, A. G. Tamirat, H.-M. Chen, T. A. Berhe, C.-J. Pan, W.-N. Su, B.-J. Hwang, *J. Mater. Chem. A*, **4**, 2205-2216 (2016).

[18] S. Jamali, A. Moshaii, *Appl. Surf. Sci.*, **419**, 269-276 (2017).

[19] K. L. Sowers, A. Fillinger, *J. Electrochem. Soc.*, **156**, F80-F85 (2009).

[20] Y. Yang, D. Xu, Q. Wu, P. Diao, *Sci. Rep.-UK,* **6**, 35158 (2016).

[21] A. Paracchino, V. Laporte, K. Sivula, M. Grätzel, E. Thimsen, *Nat. Mater.*, **10**, 456-461 (2011).

[22] C. J. Engel. T. A. Polson, J. R. Spado, J. M. Bell, A. Fillinger, *J. Electrochem. Soc.,* **155**, F37-F42 (2008).

[23] A. Paracchino, J. C. Brauer, J.-E. Moser, E. Thimsen, M. Grätzel, *J. Phys. Chem. C,* **116**, 7341-7350 (2012).

[24] K. P. Musselman, A. Marin, L. Schmidt-Mende, J. L. MacManus-Driscoll, *Adv. Funct. Mater.*, **22**, 2202-2208 (2012).

[25] L. Zhang, D. Jing, L. Guo, X. Yao, *ACS Sustain. Chem. Eng.*, **2**, 1446-1452 (2014).

[26] T. Minami, Y. Nishi, T. Miyata, *Appl. Phys. Express*, **6**, 044101 (2013).

[27] Z. Zhang, R. Dua, L. Zhang, H. Zhu, H. Zhang, P. Wang, *ACS Nano*, **7**, 1709-1717 (2013).

[28] C. G. Morales-Guio, S. D. Tilley, H. Vrubel, M. Grätzel, X. Hu, *Nat. Commun.*, **5**, 3059 (2014).

[29] K.-S. Choi, *J. Phys. Chem. Lett.*, **1**, 2244-2250 (2012).

[30] Y. Qu, J. Qian, J. Liu, L. Yao, L. Zhao, X. Song, P. Zhang, L. Gao, *J. Electrochem. Soc.*, **166**, H452-H458 (2019).

[31] K.-M. Lee, C.-W. Hu, H.-W. Chen, K.-C. Ho, *Sol. Energ. Mat. Sol. C.*, **92**, 1628-1633 (2008).

[32] H. Shelke, A. Lokhande, A. Patil, J. Kim, C. Lokhande, *Surf. Interfaces*, **9**, 238-244 (2017).

[33] S. S. Patil, N. L. Tarwal, H. M. Yadav, S. D. Korade, T. S. Bhat, A. M. Teli, M. M. Karanjkar, J. H. Kim, P. S. Patil, *J. Solid State Electr.*, **22**, 3015-3024 (2018).

Chapter 5

CuO Crystal and Morphology Engineering for Improved Hydrogen Generation and Stability by Faster Kinetic Reaction Rate

5.1 Introduction

Artificial photosynthesis from single photoelectrode integrates solar energy collection and water electrolysis, which makes it a promising technology for dealing with the increasing population and energy demand.[1] One of the methods to deal with this energy crisis is to utilize alternative energy sources, such as generating hydrogen fuel through water splitting.[2,3] Semiconductor materials are promising candidates for photoelectrochemical (PEC) water splitting cells.[4,5] PEC cells are sunlight-driven by the photon producing excitons at the interface between the semiconductor and electrolyte junction.[6,7] The overall performance of semiconductor is dependent on the light absorption efficiency, exciton separation at the interface between the semiconductor and the electrolyte, the major carrier transport in semiconductor layer, and the minor carrier transfer to electrolyte.[8,9] For n- and p-type semiconductors, the junction between semiconductor/electrolyte leads the transfer of minority carriers (hole and electron) which reacts with OH^- and H^+ to generate oxygen and hydrogen, respectively.[10-12] The photoexcited exciton can be driven to separation by an electric field formed at the junction between semiconductor/electrolyte. To operate PEC water splitting by using only sunlight, the development of both types of semiconductor materials as a photocathode and photoanode is essential.[13-15] There is a large number of researchers that are focusing on

the investigation of n-type semiconductors as a photoanode in PEC water splitting devices.[16-21] In these devices, the minority hole transfers to the electrolyte and is driven by an electric field which results in oxygen evolution, and the majority electron transports to the counter electrode via an external circuit for hydrogen evolution.[22] However, p-type semiconductors that are used as photocathodes for PEC water splitting devices have issues with the photo-induced the self-reduction of itself.[23] Due to this, there are few studies of p-type semiconductors used as photocathodes reported.[24-26] One of the most favorable candidates for photocathodes in PEC devices is cupric oxide (CuO).[27-29] It is non-toxic, earth abundant, and a p-type semiconductor with a direct band gap of 1.2 -1.6 eV and has a high optical absorption exceeding 1.04 x 10^4 cm^{-1} at 800 nm.[30,31] These favorable qualities have led to a rapid investigation into CuO as a possible material for photocatalysis. Several research groups have explored utilizing CuO as a photocathode for sunlight-driven hydrogen evolution from water.[27-29] Despite the efforts of engineering the morphology,[32] forming heterojunction,[33] and optimizing the oxygen to copper ratio in CuO,[34] the reported photocurrent density and stability is still low compared to other photoanode materials.[32] This limitation of CuO as a photocathode is caused by the poor charge separation at the electrolyte surface, transfer to the electrolyte, and transportation in the bulk.[35]

In this work, we use Zn material as a dopant in the CuO crystal structure. Zn-doped CuO (Zn:CuO) is synthesized on a conductive transparent substrate through facile electrodeposition. Zn:CuO exhibits an obvious increase in photocurrent density and stability under illumination. The optimized Zn:CuO shows a photocurrent of -1.7 mA cm^{-}

^{2}, which is better than that of the CuO photocurrent of -0.86 mA cm^{-2} at 0 V vs. RHE. This is one of the highest photocurrent densities recorded for a CuO photocathode. The crystallographic orientation, surface exposed facets, and morphology of Zn doped CuO are determined to be the leading factors causing the improvement of the photocurrent density and stability. The modified surface facets and area inhibit the charge accumulation at the interface of the photocathode and electrolyte, leading to a significant improvement in stability. This enlargement in surface area of the Zn:CuO leads to an increased amount of reaction sites on the surface.

5.2 Experimental procedure

All samples are prepared on a FTO coated-glass substrate (surface resistivity ~13 Ω/sq, Sigma-Aldrich). The FTO substrates are cleaned using a detergent solution in deionized (DI) water (18.2 MΩ), acetone, and isopropyl alcohol (IPA) in an ultrasonication bath for 5 min for each step. A nitrogen gun is used to dry the residue IPA on the surface of the FTO substrates. The precursor solution for the electrodeposition process is prepared as follows. 3 M of $CH_3CH(OH)COOH$ (lactic acid, from Sigma-Aldrich) and 0.4 M of $CuSO_4$ (Copper sulfate, from Alfa Aesar) is mixed into 30 ml DI water. After all the components are combined, the solution is mixed using a magnetic stir bar. 20 M of NaOH aqueous solution is added to obtain 11 pH of the prepared solution. $Zn(NO_3)_2 \cdot 6H_2O$ (zinc nitrate hexahydrate, from Sigma-Aldrich) is used as a dopant precursor and is added into the prepared solution. The amount of zinc nitrate in this work is 1, 3, 5, and 8% concentration. Zn-doped CuO films are deposited onto the cleaned FTO substrates by electrodeposition at 60 C^{o}. The electrodeposition is performed in a lactate-stabilized copper

sulfate aqueous solution (pH 11) applying a constant current density -1.2 V using chronoamperometry mode, with a platinum wire counter electrode. CuO is electrodeposically grown on FTO substrates and is annealed at 600 C^o for 2 hours under air.

The morphologies of the synthesized films are characterized using scanning electron microscopy (FEI NovaNanoSEM450). X-ray diffraction (XRD) spectra are obtained with PANanalytical X'Pert X-ray diffractometer, using Cu Kα diffraction (1.540598 Å). Spectra are scanned from $2\theta = 20° - 80°$ at a scan rate of $4° \text{ min}^{-1}$. The optical properties of the synthesized films are measured by the diffuse reflectance spectra from front side illumination with a Varian Cary 500 UV-Vis-NIR spectrophotometer. X-ray photoelectron spectroscopy (XPS) characterization was carried out by using a Kratos AXIS ULTRA^{DLD} XPS system equipped with an Al Kα monochromated X-ray source and a 165 mm mean radius electron energy hemispherical analyzer. Vacuum pressure was kept below 3×10^{-9} torr during the acquisition.

All electrochemical experiments are carried out in a standard three-electrode system, consisting of the working electrode, Pt wire as the counter electrode, and the reference electrode of Ag/AgCl/KCl. All data is obtained by a potentiostat (VersaSTAT 4, AMETEK). Photoelectrochemical performance of the synthesized CuO and Zn:CuO photocathodes are measured in 0.1 M $NaSO_4$ aqueous solution under light illumination (AM 1.5 G, 100 mW cm^{-2}) by solar simulator (Oriel Sol343A Class AAA Solar Simulator, 450 W Xenon). The solar simulator is calibrated by a monoclinic silicon solar cell (Newport, Oriel® Reference Solar Cell & Meter, 91150V). The scan rate for the linear

sweep voltammetry is 50 mV/s and the applied potential is 0 to +0.6 V vs. RHE. Electrochemical impedance spectroscopy (EIS) is conducted at +0.1 V vs. RHE from 10^5 to 10^{-1} Hz frequency under illumination to study interfacial charge transfer between the photocathode and the electrolyte. Measuring the capacitance against potential at 10^3 Hz frequency is performed under dark from +0.2 to +0.6 V vs. RHE to characterize the flat band potential. The stability of the CuO and Zn:CuO is measured at 0 V vs. RHE under chopped irradiation using the light source described above. Applied potential used for photoelectrochemical measurement is converted into the reversible hydrogen electrode (RHE) using the equation: $V_{RHE} = V_{Ag/AgCl/KCl} + 0.235\ V + 0.059\ pH$.

5.3 Results and discussion

SEM images present the morphologies and thickness of CuO and Zn:CuO (5 at%) shown in Figure 1. The crystal size of the synthesized Zn:CuO film decreases and the thickness increases compared to the CuO film as shown in Figure 5.1. Top and cross-sectional structure of CuO with different doping concentrations (1, 3, and 8%) are shown in Figure 5.2. Average particle sizes and thickness measured from the SEM images using ImageJ software are shown in Figure 5.3. The cross-sectional SEM images shown in Figure 5.1 (b) and (d) clearly indicate the discrepancies of the particle sizes that CuO with Zn dopant has smaller particles size than CuO. The particle size decreases with increasing concentration of Zn dopant. The voids in the synthesized films can be inferred using the materials thickness from cross-sectional SEM images. During the electrodeposition process, the reaction for the samples is completed when the charge reaches to -1 C cm^{-2} to form the CuO_x compound on the surface of FTO working electrode. It is certain that same

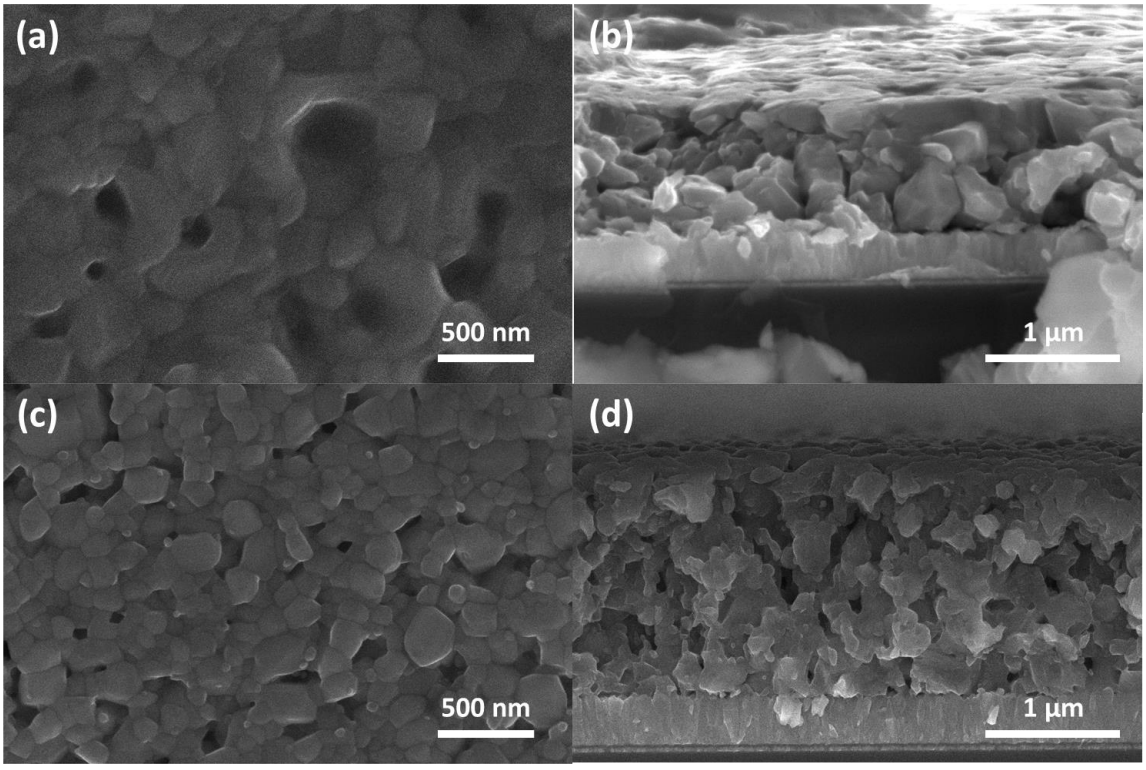

Figure 5.1 SEM images of top view; (a) CuO, (c) Zn:CuO and cross-sectional view; (b) CuO, (d) Zn:CuO.

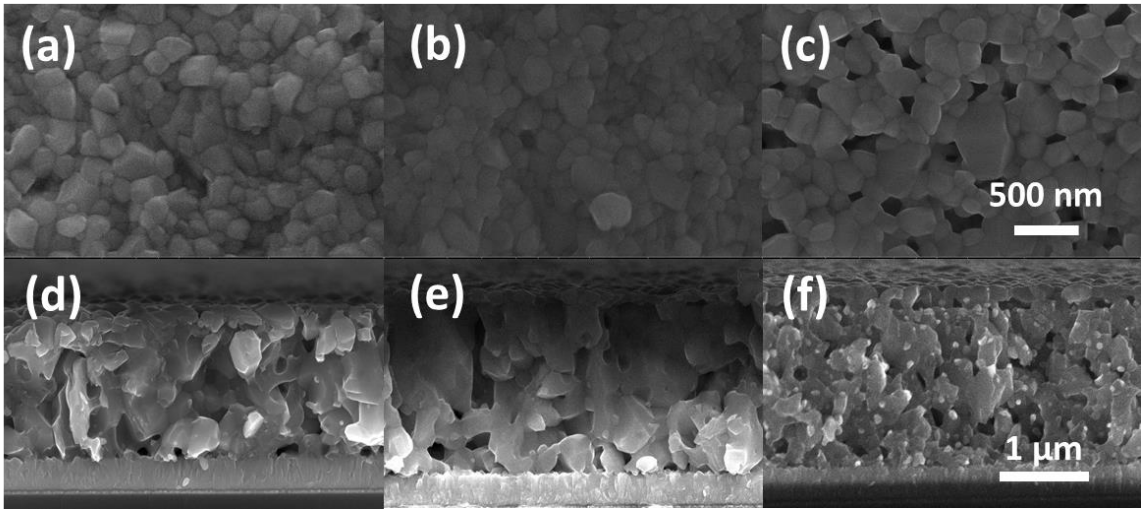

Figure 5.2 Top view (a) to (c) and cross-sectional (d) to (f) SEM images with concentration of Zn dopant 1, 3, and 8 at%.

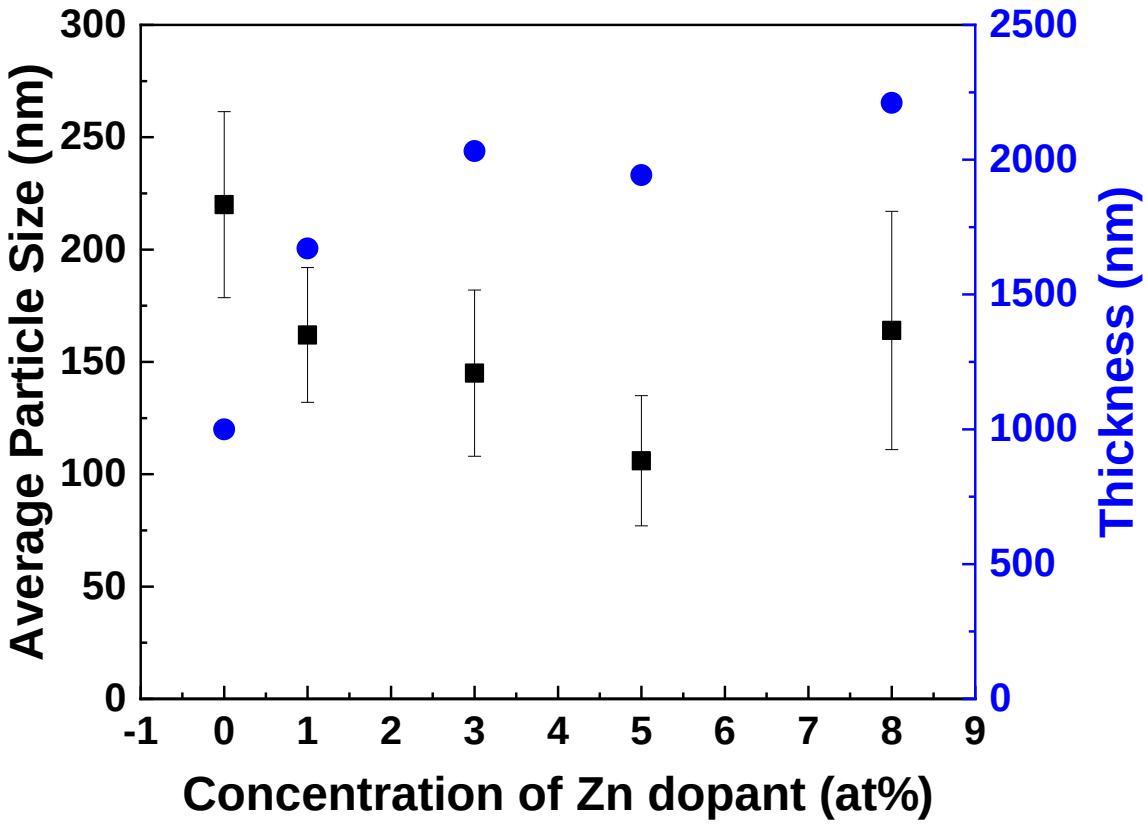

Figure 5.3 Average particle sizes and thickness of the CuO and Zn:CuO.

amount of the material is deposited on the FTO substrate regardless of the concentration of the Zn dopant in the electrodeposition solution. However, the thickness of the film on the FTO substrate increases from 1 to 1.9 μm depending on the concentration of the Zn dopant. The top view and the cross-sectional SEM images clearly show that the film synthesized without the Zn dopant is more packed while the film with the Zn dopant is less packed and consists of more voids inside the film. Therefore, the density of the synthesized materials decreases and its total volume and voids consisting of the CuO_x compound increase when the Zn dopant is added into the electrodeposition solution. The Zn dopant affects the crystal growth condition of the CuO_x compound resulting in an incremental amount of void and a reduction of particle size. Zn:CuO has a larger surface area which can act as photoelectrochemical reaction site and its smaller particle size leads to a shorter photoexcited charge transfer length to the electrolyte compared to CuO.

These experiments show that an existence and the concentration of Zn dopant have an effect on the crystallographic orientation, as measured by XRD shown in Figure 5.4. Due to an anisotropy from the different growth rates in monoclinic CuO crystal, it has the predominant crystallographic orientation.[36] The CuO films are prepared using an electrodeposition method based on the reaction solution including various Zn dopant concentrations from 0 to 8%. The crystallinity of the synthesized samples is examined by XRD which is scanned from 20° to 80° as shown in Figure 5.4. To analyze the peak position shift, the peaks of the spectra are analyzed in detail from 35° to 36.0° as shown in Figure 5.5. The XRD spectra for the samples match the standard CuO (JCPDS, #45-0937), ZnO

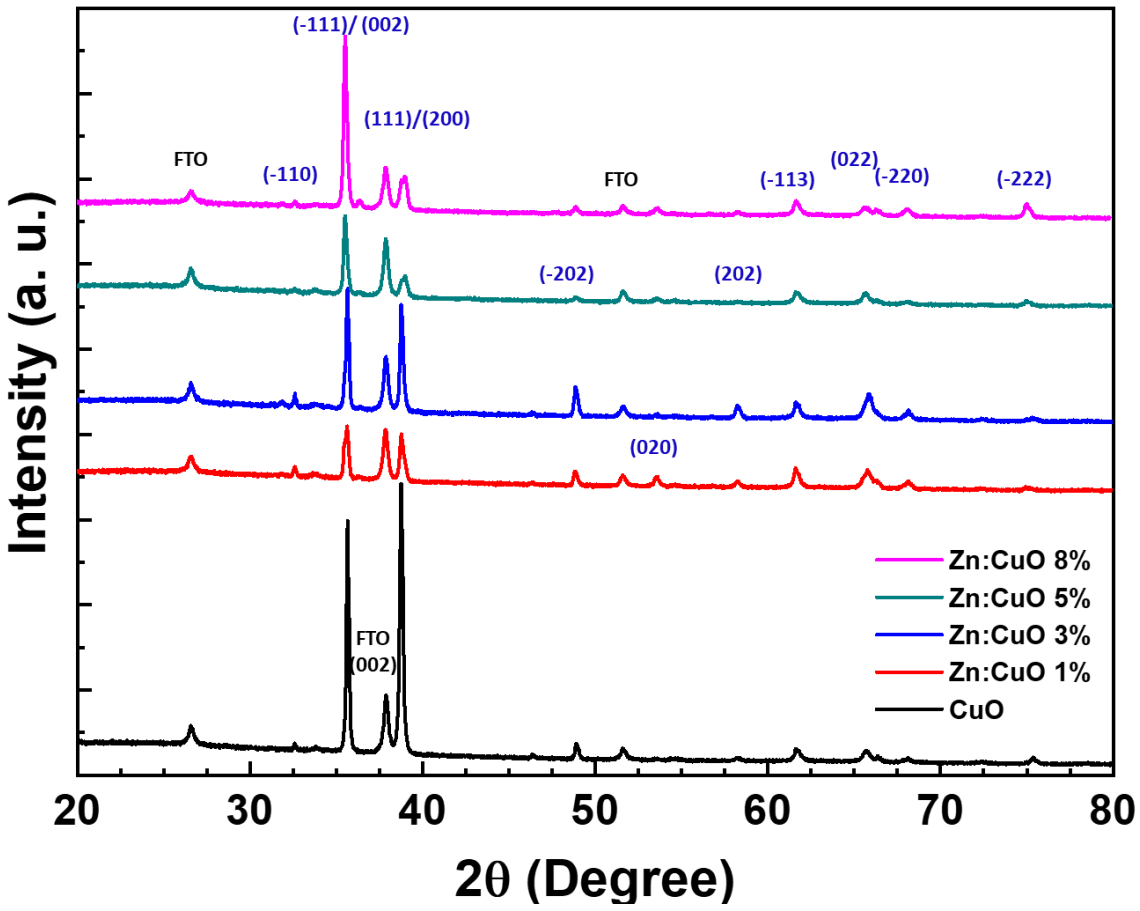

Figure 5.4 XRD spectra of CuO and Zn:CuO from 20 to 80°.

(JCPDS, #36-1451), and FTO spectra (JCPDS, #77-0447), thus confirming the successful crystallization of the monoclinic CuO phase. For the CuO monoclinic crystal, two peaks are observed at 35.7° and 38.8° which correspond with ($\bar{1}$11) and (111) crystal planes. There are discrepancies of the crystal plane between CuO and Zn:CuO in which the peak position at highest intensity shifts to the lower degree. The intensity of ($\bar{1}$11) and (111) peaks decrease when the Zn dopant is introduced to the electrodeposition solution and the shoulder peaks at the (002) and (200) increase as well. The ($\bar{1}$11) and (111) peaks found at CuO film without Zn dopant disappear after 3 at% concentration of Zn dopant in the electrodeposition solution. The shoulder peaks become the predominant crystal orientation at 5 and 8 at%. In addition, Zn:CuO films with 8 at% have the peak of a wurtzite ZnO (101) crystal plane at 36.4° which matches the standard ZnO spectra as shown in Figure 5.6. Nanoparticles with hexagonal surface shape on the CuO surface from the SEM images shown in Figure 5.1 (d) and 5.2 (f) are determined as a ZnO crystals. From these results, the existence of Zn dopant and its concentration in the deposition solution effect the growth condition of the CuO film. When Zn dopant is added into the electrodeposition solution, the dominant crystallographic orientation is changed from ($\bar{1}$11) and (111) to (200) and (002), respectively. It is well known that the crystal orientation determines the grain size due to the differing reaction kinetic rates.[36]

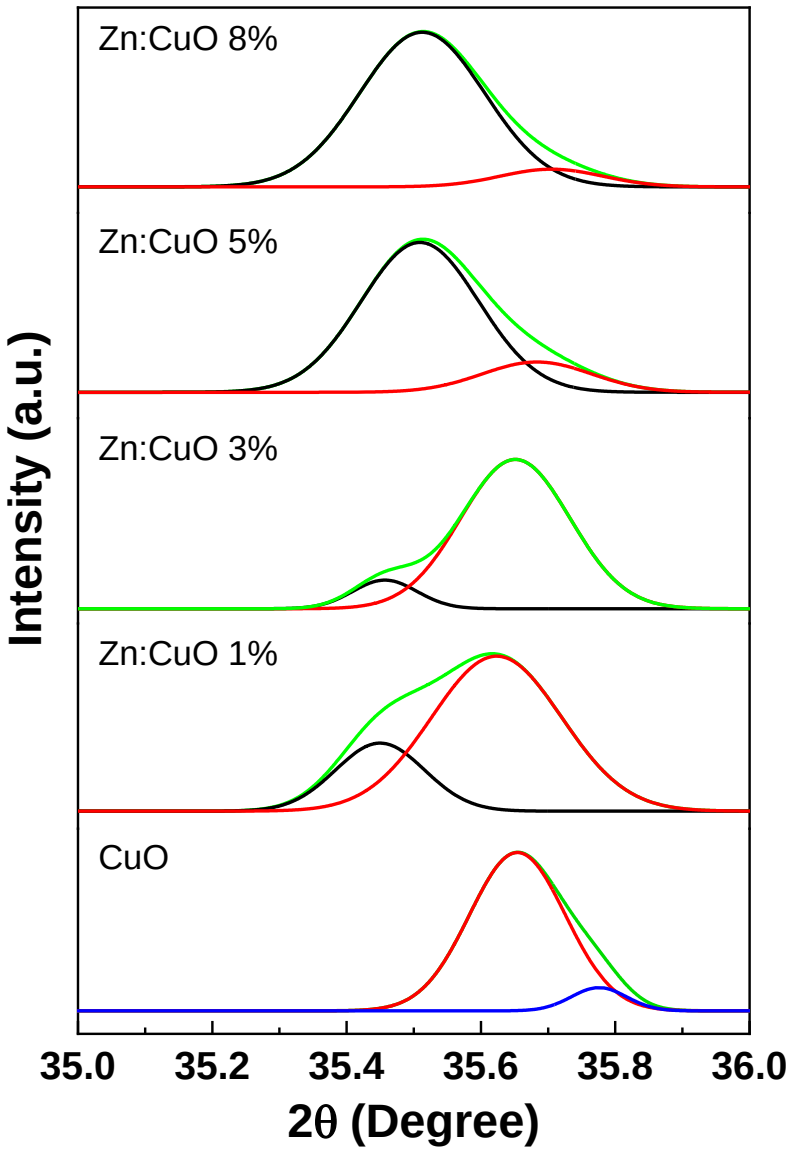

Figure 5.5 X-ray diffraction spectra of the CuO and Zn:CuO.

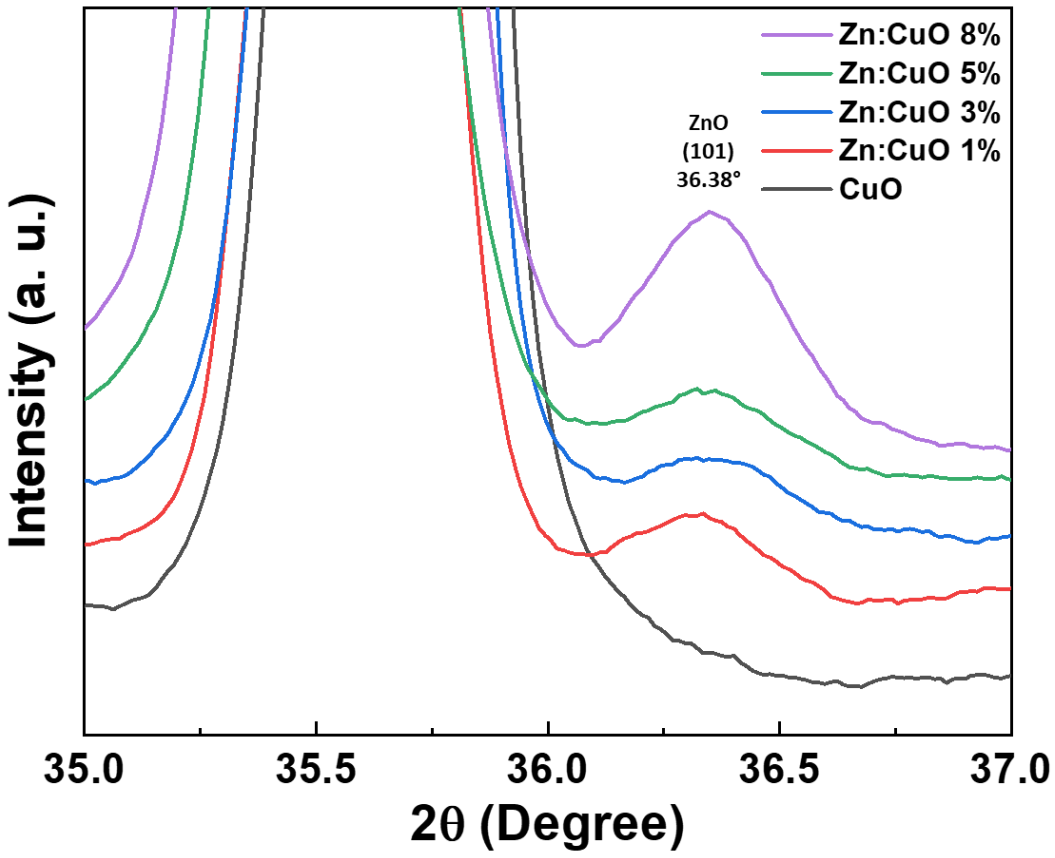

Figure 5.6 X-ray diffraction spectra of CuO and Zn:CuO from 35 to 37°.

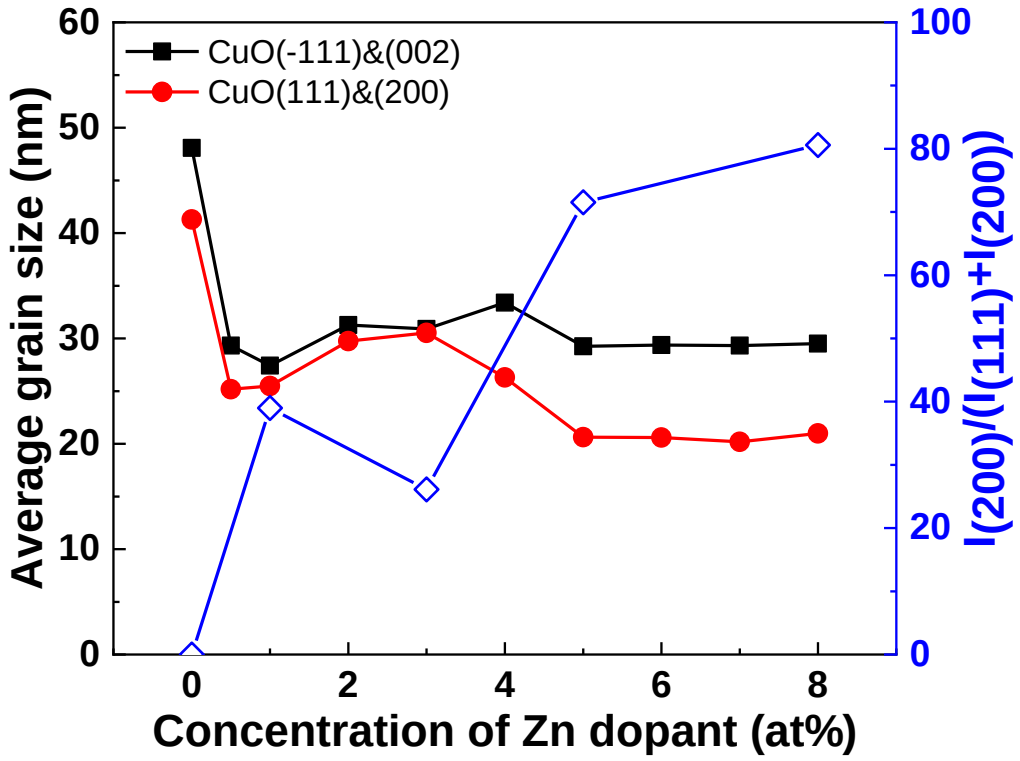

Figure 5.7 Average grain size depending on the concentration of Zn dopant (at%).

Average grain sizes for the predominant crystal orientation is calculated by Scherrer equation using the full width at the half maximum and the peak position measured from XRD results as shown in Figure 5.7. For a given deposition condition, if one compares the grain size of the CuO deposited by electrodeposition with and without Zn dopant, the smaller grain size is obtained at the higher concentration of Zn dopant. This is because the Zn dopant engineers the crystal orientation and growth rate of CuO. There is no significant change in the average grain size due to the concentration, which may affect the growth conditions of CuO if it is saturated above 5 at%, introducing the ZnO nanocrystal on the CuO surface. These results show that an excess amount of Zn dopant does not participate in CuO crystal growth reaction, but instead it forms a new ZnO crystal on the CuO surface. Therefore, concentrations higher than 5 at% of Zn dopant do not make any changes to the grain size. The relative small grain size of Zn:CuO has a larger surface area compared to CuO, this leads to a more active surface for photoelectrochemical reactions. The crystallographic orientation is associated with the charge transfer to the electrolyte. The monoclinic CuO with the strong (200) and (002) orientation reacts with H^+ in water, while the strong ($\bar{1}11$) and (111) orientation have less amount of reactivity. The crystal plane at the surface of CuO depends on the existence and the concentration of Zn dopant in the electrodeposition solution. Duration of the deposition reaction calculates the growth rate for the conditions shown in Figure 5.8. Concentration of Zn dopant in the electrodeposition solution controls the growth rate of the CuO film. There are three growth rate regions in this range of concentration of Zn dopant. First, the growth rate is fast and does not change from 0 to 1 at% of the Zn dopant. In the second region from 2 to 4 at%, the growth rate

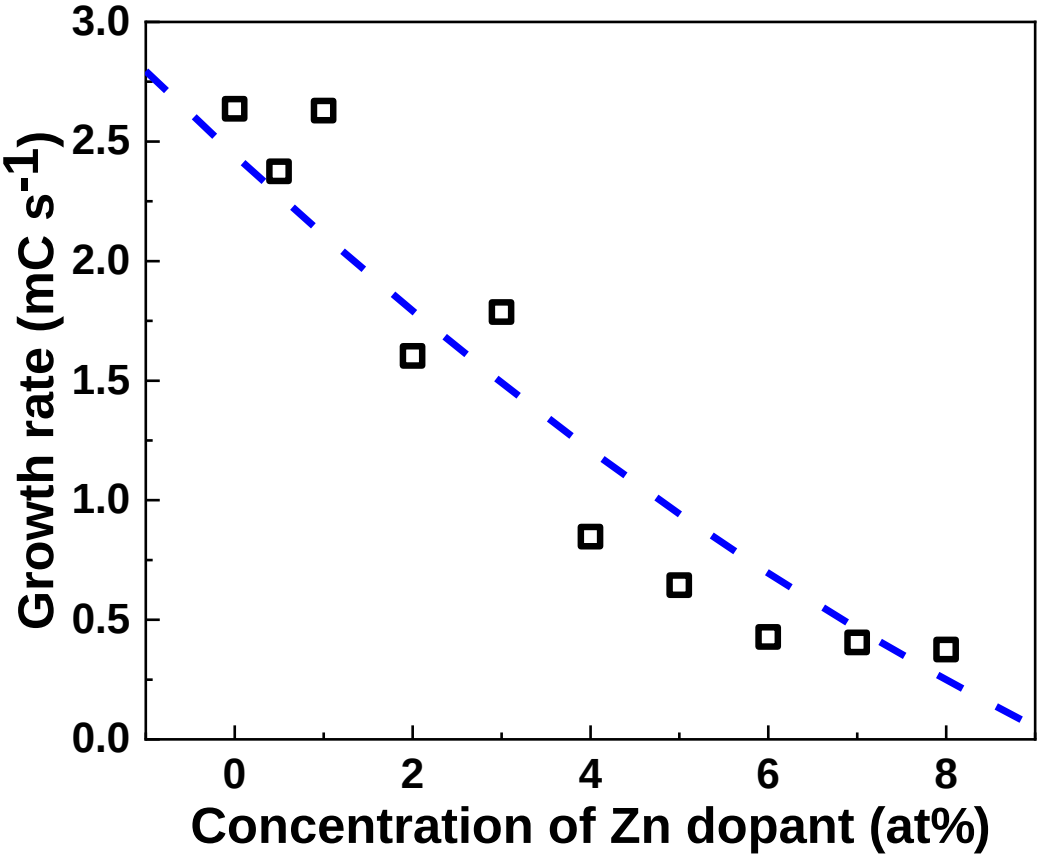

Figure 5.8 Growth rate depending on the concentration of Zn dopant in the electrodeposition solution.

decreases significantly. Finally, the growth rate does not change significantly above 5% of Zn dopant due to the excess materials that form the ZnO crystal. These results are dependent on the XRD results. Therefore, these results show that the growth rate of the crystal orientation of {200} and {002} is slower than {111} and $\{\bar{1}11\}$.

The photoactivity of the synthesized CuO and Zn:CuO as a function of the Zn dopant concentration is determined by obtaining the photocurrent density operating applied potential under illumination as shown in Figure 5.9. The measurement is carried out under artificial sunlight simulated AM 1.5 G illumination in the 0.1 M of Na_2SO_4 aqueous solution as an electrolyte. The improvement in photocurrent density is observed for Zn:CuO compared to the CuO film. Even very low amounts of Zn dopant (0.5 at%) enhances photocurrent density from -0.86 to -1.05 mA cm^{-2} at 0 V vs. RHE compared to CuO film. A large amount of Zn dopant shows a higher photocurrent density under illumination and shows no significant discrepancies among the Zn:CuO samples. The improvement of Zn:CuO using 0.5 at% is a result of the reduced average grain size of CuO rather than the changing crystallographic orientation. The Zn:CuO films above 0.5 at% have a stronger (200) and (002) crystallographic orientation with the dominant {111} and$\{\bar{1}11\}$ exposed facets which are non-polar. Even though the average grain sizes decrease with a higher amount of Zn dopant, the Zn:CuO (3, 5, 8 at%) shows similar photocurrent density due to the grain size remaining unchanged. This results in the shorter average minority carrier transport length from the smaller grain size to the photocathode/electrolyte interface. Therefore, the charge collection efficiency of Zn:CuO

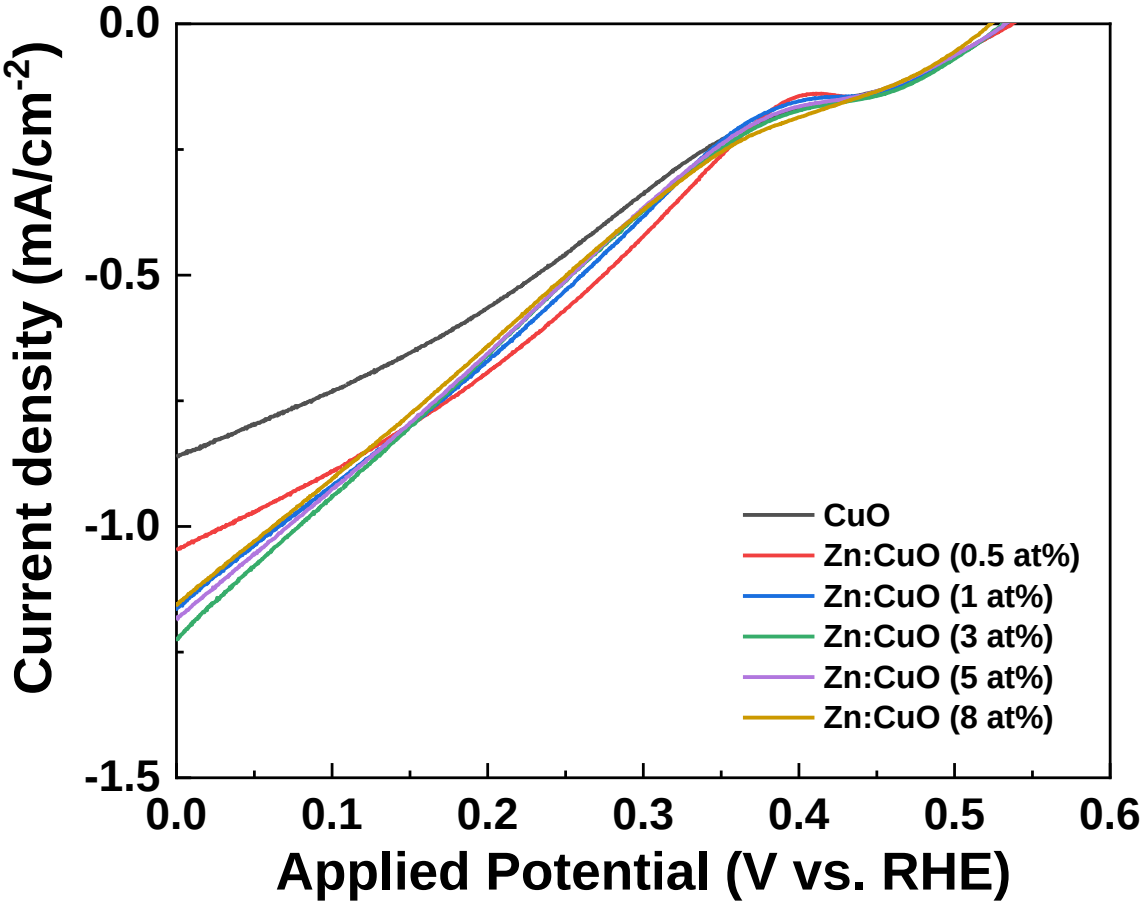

Figure 5.9 The photocurrent density versus the potential characteristics of CuO and Zn:CuO photocachode under simulated sunlight illumination.

is improved due to fast carrier transportation. By monitoring the degradation of the photocurrent density according to the PEC reaction time, the stability for PEC reaction is readily determined as shown in Figure 5.10. This PEC stability test measures the photocurrent density at 0 V vs. RHE applied potential in the 0.1 M Na_2SO_4 aqueous solution under chopped irradiation. The Zn:CuO using 5 at% of Zn dopant shows -1.7 mA cm^{-2} of initial photocurrent density which is one of the highest photocurrent densities compared to the relative systems shown in Table 5.1.[27, 36-40] The ratio of photocurrent density measured at initial to final of the reaction is calculated in order to compare the stability shown in Figure 5.11. The curves comparing photocurrent density versus time present a better stability of Zn:CuO operated in the PEC reaction compared to CuO. The stability of Zn:CuO operating as a photocathode in the PEC reaction can be maintained at more than 48% of its initial value after illumination for final. Its stability is higher than that of CuO which is maintained at 19%. Therefore, Zn dopant in the CuO crystal improves the stability of the PEC reaction under illumination. This is due to the {200} facets of CuO having a polar surface with higher surface energy that is favorable and CuO decomposition. Zn:CuO with non-polar {111} and {$\bar{1}$11} facets have a lower surface energy which is more stable under the photocathodic reaction. On the other hand, even though the stability of Zn:CuO synthesized at 8 at% of Zn dopant concentration is best among the samples, the photocurrent density for the entire region is lower than that of Zn:CuO at 5 at%. Therefore,

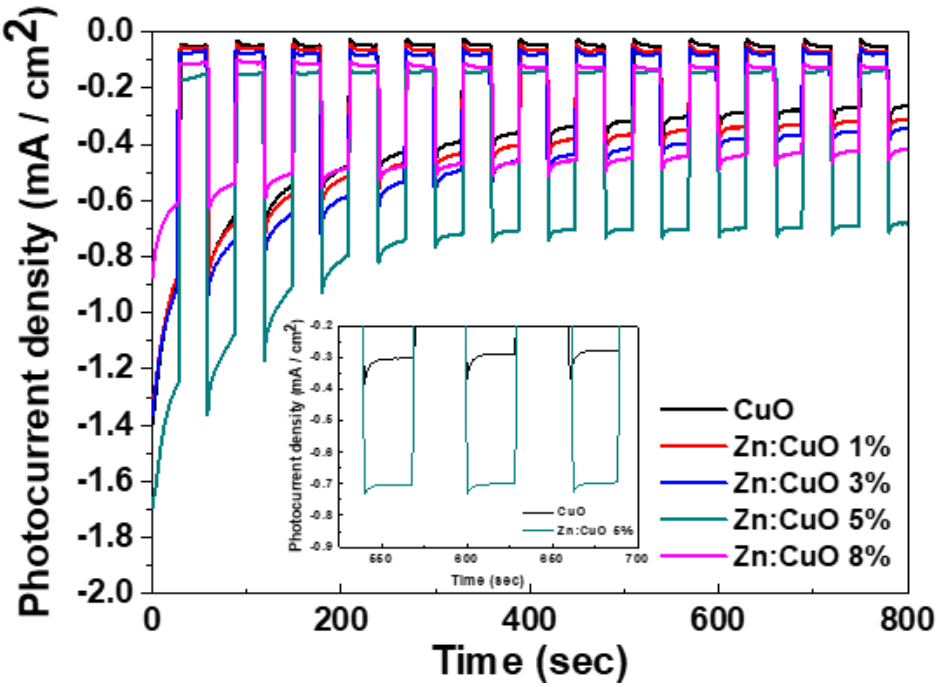

Figure 5.10 Stability tests of the synthesized CuO and Zn:CuO with 1, 3, 5, 8 at% Zn dopant. Ratio of photocurrent density at 800 sec to 1 sec (insert) and initial photocurrent density.

Table 5.1 Summary of the CuO-based photocathodes for PEC water splitting.

Material	Methods	J_{ph} @ 0 V_{RHE} (mA/cm_2)	Morphology	Electrolyte	Thickness	ref
CuO	Electrochemical deposition	-0.86	Film	0.1 M Na_2SO_4	1 μm	This work
Zn:CuO		-1.71	Film	0.1 M Na_2SO_4	1.7 μm	
CuO	Sputtering deposition	-0.92	Film	0.1 M Na_2SO_4	0.5 μm	37
Cu_2O/CuO/TiO_2	Electrochemical deposition	-0.84	Film	1 M Na_2SO_4	1.3 μm	36
Cu_2O/CuO	H_2-O_2 flame	-0.82	Film	0.5 M Na_2SO_4	3.5 μm	38
CuO nanowire	Thermal treatment	-1.18	Nanowire	0.5 M Na_2SO_4	5 – 20 μm	27
CuO	Sol-gel	-0.53	Film	0.1 M Na_2SO_4	0.6 μm	39
Ti:CuO	Sputtering deposition	-0.09 @ -0.2$V_{Ag/AgCl}$	Film	1 M Na_2SO_4	0.5 μm	40

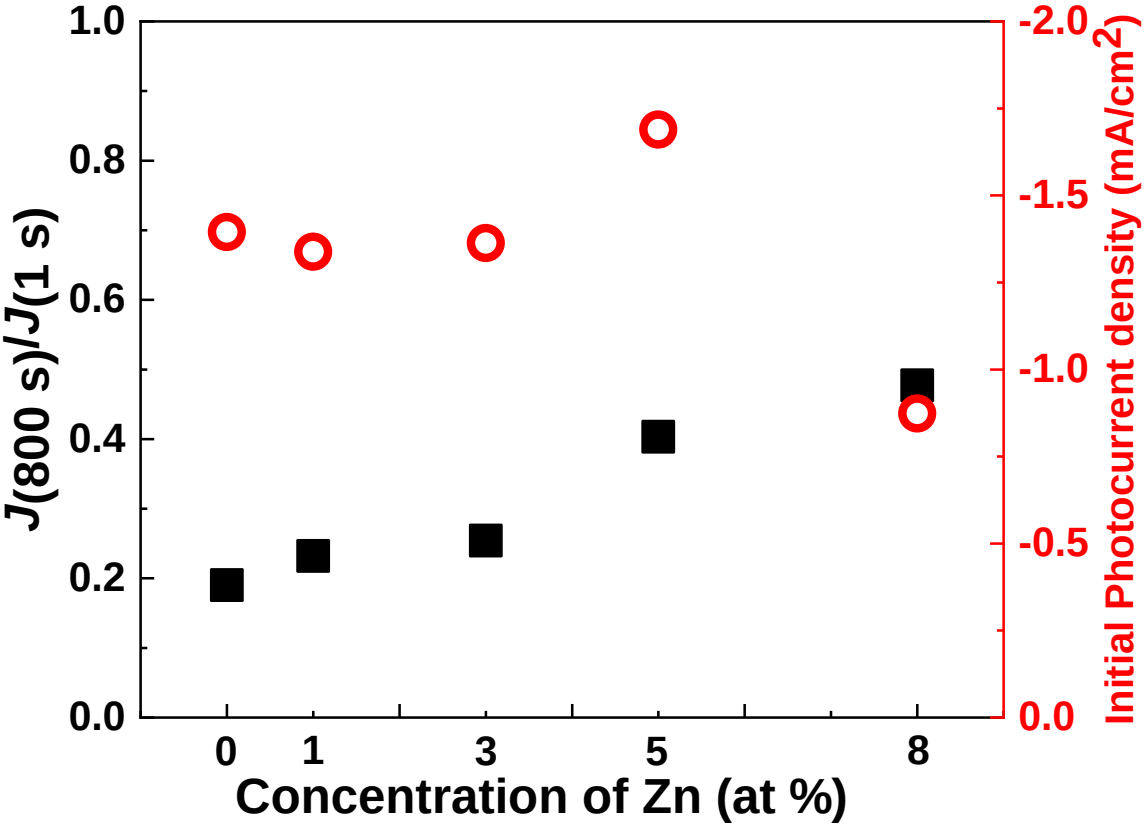

Figure 5.11 Ratio of photocurrent density at 800 sec to 1 sec (insert) and initial photocurrent density according to the concentration of Zn dopant.

Zn:CuO synthesized with the addition of 5 at% of Zn dopant demonstrates the best stability with the highest photocurrent density in this work. For the Zn:CuO at 8 at%, the heterojunction structure formed by ZnO nanoparticles on the CuO surface has an additional charge depletion region between n- and p- type semiconductors which hinders the excited electron transfer to the electrolyte. Therefore, CuO with a higher amount of ZnO nanoparticles synthesized above 5 at% concentration shows a lower photocurrent density. The inserted plot presents the photocathodic current for CuO and Zn:CuO under chopped irradiation. When the photocathode is illuminated by light, the photogenerated charge at the depletion region is separated and transported to the interface between the photoelectrode and electrolyte, and transferred to the electrolyte, sequentially. If there is a charge accumulation at the interface due to a slow kinetic reaction rate from the injection of electrons from the external circuit, it recombines with an accumulated number of holes at the interface between the photocathode and electrolyte.[27] The shape of the photocathodic spike is observed as soon as light illuminates the photocathode, and then the spike disappears after reaching equilibrium between the surface reaction and the charge recombination. It is well known that the phenomenon of a sharper photocathodic spike is ascribed to a larger amount of charge accumulation and slower reaction kinetics, while faster reaction kinetics and a lower amount of charge accumulation make the spike smoother. From our results, there is a significant difference in photocathodic spike shapes between CuO and Zn:CuO under illumination. The sharp cathodic transient spike is observed for CuO that presents the high charge accumulation at the interface between the photocathode and electrolyte. The Zn:CuO photocathode improves the transfer of the

photogenerated electrons to the electrolyte so it may participate in the reduction of H^+. This results in a decreased charge accumulation at the interface and the increases the spatial charge separation at interface between the photocathode and electrolyte. Therefore, we conclude that the cathodic transient spike for Zn:CuO almost vanishes at the interface by achieving a faster kinetic reaction rate due to the decreasing grain size and engineered surface facets.

The chemical state of surface elements of CuO and Zn:CuO could be evidenced by the X-ray photoelectron spectroscopy spectra as shown in Figure 5.12. The survey spectra of the pure CuO and Zn:CuO are dominated by the peaks of oxygen. The peaks related to the 1s orbital of the oxygen is located from the 528 to 534 eV range. The peak is well deconvoluted into four peaks. The peak due to Cu-O bonding for CuO crystal is centered at 529.82 eV. The samples with and without Zn dopant have the Cu-O peak in CuO crystal. Pure CuO has low intensity of the peak located at the 531 eV arising from the ionization of characteristics of oxygen species such as OH^-. On the other hand, Zn:CuO samples have higher intensity of the peak. It is evidence that the surface of Zn:CuO is covered by more hydroxyl group which can be surface active sites for hydrogen absorption and desorption reaction.[41] The absorbed hydroxyl group reacts proton to produce the hydrogen evolution reaction as shown in Figure 5. 13. Volmer-Tafel and Volmer-Heyrovsky reactions begin when the hydrogen connected to the surface react to the proton that produces hydrogen gas. Therefore, the higher coverage of hydroxyl group in Zn:CuO enhances the surface reaction by increasing amount of the reactive hydrogen atom. The electron generated by sunlight at the Zn:CuO reduces to hydrogen quickly faster than CuO which has less amount of

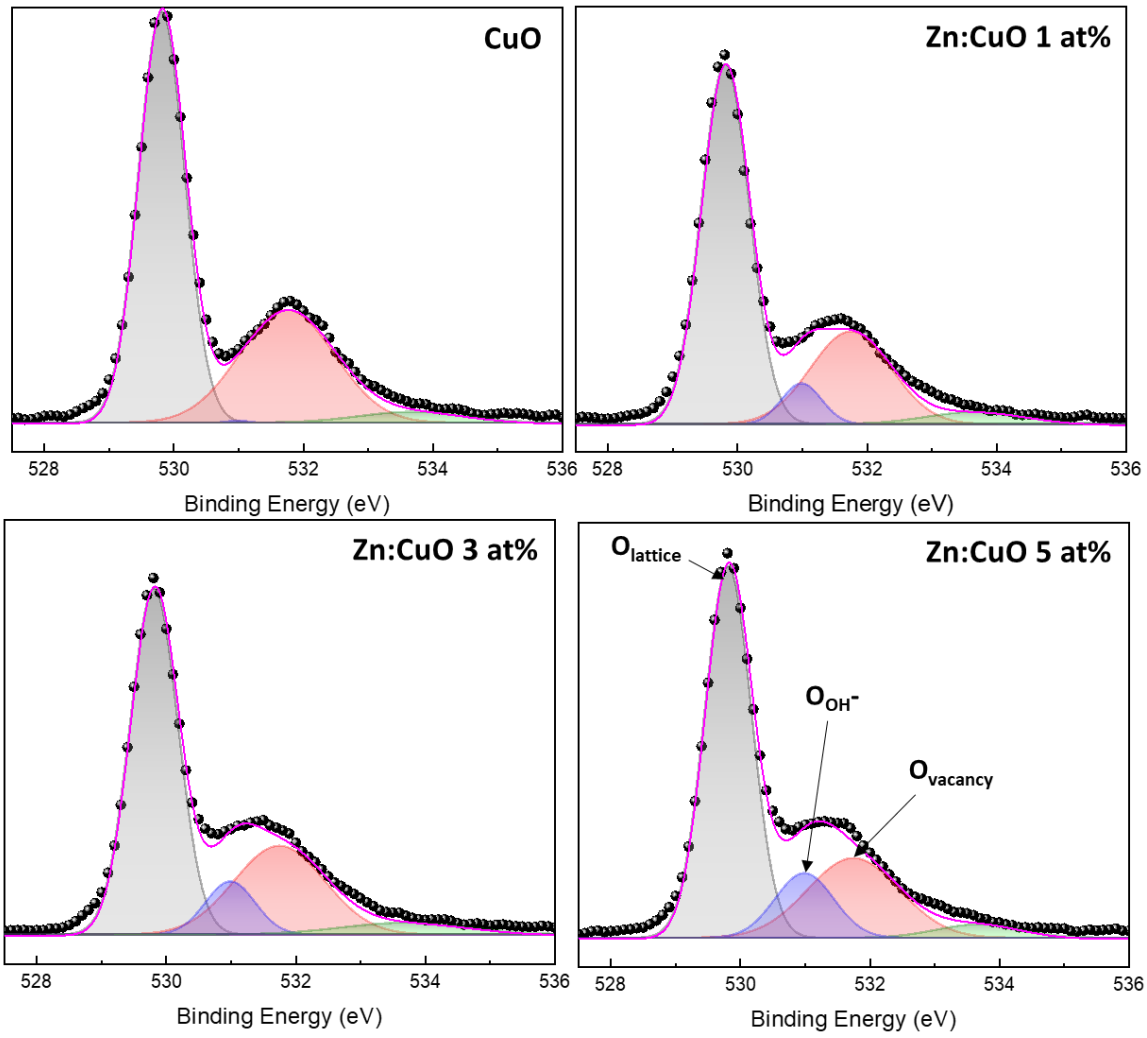

Figure 5.12 XPS spectra of oxygen 1s for CuO, and Zn:CuO (1, 3, and 5%). Oxygen from lattice ($O_{lattice}$), hydroxyl(O_{OH}-), and vacancy($O_{vacancy}$) are marked.

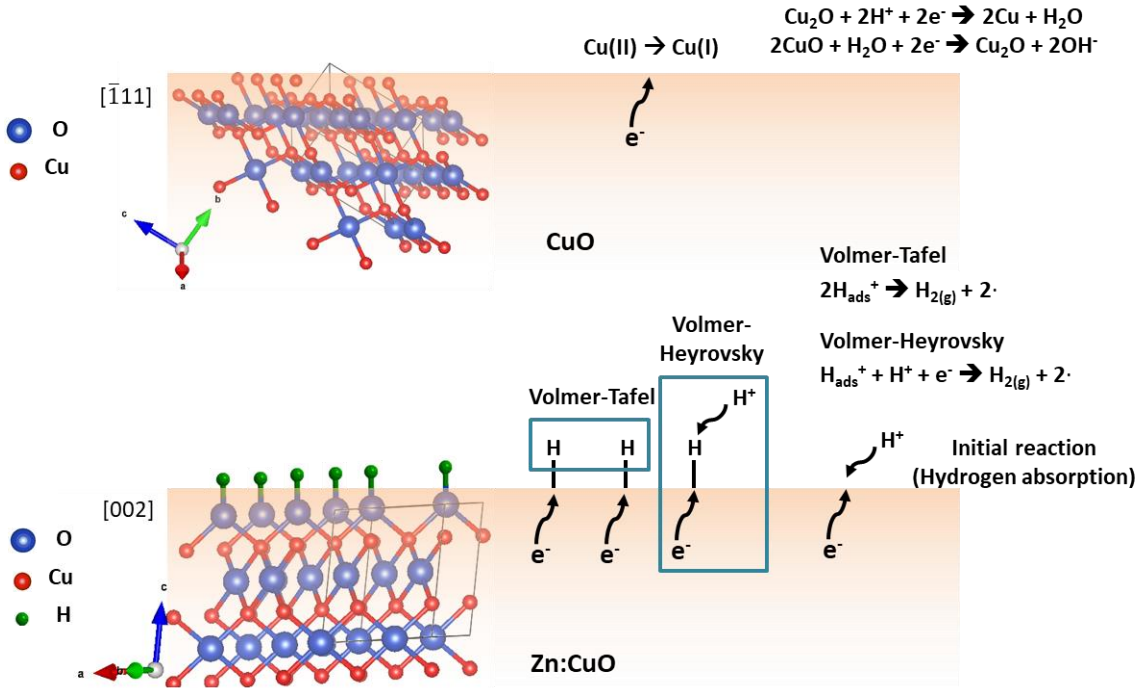

Figure 5.13 Schematic of hydrogen evolution reaction at the surface of CuO and Zn:CuO indicating hydroxyl group reacts proton when adding electron generated by sunlight.

hydroxyl group. Zn:CuO release charge accumulation due to the faster charge transfer to the hydroxyl group at the surface and larger surface area. The intensity of peaks at the 531.76 and 533.71 eV from the ionization of oxygen species which compensate deficiencies in the vicinity of CuO surface and weekly adsorbed species are similar to the samples regardless of Zn dopant.

5.4 Conclusion

In summary, Zn:CuO is successfully synthesized on FTO substrate as a photoelectrode via a facile electrodeposition process. The Zn dopant increases the amount of pores, decreases grain size, and engineers the crystallographic orientation of CuO with [002] and [200] that the surface of Zn:CuO has higher amount of hydrogen compared to CuO. Zn:CuO shows a higher photocurrent density of -1.7 mA cm^{-2} at 0 V vs. RHE and a better stability under AM 1.5 G illumination which is one of the highest photocurrent densities for CuO for PEC water splitting. The pores of [002] and [200] orientation have a shorter charge transport length and higher amount of absorbed hydrogen that prevents charge accumulation at the interface between Zn:CuO and electrolyte. Our simple method of doping elemental Zn in CuO crystals will pave the way to facilitate it as the primary photocathode in PEC devices.

Reference

[1] N. S. Lewis, *Am. Sci.*, **83**, 534-541 (1995).

[2] E. S. Andreiadis, M. Chavarot-Kerlidou, M. Fontecave. V. Artero, *Photochem. Photobiol.*, **87**, 946-964 (2011).

[3] S. Berardi, S. Drouet, L. Francàs, C. Gimbert-Suriñach, M. Guttentag, C. Richmond, T. Stoll, A. Llobet, *Chem. Soc. Rev.*, **43**, 7501-7519 (2014).

[4] A. Fujishima, K. Honda, *Nature*, **238**, 37-38 (1972).

[5] S. Y. Reece, J. A. Hamel, K. Sung, T. D. Jarvi, A. J. Esswein, J. J. H. Pijpers, D. G. Nocera, *Science*, **334**, 645-648 (2011).

[6] R. Chen, S. Pang, H. An, T. Dittrich, F. Fan, C. Li, *Nano Lett.*, **19**, 426-432 (2019).

[7] K. Sivula, F. L. Formal, M. Grätzel, *ChemSusChem*, **4**, 432-449 (2011).

[8] J. Miao, H. B. Yang, S. Y. Khoo, B. Liu, *Nanoscale*, **5**, 11118-11124 (2013).

[9] J. Chen, D. Yang, D. Song, J. Jiang, A. Ma, M. Z. Hu, C. Ni, *J. Power Sources*, **280**, 649-666 (2015).

[10] H. Bae, H. Rho, J.-W. Kim, Y.-T. Lee, S. H. Lee, K. Fuji, H.-J. Lee, J.-S. Ha, *Appl. Surf. Sci.*, **422**, 354-358 (2017).

[11] S. Ida, K. Yamada, T. Matsunaga, H. Hagiwara, Y. Matsumoto, T. Ishihara, *J. Am. Chem. Soc.*, **132**, 17343-17345 (2010).

[12] K. Tennakone, J. Bandara, *Sol. Energ. Mat. Sol. C.*, **60**, 361-365 (2000).

[13] K. Fujii, K. Ohkawa, *Jpn. J. Appl. Phys.*, **44**, L909-L911 (2005).

[14] T. Hisatomi, J. Kubota, K. Domen, *Chem. Soc. Rev.*, **43**, 7520-7535 (2014)

[15] H. Mettee, J. W. Otvos, M. Calvin, *Sol. Energ. Mater.*, **4**, 443-453 (1981)

[16] H. Bae, E. Kim, J.-B. Park, S.-J. Kang, K. Fujii, S. H. Lee, H.-J. Lee, J.-S. Ha, *J. Electrochem. Soc.*, **163**, H213-H217 (2016)

[17] X. Yang, A. Wolcott, G. Wang, A. Sobo, R. C. Fitzmorris, F. Qian, J. Z. Zhang, Y. Li, *Nano Lett.*, **9**, 2331-2336 (2009)

[18] T. W. Kim, K.-S. Choi, *Science*, **343**, 990-994 (2014)

[19] S. U. M. Khan, M. Al-Shahry, W. B. Ingler, *Science*, **297**, 2243-2245 (2002)

[20] Y.-S. Hu, A. Kleiman-Shwarsctein, A. J. Forman, D. Hazen, J.-N. Park, E. W. McFarland, *Chem. Mater.*, **20**, 3803-3805 (2008)

[21] A. Tacca, L. Meda, G. Marra, A. Savoini, S. Caramori, V. Cristino, C. A. Bignozzi, V. G. Pedro, P. P. Boix, S. Gimenez, J. Bisquert, *ChemPhysChem*, **13**, 3025-3034 (2012)

[22] M. D. Bhatt, J. S. Lee, *J. Mater. Chem. A*, **3**, 10632-10659 (2015)

[23] Z. Jin, Z. Hu, J. C. Yu, J. Wang, *J. Mater. Chem. A*, **4**, 13736-13741 (2016)

[24] A. Paracchino, V. Laporte, K. Sivula, M. Grätzel, E. Thimsen, *Nat. Matt.*, **10**, 456-461 (2011)

[25] R. N. Dominey, N. S. Lewis, J. A. Bruce, D. C. Bookbinder, M. S. Wrighton, *J. Am. Chem. Soc.*, **104**, 467-482 (1982)

[26] J. Gu, A. Wuttig, J. W. Krizan, Y. Hu, Z. M. Detweiler, R. J. Cava, A. B. Bocarsly, *J. Phys. Chem. C*, **117**, 12415-12422 (2013)

[27] J. Li, X. Jin, R. Li, Y. Zhao, X. Wang, X. Liu, H. Jiao, *Appl. Catal. B-Environ.*, **240**, 1-8 (2019)

[28] X. Guo, P. Diao, D. Xu, S. Huang, Y. Yang, T. Jin, Q. Wu, M. Xiang, M. Zhang, *Int. J. Hydrogen Energ.*, **39**, 7686-7696 (2014)

[29] W. Septina, R. R. Prabhakar, R. Wick, T. Moehl, S. D. Tilley, *Chem. Mater.*, **29**, 1735-1743 (2017)

[30] S. Masudy-Panah, R. S. Moakhar, C. S. Chua, A. Kushwaha, T. I. Wong, G. K. Dalapati, *RSC Adv.*, **6**, 29383-29390 (2016)

[31] A. Chen, G. Yang, H. Long, F. Li, Y. Li, P. Lu, *Thin Solid Films*, **517**, 4277-4280 (2009)

[32] A. Kushwaha, R. S. Moakhar, G. K. L. Goh, G. K. Dalapati, *J. Photoch. Photobio. A.*, **337**, 54-61 (2017)

[33] A. A. Dubale, A. G. Tamirat, H.-M. Chen, T. A. Berhe, C.-J. Pan, W.-N. Su, B.-J. Hwang, *J. Mater. Chem. A*, **4**, 2205-2216 (2106)

[34] S. Masudy-Panah, R. S. Moakhar, C. S. Chua, A. Kushwaha, G. K. Dalapati, *ACS Appl. Mater. Interfaces*, **9**, 27596-27606 (2017)

[35] Y. Yang, D. Xu, Q. Wu, P. Diao, *Sci. Rep.-UK*, **6**, 35158 (2016)

[36] A. Paracchino, J. C. Brauer, J.-E. Moser, E. Thimsen, M. Grätzel, *J. Phys. Chem. C*, **116**, 7341-7350 (2012)

[37] S. Masudy-Panah, R. S. Moakhar, C. S. Chua, H. R. Tan, T. I. Wong, D. Chi, G. K. Dalapati, *ACS Appl. Mater. Interfaces*, **8**, 1206-1213 (2016)

[38] J. Han, X. Zong, X. Zhou, C. Li, *RSC Adv.*, **5**, 10790-10794 (2015)

[39] Y.-F. Lim, C. S. Chua, C. J. J. Lee, D. Chi, *Phys. Chem. Chem. Phys.*, **16**, 25928-25934 (2014)

[40] H. Tang, M. A. Matin, H. Wang, S. Sudhakar, L. Chen, M. M. Al-Jassim, Y. Yan, *J. Electron. Mater.*, **41**, 3062-3067 (2012)

[41] J.-C. Dupin, D. Gonbeau, P. Vinatier, A. Levasseur, *Phys. Chem. Chem. Phys.*, **2**, 1319-1324 (2000)

Chapter 6

Conclusions and Future Work

CuO_x compounds such as CuO and Cu_2O as a protective layer and photocathodes are reported in this work. CuO shell on the ZnO nanorods surface is multifunction layer for protective charge recombination between photoelectrode and an organic dye in Chapter 2 and 3. We pave the way that CuO as a protective layer on the other metal-oxide surface. Also, CuO and Cu_2O film present their properties as a photocathode in photoelectrochemical water splitting. In Chapter 4, Cu_2O photocathode was successfully synthesized without Cu interlayer which is the recombination site of electron and hole. The Cu_2O photocathode shows increasing hydrogen evolution reaction without decreasing thickness of Cu interlayer. In Chapter 5, Zn dopant is used in the CuO crystal that is favorable plane to form hydroxyl group at the surface. This modified surface reduces the charge accumulation at the interface photoelectrode/electrolyte that improve the charge extraction. Development of these photocathodes with low charge recombination rate is important due to it is suffered from photocorrosion at the interface semiconductor/electrolyte.[1] In addition, the researches preventing surface states of photocathode which can act as the recombination sites will be necessary to improve an efficiency of hydrogen evolution and the stability during photoelectrochemical reaction.[2] However, these developments are not sufficient to commercially use photocathode consisting of CuO_x compounds in water splitting cells due to still low efficiency and poor stability, even though they have ability to utilize visible and infrared light. Therefore, it is

desirable to have higher charge extraction to electrolyte and reduce electron and hole recombination which deteriorates the stability. Additional layer for the protection such as ZnO, Ti_2O, RuO_x which are not blocking light and improving charge separation on the surface modified CuO_x compounds will be studied for further development.[3]

It is necessary to develop the photoanode along with the photocathode to fabricate water splitting cells without additional bias from the external source.[4] As I mentioned previous, the photocathode and photoanode absorb light in the range of different wavelength and produce electron and hole pair in the semiconductor material which participate the reduction and oxidation reaction, respectively. Therefore, including this research on the improvement in the efficiency and stability of photocathode, the invention of photoanode materials which can be used combined CuO photocathode accompany the fabrication of water splitting cell driven by only sunlight. The synthesis of n-type CuO semiconductor obtained from doping will be used to formation of homojunction.[5] It absorbs light and produce electron and hole pair that accepter react to water molecule. In addition, the other n-type semiconductors which have been developed will be used for this photoelectrochemical cells.

Due to limited instrumentation, the measurement of photocurrent density has been compared among the samples that it is widely used indirect technique. The amount of the generated hydrogen gas will be compared using gas chromatography.[6] For this research, the materials have not limited selection that do not need the substrate that transparent conductive film (fluorine doped tin oxide and indium tin oxide) deposited on the glass due

to electronic connection.[7] It has advantage for synthesis substrate free structure such as nanoparticles. This is because the measurement of amount gas shows hydrogen generation efficiency.

References

[1] M. E. Aguirre, R. Zhou, A. J. Eugene, M. I. Guzman, M. A. Grela, *Appl. Catal. B-Environ.*, **217**, 485-493 (2017).

[2] A. A. Ismail, D. W. Bahneman, *Sol. Energ. Mat. Sol. C.*, **128**, 85-101 (2014).

[3] T. Moehl, W. Cui, R. Wick-Joliat, S. D. Tilley, *Sustainable Energy Fuels*, **3**, 2067-2075 (2019).

[4] K. P. Sokol, W. E. Robinson, J. Warnan, N. Kornienko, M. M. Nowaczyk, A. Ruff, J. Z. Zhang, E. Reisner, *Nat. Energ*., **3**, 944-951 (2018)

[5] W. Chen, D. Qi, X. Gao, A. T. S. Wee, *Prog. Surf. Sci.*, **84**, 279-321 (2009)

[6] J. Lee, J. Yun, S.-R. Kwon, W. J. Chang, K. T. Nam, T. D. Chung, *Sci. Rep.*, **7**, 12281 (2017)

[7] M. I. Abdullah, A. Hameed, N. Zhang, M. Ma, *Adv. Mater. Interfaces*, **6**, 1900586 (2019)